UiO : Department of Physics
University of Oslo

Spectral Analysis of the Electron Density Fluctuations Measured by the ICI-2 Sounding Rocket

Master's Thesis

Andres Spicher

Mai 2013

Abstract

The Investigation of Cusp Irregularities (ICI) series of sounding rockets are aimed to study plasma instabilities and turbulence associated with cusp flow channels and F-region electron density patches. The ICI-2 sounding rocket was launched into the cusp ionosphere in December 2008 from Ny-Ålesund, Svalbard, and intersected several poleward moving auroral forms. The unprecedented high sampling rate of 5.7 kHz of absolute electron density made by the multi-needle Langmuir probes (m-NLP) allowed measurements of plasma irregularity structures down to meter scales. The rocket intersected instability regions in relation to both particle precipitation and density enhancements. In this thesis the spectral characteristics of electron density fluctuations associated with the encountered plasma structures are analyzed. We present the power laws of the irregularity spectra observed in different plasma regimes during the flight. The power spectra of the strong density fluctuations exhibit a characteristic dual-slope power law behavior with a spectral knee at frequencies in the range $f_{sb} \in [20, 55]$ Hz, corresponding to wavelengths $\lambda_{sb} \in [25, 60]$ m. The spectral indices are $p_1 = -1.8$ below approximately 30 Hz and $p_2 = -4$ at frequencies above 40 Hz. In the literature, very little evidence of this two-component spectrum exists for the high latitude F-region. Our results are discussed in the context of ionospheric turbulence and compared with the previous studies of high latitude and equatorial regions. The results strongly suggest the gradient-drift instability as being the dominant mechanism for the generation of the observed irregularities.

Acknowledgment

I would like to thank my two supervisors, Jøran I. Moen and Wojciech J. Miloch for their valuable help and their support throughout this thesis. I am thankful to Jøran I. Moen for the trust he put in me by giving me an exciting and challenging thesis topic that is a part of an actual research project of greater scale, i.e. the STAR project.

A special thanks goes to Wojciech J. Miloch, who devoted his precious time and energy to help me going forward with my work, even whilst abroad. He also read through my thesis and gave me very constructive feedbacks.

Thanks to Tore André Bekkeng and Espen Trondsen for their help concerning the different rocket instruments, Hans Pécseli for the numerous discussions about plasma instabilities and Bjørn Lybekk for all the technical assistance.

I would also like to thank Lasse Clausen for providing me with the electric field data and the SuperDARN figures, as well a Yoshifumi Saito for the particle precipitation data.

In addition, I am grateful to Ragnhild Bøhler, Max Grönke and Antonio Delfino for also reading through this thesis and giving me feedbacks.

Moreover, thanks to my family for supporting me and helping me financially to pursue my studies in Norway. Thanks also to my friends and colleagues for making my stay in Norway particularly pleasant.

Andres Spicher
Oslo, Mai 2013

Contents

List of used symbols

Symbol	Name
$\mathbf{r}$	Vector position
$\mathbf{u}$	Velocity in the Eulerian description.
ω	Vorticity vector
F_s	Sampling rate
L	Characteristic length scale and gradient length scale
l_0	Characteristic length of large-scale structures
η	Characteristic length of small-scale structures
u_l	Characteristic speed of large-scale structures
u_η	Characteristic speed of small-scale structures
μ	Total viscosity coefficient
ν	Kinematic viscosity coefficient
ϵ	Mean energy dissipation per unit mass
Π	Flux of energy down the cascade
ρ	Mass density
ρ_k	Mass density of species k
ρ_c	Charge density
M_k	Mass of species k
p	Pressure
Re	Reynold's number
S_p	Structure function
q	Electric charge
r_{Lk}	Gyroradius of species k
Ω_{ck}	Gyrofrequency of species k
λ_D	Debye length
λ_{Def}	Effective Debye length
n_k	Density number of species k
ν_{kl}	Collision frequency between species k and l
$\mathbf{B}$	Magnetic field
$\mathbf{E}$	Electric field
$\mathbf{J}$	Current
T_k	Temperature of species k
τ	Time lag
κ_k	Ratio of gyrofrequency to collision frequency of species k
μ_k	Mobility of species k
H_k	Scale height of species k
D_k	Diffusion coefficient of species k
ϵ_0	Permittivity of free space
μ_0	Permeability of free space
σ	Conductivity
t_{of}	Time of flight
h	Altitude
λ_b	Wavelength at which the power spectrum steepens

Symbol	Name
k_b	Wavenumber at which the power spectrum steepens
f_s	Sampling frequency
f_{sb}	Sampling frequency at which the power spectrum steepens
k_B	Boltzmann constant
Γ	Continuous power spectrum
S_{xx}	Sample spectrum for a discrete series
c_{xx}	Discrete autocovariance
C	Reduced spectrum
γ_{XX}	Autocovariance function
x_t	Discrete time series
v_0	Magnitude of the velocity with respect to the neutrals; also called *slip* velocity
γ_{GDI}	Growth rate for the gradient-drift instability
γ_{KH}	Growth rate for the Kelvin-Helmoltz instability
$W_n(s)$	Wavelet coefficient for translation n and scale s
$\mathbf{u}_D$	$\mathbf{E} \times \mathbf{B}$-drift velocity
$\mathbf{F}$	External force
R_E	Earth radius
$\underline{\sigma}$	Conductivity tensor
σ_P	Pedersen conductivity
σ_H	Hall conductivity
σ_0	Conductivity parallel to $\mathbf{B}$
Σ_p	Height-integrated Pedersen conductivity
Σ_H	Height-integrated Hall conductivity
N_e	Electron density
$D_\perp$	Diffusion coefficient perpendicular to $\mathbf{B}$
$D_{k\perp}$	Diffusion coefficient perpendicular to $\mathbf{B}$ for species k
$D_\parallel$	Diffusion coefficient parallel to $\mathbf{B}$
Λ	Plasma parameter
$\hat{\mathbf{B}}$	Unit vector in the direction of $\mathbf{B}$
$\hat{\mathbf{g}}$	Unit vector in the direction of $\mathbf{g}$
β	β-parameter used to classify plasmas
V_f	Floating potential

- ICI-2 Investigation of Cusp Irregularities-2
- m-NLP Multi-Needle Langmuir Probe
- NSE Navier-Stokes Equations
- IMF Interplanetary Magnetic Field
- MHD Magneto-Hydrodynamics
- AU Astronomical Unit
- CMEs Coronal Mass Ejections
- CIRs Co-rotational Interaction Regions
- UV Ultraviolet
- EUV Extreme Ultraviolet
- DST Discrete Fourier Transform
- FFT Fast Fourier Transform
- pdf Probability Density Function
- rv Random Variable
- acvf Autocovariance Function
- PSD Power Spectral Density
- MSP The Meridian Scanning Photometer
- EISCAT European Incoherent Scatter
- ASI All-Sky Imager
- RT Rayleigh-Taylor Instability
- GDI Gradient-Drift Instability
- CC Current-Convective Instability
- KH Kelvin-Helmoltz Instability
- DW Drift-Wave Instability
- IC Ion-Cyclotron Instability
- CGM Corrected Geomagnetic Coordinates
- UT Universal Time
- MLT Magnetic Local Time
- MLAT Magnetic Latitude
- COI Cone Of Influence
- LEP Low Energetic Particle
- IGRF International Geomagnetic Reference Field
- IRI International Reference Ionosphere
- NED Earth-fixed coordinate system North-East-Down
- LLBL Low Latitude Boundary Layer
- FAC Field Aligned Current
- EBI Equatorward Boundary Intensifications
- PMAFs Poleward Moving Auroral Forms
- BPS Boundary Plasma Sheet
- CPS Central Plasma Sheet
- HF High Frequency
- UHF Ultra High Frequency
- VHF Very High Frequency
- TOI Tongue Of Ionization
- GPS Global Positioning System

1 Introduction

It is a well established fact that electron density irregularities are common phenomena in the F-region high latitude ionosphere (e.g Dyson et al., 1974; Kelley et al., 1980; Tsunoda, 1988; Basu et al., 1988). These irregularities have spatial scales ranging from tens of kilometers to a few meters (e.g. Phelps and Sagalyn, 1976; Basu et al., 1990; Carlson, 2012; Moen et al., 2012) and may cause negative effects on communication and navigation systems (e.g. Moen et al., 2013). Indeed, they may distort radio signals as the radio waves propagate through the highly fluctuating plasma and cause backscatter at longer wavelengths, for example at HF frequencies (e.g. Moen et al., 2000). High latitude ionospheric irregularities are thus of particular interest for mitigation/circumvention of consequences to satellite communication, Global Positioning System (GPS) navigation and HF communications.

When the interplanetary magnetic field (IMF) directed southward, the generalized view is that the irregularities located on the dayside are closely related to the density gradients associated with electron density enhancements and/or polar cap patches (e.g. Moen et al., 2013). Polar cap patches are defined as hundreds of kilometers scale islands with F-region plasma density 2 to 10 times larger than the background density present in the polar cap (e.g. Crowley, 1996; Carlson, 2012). Low density patches can be produced by auroral precipitation while high density patches have solar EUV origins (Carlson, 2012). After creation at sub-auroral latitudes, these enhanced density structures convect poleward into the polar cap and into the nightside, following the convection pattern. Polar cap patches are highly structured regions and irregularities have been observed to populate them entirely (Kivanc and Heelis, 1997). However, the strongest irregularities are often located on the trailing edges of the plasma patches or strong density enhancements (Weber et al., 1984).

A long list of mechanisms have been proposed to be responsible for these irregularities (e.g. Kintner and Seyler, 1985; Tsunoda, 1988). Nowadays, two macroinstabilities are believed to be the dominant mechanisms for the production of irregularities in the high-latitude F-region (Carlson et al., 2007); the Gradient-Drift instability (GDI) and the Kelvin-Helmoltz (KH) instability. The GDI occurs when a gradient is present in the plasma and is due to the different drifts of the ions and the electrons perpendicular to the gradient (Ossakow and Chaturvedi, 1979; Keskinen and Ossakow, 1983). The GDI has a preferred direction, meaning that it is unstable if the $\mathbf{E} \times \mathbf{B}$ polarization drift produced by the charge separation is parallel to the preexisting density gradient (e.g. Tsunoda, 1988). This instability is believed to be a dominant mechanism in the polar caps (e.g. Ossakow and Chaturvedi, 1979; Keskinen and Ossakow, 1983; Tsunoda, 1988; Cerisier et al., 1985; Carlson et al., 2007; Oksavik et al., 2012). The KH plasma instability is accredited to strong velocity shear flows occurring in the direction perpendicular to the magnetic field (e.g. Keskinen et al., 1988; Treumann and Baumjohann, 1997). Carlson et al. (2006, 2007, 2008) argued that velocity shears were inherent polar cap patch formation, implying that the KH instability was likely to be the first mechanism to structure patches. The GDI would then operate as a secondary process breaking down the structures into smaller-scales (Carlson, 2012). However, work still remains to be done on the quantification and the characterization of F-region irregularities.

Research about small-scale irregularities in the high-latitude F-region has not progressed as fast as in the equatorial regions (Kelley, 2009). A probable reason is the geometrical impossibility for high-latitude ground based radar to obtain an appropriate backscatter angle at F-region using VHF and UHF systems (Kelley, 2009). F-region ground-based radar are possible at HF frequencies but their resolution is usually too poor to investigate in depth the electron density fluctuations at decameter scales. Therefore, Moen et al. (2002) pointed out an ultimate need for high-resolution in-situ measurements in order to be able to characterize irregularities at small-scales and assess the role of different instability mechanisms. Hence, a series of sounding rockets has been constructed by the University of Oslo and launched in the dayside polar caps at F-region altitudes.

In this study, the high-resolution electron density data obtained from the measurements made by the Investigation of Cusp Irregularities 2 (ICI-2) sounding rocket is analyzed. The ICI-2 sounding rocket was launched from Ny-Ålesund, Svalbard, Norway (78.9° N, 11.9° E geographic coordinates) at 1035 Universal Time (UT) on the 5th of December 2008 and had for main objective to perform in-situ observations of HF radar echoing targets and to quantify the gradient drift instability mechanism. Power spectral analysis is performed on the electron density fluctuation data at various segments of cusp/polar cap activities associated with different plasma structures such as particle precipitations or density gradients. Previous satellites and rocket experiments showed that the density fluctuations in the high-latitude ionosphere exhibited power law spectra (e.g. Dyson et al., 1974; Phelps and Sagalyn, 1976; Basu et al., 1988, 1990; Mounir et al., 1991). Thus, the main objective here is to determine whether different power-laws can be associated with different plasma structures and further, to determine whether different candidate instability mechanisms imprint different power spectral features.

The following thesis is divided into three parts. The first part consists of a theoretical background. It describes the basics of plasma physics and gives a general overview of the Near-Earth plasma environment. The coupling between the Earth and the Interplanetary space, as well as the resulting plasma structures are also presented here. Then, the basics of fluid turbulence theory are derived as an intuitive approach, in order to introduce plasma turbulences and irregularities.

The second part is focused on the description of the experiment. Different instruments used in this study are presented. Emphasis is put on the ICI-2 rocket and on the Langmuir probes as these were the principal devices used. In addition, the methods to analyze the data are presented, namely the windowed fast Fourier transforms and the Morlet wavelet transforms. This part ends with the description of some assumptions and considerations regarding the study of plasma structures using spacecrafts.

The third part of this thesis concerns the measurements and the discussion of the results. First, the plasma-flow conditions of the rocket flight are given. Then, the electron density structures measured by the rocket are described and the analyzed data are presented. The results are compared with previous experimental studies in order to put them into a wider context. They are finally discussed with respect to several instability mechanisms. The thesis ends with a list of ideas for future work or experiments that could be done in order to obtain a better knowledge about small-scales irregularities in the high-latitude ionosphere.

2 Theoretical Background

In this chapter, a general background in space physics is given. It starts with a description of the basics of plasma physics and presents a general picture of the near-Earth environment, with emphasis on the high-latitude ionosphere. Then, the basics of fluid turbulence theory are derived as an intuitive approach, in order to introduce plasma turbulences and different irregularity mechanisms that might occur in the ionosphere.

2.1 Plasma physics

On Earth we are principally confronted to matter as being solid, liquid or gas. However in the universe (above the lower layers of the Earth's atmosphere), most of the matter is in a state called plasma (Baumjohann and Treumann, 1996). Hence, notions of plasma physics are necessary when one desires to study structures in the ionosphere (as it is the case here). Hence, in this section, some of the fundamental plasma characteristics are briefly presented as well as the basic dynamics of charged particles in electric and magnetic fields. In addition, the equations governing the one- and two- fluid models are presented.

2.1.1 Definition of plasma

A plasma is essentially a gas composed of charged particles, electrons and ions, rather than neutral molecules or atoms. Plasmas are electrically neutral overall, but due to the existence of charged particles, they can support electric and magnetic fields. They generally satisfy two conditions (Cairns, 1985):

- Quasi-neutrality: the sum of the charges of all particles is equal to zero in a macroscopic volume.
- Collective behaviors: the collective effects of the particles are more important than the ones due to Coulombian forces between the charges.

Hence, plasma cannot simply be treated as an ordinary gas which is electrically conducting.

There are mainly three levels of description of plasma giving raise to different sets of equations. The first one is a kinetic description, based on the trajectories of individual particles. The second one is a fluid description, where the plasma is considered as a charged gas/fluid governed by fluid equations. When the plasma is assimilated to a single fluid, this model is referred as magneto-hydrodynamics (MHD). In the third description, the fluid equations are also used but the plasma is divided into a mixture of two gases, an electron and an ion gas. This model is referred as the two-fluid approximation or multi-component plasma (Pécseli, 2012). Depending on the length and time scales over which the system considered changes, one or the other description is better suited. Fluid equations are usually used for describing large scales plasmas while kinetic equations are better adapted to characterize high frequency motions.

The Debye length

An important parameter in plasma physics is called the *Debye length*, λ_D. It characterizes a shielding distance of any electric charge by the plasma. For example, if a positive charge is placed in a plasma, the electrons are attracted towards it and the ions repelled, creating a screen of negative charge around it. Consequently, the potential falls off with radial distance and, at few Debye lengths, the electric potential due to that charge is zero (and the plasma is quasi-neutral). The Debye length is defined by

$$\lambda_D \equiv \sqrt{\frac{\epsilon_0 k_B T}{nq^2}} \tag{2.1}$$

where n is the number density, q the charge, ϵ_0 the permittivity of free space and k_B the Boltzmann constant. When the plasma is considered as a mixture of both mobile electrons and mobile ions with an isothermal Boltzmann distribution, one can obtain the effective Debye length λ_{Def} (Pécseli, 2012)

$$\frac{1}{\lambda_{Def}^2} = \frac{1}{\lambda_{Di}^2} + \frac{1}{\lambda_{De}^2}. \tag{2.2}$$

Any charged particle in a plasma attracts a screening charge towards it, having for consequence that the effective range of inter-particle force is of the order of the Debye length. This is important when a device is put into a plasma to make measurements such as it was done with the probes on the ICI-rockets. A negatively biased electrode attract a surplus of positive charges around it, while a positively biased electrode acquires an electron shielding cloud surrounding it. The size and the shape of the probes must thus be adapted to the plasma investigated.

The plasma parameter

From the Debye length and the plasma density, one can obtain a number called the *Plasma parameter* Λ, giving the number of particle in a sphere of radius λ_D (apart from a constant $4\pi/3$). The plasma parameter is defined as (Cairns, 1985)

$$\Lambda \equiv n\lambda_D^3. \tag{2.3}$$

Since the shielding described in section 2.1.1 is the result of the collective behaviors inside a Debye sphere, the number of particles inside the sphere must be high ($\Lambda \gg 1$). Note that Λ decreases for plasmas with increasing density and constant temperatures. The plasmas satisfying $\Lambda \gg 1$ are thus *hot* and *dilute* (Pécseli, 2012).

The plasma frequency

A plasma is also characterized by the oscillation of its particles. The frequency of these oscillations is called the *plasma frequency* and is given by

$$\Omega_{pk} = \sqrt{\frac{q_k^2 n_k}{\epsilon_0 M_k}}, \tag{2.4}$$

where the subscript k refers to each species, i.e. $k = i$ for ions and $k = e$ for electrons. These subscripts will be used throughout the entire thesis.

The β parameter

It can be shown that a plasma is a *diamagnetic*, having the property that high plasma pressure reduces magnetic pressure (Pécseli, 2012). The relative importance between the thermal and the magnetic pressure is defined as

$$\beta \equiv \frac{p_{thermal}}{p_{magnetic}} = \frac{n\kappa T}{B^2/2\mu_0} \tag{2.5}$$

where the ideal gas law was used in the last equality. The β parameter is important for classifying plasmas. Typical values in the solar wind are $\beta \in [0.5, 1]$ (Pécseli, 2012).

2.1.2 Single particle motion

Per definition, a plasma is composed of charged particles. The motion of charged particles in presence of a magnetic ($\mathbf{B}$) or electric ($\mathbf{E}$) field is dictated by the Lorentz force $\mathbf{F}_L = q\mathbf{E} + q\mathbf{u} \times \mathbf{B}$. The trajectories for stationary and homogeneous $\mathbf{B}$ and $\mathbf{E}$ are presented here in order to introduce the simplest features of particle motions and drifts engendered by electric or magnetic fields. A more complete description of possible trajectories, also when the fields are inhomogeneous, is given in Pécseli (2012) for example.

The starting point is Newton's second law

$$m\frac{\mathrm{d}}{\mathrm{dt}}\mathbf{u} = q\mathbf{E} + q\mathbf{u} \times \mathbf{B}, \tag{2.6}$$

where $\mathbf{u}$ is the velocity of a particle with mass M. Two cases are considered, one for $\mathbf{E} \parallel \mathbf{B}$ and the other for $\mathbf{E} \perp \mathbf{B}$.

- $\mathbf{E} \parallel \mathbf{B}$: When the electric and magnetic fields are parallel, i.e. $\mathbf{E} \parallel \mathbf{B}$, the motion along $\mathbf{B}$ is a steady acceleration

  $$u_\parallel = \frac{q}{M}E_\parallel + u_{0\parallel}. \tag{2.7}$$

  In the direction perpendicular to $\mathbf{B}$, electrons and ions will gyrate in a circular orbit with a frequency Ω_{ck}, the *gyrofrequency*, and with a radius r_{Lk}, the *Larmor radius*. These two quantities are given by

  $$\Omega_{ck} = \frac{qB}{Mk} \quad \text{and} \quad r_{Lk} = \frac{u_\perp}{|\Omega_{ck}|}. \tag{2.8}$$

  Since the direction of rotation is dictated by the charge ions and electrons gyrate in opposite directions around the magnetic field.

- $\mathbf{E} \perp \mathbf{B}$: When $\mathbf{E} \perp \mathbf{B}$, it can be shown that the average location of a particle over a gyro-period, referred as the *guiding center*, is drifting with velocity

  $$\mathbf{u}_D = \frac{\mathbf{E} \times \mathbf{B}}{B^2}. \tag{2.9}$$

The trajectory is a combined rotation and drift perpendicular to both the magnetic and the electric field. An illustration of this motion for both ions and electrons is shown in Figure 2.1. Mathematically, it is referred as a cycloid. This motion occurs often in the ionosphere and has been termed the $\mathbf{E} \times \mathbf{B}$-drift. Since the particles are moving in the same direction, no charge separation is occurring, and thus no current created. Note that the electric field $\mathbf{E}$ could be replaced in Eq. (2.6) by a force such as gravity and a drift would also occur.

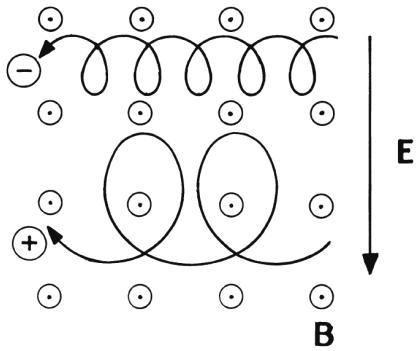

Figure 2.1: Schematic illustration of the $\mathbf{E} \times \mathbf{B}$-drift for ions and electrons. Courtesy of Pécseli (2012).

2.1.3 The fluid description

When focus is not put on the motion of individual particles, a plasma can be described as an electrically conducting fluid able to interact with magnetic and electric fields. This description requires a set of equations regrouping both fluid and electrodynamics terms. The most important features of neutral fluid theory, as well as the main equations of electrodynamics are presented below. These equations will then be used to construct the MHD and the two-fluid models, which are, for example, used to described solar wind plasmas and ionospheric plasmas, respectively.

Fluid treatment is based on the continuum model in which the fluid is assimilated to a continuous mass (a lump of fluid) rather than to discrete particles. Two different descriptions can be used: the Lagrangian and the Eulerian. The Lagrangian type links each fluid particle to a material point, which is followed in time, while the Eulerian method describes flow quantities by a function of position in space $\mathbf{x}$ and time t, using vector field of velocities $\mathbf{u}(\mathbf{x}, t)$. In this thesis, the Eulerian description will be used. The acceleration, given by *the rate of change of a quantity associated with a fluid element* contains an additional term compared to the usual partial derivative $\partial(\cdot)/\partial t$. The convective derivative $D(\cdot)/Dt$ of a fluid with velocity $\mathbf{u}$ is defined as (Davidson, 2006)

$$\frac{D(\cdot)}{Dt} \equiv \frac{\partial(\cdot)}{\partial t} + (\mathbf{u} \cdot \nabla)(\cdot). \tag{2.10}$$

The Navier-Stokes equations

The starting point to derive the equations of motion of a fluid, called the Navier-Stokes equations (NSE), is Newton's second law. For an incompressible fluid whose mass-conservation law is

$\nabla \cdot \mathbf{u} = 0$, with a viscosity coefficient uniform over the fluid, the NSE are given by (see Batchelor (2000) for a complete derivation)

$$\rho \frac{D\mathbf{u}}{Dt} = \rho \left\{ \frac{\partial \mathbf{u}}{\partial t} + (\mathbf{u} \cdot \nabla)\mathbf{u} \right\} = \rho \mathbf{F} - \nabla p + \mu \nabla^2 \mathbf{u}, \tag{2.11}$$

where ρ is the fluid density, p the pressure, $\mathbf{F}$ an external force and μ the total viscosity coefficient.

The NSE contain a non-linear term in $\mathbf{u}$ that can lead to very complex solutions. The impossibility of solving them completely is known as the *closure or smoothness problem* and researchers are still trying to find a unified solution (Sonar, 2011). However with some assumptions about the flow, there exists cases where the NSE can be analytically solved and the results are in good agreements with experimental studies. In addition, the NSE are widely used as basis for numerical simulations of fluids.

Mass conservation

The mass conservation equation states that the flux of material entering or exiting a volume V through its surface Σ must be equal to the rate of mass variations inside the volume. Mathematically, it is relating the mass density ρ and the velocity $\mathbf{u}$ by

$$\iiint_V \frac{\partial \rho}{\partial t} \mathrm{d}V = - \iint_\Sigma \rho \mathbf{u} \cdot \mathrm{d}\mathbf{A}. \tag{2.12}$$

From this equation, it is possible to obtain the *continuity equation* for neutral fluid

$$\frac{\partial \rho}{\partial t} = -\nabla \cdot (\rho \mathbf{u}). \tag{2.13}$$

Equation of state

In addition to the equations of motion and of mass conservation, an equation of state has to be considered in order to be able to solve the full set of fluid equations. Several expressions can be accounted as an equation of state depending on the system considered (Kelley, 2009). For example, it could be the incompressibility condition, i.e. $\nabla \cdot \mathbf{u} = 0$. When the plasma is assimilated to an ideal gas, the equation of state is given by

$$p = n k_B T. \tag{2.14}$$

Electrodynamics equations

Remembering that a plasma is composed of charged particles, the forces from magnetic and electric fields have to be introduced. Hence, in addition to the basic fluid equations, one needs to consider Ohm's Law and Maxwell's equations (e.g. Proelss, 2004; Pécseli, 2012):

$$\mathrm{J} = \sigma\left(\mathbf{E} + \mathbf{u} \times \mathbf{B}\right) \quad \text{Ohm's law,} \tag{2.15}$$

$$\nabla \cdot \mathbf{E} = \frac{\rho_c}{\epsilon_0} \quad \text{Gauss' law for electricity,} \tag{2.16}$$

$$\nabla \times \mathbf{E} = -\frac{\partial \mathbf{B}}{\partial t} \quad \text{Faraday's law,} \tag{2.17}$$

$$\nabla \cdot \mathbf{B} = 0 \quad \text{Gauss's law for magnetism,} \tag{2.18}$$

$$\nabla \times \mathbf{B} = \mu_0 \left(\mathbf{J} + \epsilon_0 \frac{\partial \mathbf{E}}{\partial t}\right) \quad \text{Ampere's law.} \tag{2.19}$$

where σ is the conductivity, μ_0 the permeability of free space, $\rho_c = \sum_k q_k n_k$ the charge density and $\mathbf{J} = \sum_k q_k n_k \mathbf{u}_k$ the current density.

2.1.4 Magneto-hydrodynamics

Having now a set of equation describing both the motion of electric charges and fluids, one can develop a model for the dynamics of fully ionized plasmas, found for example in the Earth's upper ionosphere or in the solar wind (Baumjohann and Treumann, 1996). When the fact that a plasma is a mixture of electrons and ions is neglected, i.e., the plasma is considered as a single electrically conducting fluid, the model is referred as *Magneto-Hydrodynamics* (MHD). In MHD, the plasma is also assumed to be a good enough conductor so that deviations from overall charge neutrality will be instantaneously shorted out. This implies that MHD is concerned with large scales (low frequency) phenomena and that the electric fields and currents present in the systems are generated by varying magnetic fields.

For a lump of fluid with density ρ, the following equations are required in the MHD model:

- **The continuity equation**: since the plasma is considered as a unique fluid without any creation or loss of particles, the continuity equation is the same as for neutral fluids, i.e. Eq. (2.13).
- **Newton's second law**: the forces acting on the plasma are due to the pressure gradient, the magnetic field and, for generality, the gravity. Note that since the plasma is assumed to be a good conductor, no force due to charge distribution or electric fields have been added here: large currents are supposed to short-out charge separations instantaneously. Newton's second becomes

$$\rho \frac{D\mathbf{u}}{Dt} = -\nabla p + \mathbf{J} \times \mathbf{B} + \rho \mathbf{g}. \tag{2.20}$$

- **Equation of state**: as described in 2.1.3, an equation of state is needed. For example, for incompressible MHD, one can simply use $\nabla \cdot \mathbf{u} = 0$.
- **Electrodynamics equations**: in this fluid description, only low frequency phenomena are considered. It can be shown that the displacement current in Ampere's law is negligible compared to the current $\mathbf{J}$, giving

$$\nabla \times \mathbf{B} = \mu_0 \mathbf{J}. \tag{2.21}$$

Faraday's law, given by Eq.(2.17) and Ohm's law, given by Eq. (2.15), are also needed in order to solve the full set of MHD equations. Here, a special case of MHD called *ideal MHD* is presented. In this *ideal limit*, the plasma is assumed to be an ideal conductor, with $\sigma \to \infty$. In order to keep the current finite, Ohm's law must become

$$0 = \mathbf{E} + \mathbf{u} \times \mathbf{B}. \tag{2.22}$$

This implies that the electric fields are caused by the motion of the plasma across the magnetic fields. An important consequence following from the ideal MHD is that the plasma is *frozen to the magnetic field*, meaning that a lump of plasma initially located on a given field line will stay on the same field line. The derivation of this principle can be found in several plasma books, for example in Pécseli (2012).

The full set of equations for ideal and incompressible MHD, where Eq. (2.22) and Eq.(2.17) have been combined is given by:

$$\begin{aligned}
&\frac{\partial \rho}{\partial t} = -\nabla \cdot (\rho \mathbf{u}) \\
&\rho \frac{D\mathbf{u}}{Dt} = -\nabla p + \mathbf{J} \times \mathbf{B} + \rho \mathbf{g} \\
&\nabla \cdot \mathbf{u} = 0 \\
&\nabla \times \mathbf{B} = \mu_0 \mathbf{J} \\
&\frac{\partial \mathbf{B}}{\partial t} = \nabla \times (\mathbf{u} \times \mathbf{B}) .
\end{aligned}$$

2.1.5 The two-fluid approximation

A plasma can also be seen as a mixture of positively and negatively charged gases. One can for example imagine the possibility for the electrons to move almost freely in an ion background also having its own dynamic. This approach to a plasma is referred to as the *two-fluid approximation* and is applicable to higher frequencies than for MHD. Partially ionized plasmas such as the ones in the ionosphere can typically be described by the two-fluid approximation. In the following section the mathematical description of this model is presented.

For a fluid with mass density ρ_k (related to the number density through $\rho_k = n_k M_k$), the following equations have to be fulfilled for ions and electrons:

- **The continuity equation**: an additional term is introduced in Eq. (2.13) to take into account the possibility for recombination and electron pairs production due to impact of photons and energetic particles. If P_k is the rate of production of charged particles per cubic meter per second and L_k, the rate of loss, the continuity equation becomes (Kelley, 2009)

$$\frac{\partial \rho_k}{\partial t} + \nabla \cdot (\rho_k \mathbf{u}_k) = M_k (P_k - L_k) . \tag{2.23}$$

Since electric charge is a conserved quantity, the total number of electrons gained or lost

must be equal to the sum over all ion species l (over the sum of ions gained or lost), i.e.

$$P_e - L_e = \sum_l N(P_l - L_l). \tag{2.24}$$

- **Newton's second law**: the important body forces acting on the plasma in the ionosphere are the gravitational force $\rho_k \mathbf{g}$, the electric force $n_k q_k \mathbf{E}$ and the magnetic force $n_k q_k (\mathbf{u}_k \times \mathbf{B})$. Hence, the momentum equation can be written as

$$\rho_k \frac{D\mathbf{u}_k}{Dt} = -\nabla p_k + q_k n_k \left(\mathbf{E} + \mathbf{u}_k \times \mathbf{B}\right) + \rho_k \mathbf{g} + \sum_{k \neq l} \mathbf{R}_{kl}, \tag{2.25}$$

  where q_k is the charge and $\mathbf{R}_{kl}$ corresponds to Coulomb collisions with

$$\mathbf{R}_{kl} = n_k M_k \nu_{kl} (\mathbf{u}_l - \mathbf{u}_k) = -\mathbf{R}_{lk} \quad \text{with} \quad l = i, e, \tag{2.26}$$

  with ν_{kl} being the collision frequency between the species k and l. Note that for a collisionless plasma $\mathbf{R}_{kl} = 0$.

- **The equation of state**: again, as for the MHD model, an appropriate equation of state must be chosen. This equation depends on the type of plasma studied. Knowing that a plasma has many properties of an ideal gas (Kivelson, 1995), one could use the ideal-gas law in certain cases, as done by Kelley (2009), and have the pressure and temperature related by

$$p_k = n_k k_B T_k. \tag{2.27}$$

- **Electrodynamic equations**: from Maxwell's equations (see 2.1.3), both Ampere's law (Eq. (2.19)), and Faraday's law (Eq. (2.17)), can be added to complete the set of the equations needed to describe the plasma in the two-fluid model.

The complete set of equations is given by:

$$\frac{\partial \rho_k}{\partial t} + \nabla \cdot (\rho_k \mathbf{u}_k) = M_k \left(P_k - L_k\right)$$
$$\rho_k \frac{D\mathbf{u}_k}{Dt} = -\nabla p_k + q_k n_k \left(\mathbf{E} + \mathbf{u}_k \times \mathbf{B}\right) + \rho_k \mathbf{g} + \sum_{k \neq l} \mathbf{R}_{kl}$$
$$p_k = n_k k_B T_k$$
$$\nabla \times \mathbf{B} = \mu_0 \left(\mathbf{J} + \epsilon_0 \frac{\partial \mathbf{E}}{\partial t}\right)$$
$$\nabla \times \mathbf{E} = -\frac{\partial \mathbf{B}}{\partial t}.$$

2.2 The near-Earth environment

Plasmas are abundant in the solar-terrestrial environment. All matter above about 100 km altitude must be treated using plasma models Cairns (1985). The plasmas in the near-Earth environment are quite diverse and exhibit very different temperatures and density characteristics. In this section, some of these geophysical plasmas are described after having introduced the magnetic field of the Earth. As shown in section 2.1, the behavior of a plasma is controlled by the magnetic field. Hence, an appreciation of the geomagnetic field is essential to understand the motion of the charged particles in the near-Earth system.

2.2.1 The Earth's magnetic field

The Earth has an intrinsic magnetic field with its source located in the center core (Merrill, 2010). The shape of the field is complicated and contains contributions from currents both in the central core of the Earth and in space. However, the main magnetic field can be approximated as a dipole whose axis is tilted with respect to the rotation axis by $\approx$ 10 degrees (Pfaff Jr., 2012). The dipole approximation is sufficient for the considerations here, that is describing the plasma motion due to the magnetic field. Figure 2.2 shows the dipole-shaped field. At high latitudes, the magnetic field lines are almost vertical with respect to the ground while they are horizontal at low latitudes. Due to the offset between the rotation axis and the magnetic axis, the magnetic and geographic poles, as well as the magnetic and geographic equators, are not located at the same place. Using a mathematical model such as the International Geomagnetic Reference Field (IGRF), one can describe the main magnetic field around the Earth. For example, the location of the geomagnetic north pole in 2010 was 80 ° N and 72 ° W, and its magnitude was about 60000 nT.

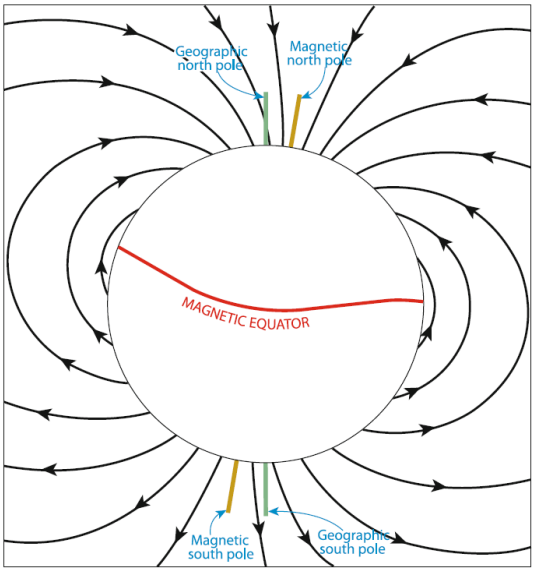

Figure 2.2: The dipole-shape magnetic field of the Earth. The geographic and magnetic poles are not located at the same positions. At high latitudes, the magnetic field lines are nearly vertical with respect to the ground and almost horizontal at low latitudes. Figure from Pfaff Jr. (2012).

Nowadays, the field lines begin in the southern hemisphere of the Earth and close in the northern hemisphere, implying a South-North direction, as shown in Figure 2.2. There has been several direction reversal during the history of the Earth and we might be heading towards a new polarity change (Merrill, 2010).

2.2.2 Geophysical plasmas

The Sun

The Sun is a plasma sphere with a radius of approximately $6.96 \cdot 10^8$ m and a mass of $1.99 \cdot 10^{30}$ kg (Stix, 2004). It consists mainly of hydrogen ($\sim 90\,\%$) and helium ($\sim 10\,\%$) (Priest, 1995). The Sun is composed of a central core, a radiative region and a convective region. The Sun's visible surface is called the photosphere.

The layers above the surface of the Sun are much hotter and comprise the chromosphere and the corona. The outermost layer is the corona and consists mainly of ionized hydrogen (Low, 2001). The corona extends far into the solar system and has a very complicated fine structure containing flares, helmet streamers, filaments, coronal holes etc. all related to the complex magnetic field of the Sun.

The magnetic field activity of the Sun has an 11 years period (Akasofu and Chapman, 1972). During low activity, the magnetic field is dipole-shaped and helmets streamers form a belt of closed magnetic field along the polarity separatrix. During solar maximum activity, the dipole-like symmetry is completely broken and the field is disorganized. The number of sunspots also increases with solar activity, giving raise to more outflow of plasmas (Priest, 1995).

The solar wind

Most of the energy from produced by the Sun arrives to the Earth as photons (Akasofu and Chapman, 1972). However a very highly conductive plasma with relatively high temperature is also escaping from the corona with a supersonic velocity. This plasma is flowing in all directions and is called *the solar wind*. It is essentially composed of protons ($\sim 95\,\%$) with an equal number of electrons per volume and a small percentage ($\sim 4\,\%$) of alpha particles (Hundausen, 1995). At 1 astronomical unit (AU), which is approximately the mean Earth-Sun distance, the density of the solar wind is approximatively $10\,\mathrm{cm}^{-3}$, its temperature is $(7.4 - 8) \cdot 10^4\,\mathrm{K}$ and its average speed is 420 km/s (Lepping et al., 2003).

Since the Sun has an intrinsic magnetic field, the solar wind carries a weak magnetic field of about 5.5 nT at 1 AU (Lepping et al., 2003), which is *frozen into the plasma* (see section about MHD 2.1.4) and form the Interplanetary Magnetic Field (IMF). The solar wind is thus a highly conducting, collisionless, magnetized plasma and, to the lowest order, can be described by the ideal MHD model (see section 2.1.4) (Schunk and Nagy, 2009). The solar wind is streaming outward radially, but due to the rotation of the Sun, the large scale IMF has a complicated spiral form called the Parker Spiral. In addition, due to the dipole-shaped magnetic field of the Sun, open field lines have different polarities in each hemisphere. This implies the existence of the heliospheric current sheet (HCS), a thin region of high current density at the solar equator. Due to the offset of the Sun's axis with the rotation axis, the spiraling HCS wraps into a shape often referred as a ballerina skirt as it changes polarity (see Figure 2.3). Thus an observer on Earth, for example, will see alternatively positive and negative magnetic field regions called *sectors*.

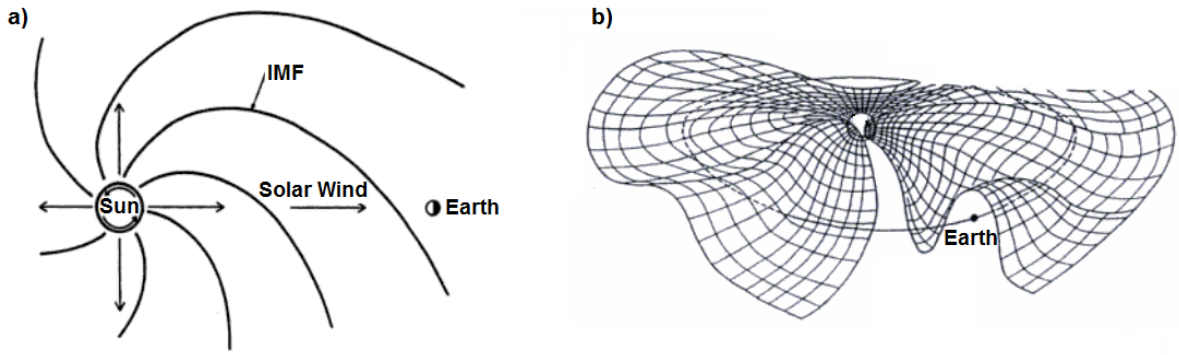

Figure 2.3: Illustrations of a) The Parker Spiral and b) the heliospheric current sheet separating oppositely directed field lines. The *ballerina skirt*-shape is a consequence of the offset between the Sun's rotation axis and the magnetic dipole axis. Figure from Schunk and Nagy (2009).

Two other important features related to the solar wind are coronal mass ejections (CMEs), which are large eruptions of plasmas (Low, 2001) and coronal hole. Coronal holes are regions in the corona with colder, less dense plasma than their surrounding and a magnetic field that opens freely into the interplanetary space. They are known to be the source of the high-speed solar wind and can reach $\approx 800\,\mathrm{km/s}$ (Lepping et al., 2003). Coronal holes usually cover regions around the Sun's poles during periods of low solar activity and can be found everywhere on the corona. Interactions between the fast solar wind and slower solar wind can also create structures called co-rotational interaction regions (CIRS).

Structure of the neutral atmosphere and the main ionosphere

The neutral atmosphere and the ionosphere of the Earth can be considered horizontally stratified to first order. The layers in the atmosphere are organized by the temperature profile while the structures in the ionosphere are organized by the density. The midlatitudes profiles are shown in Figure 2.4.

The first layer of the neutral atmosphere is called the troposphere and is the seat of all weather systems. The temperature decreases from the ground to approximately 10 km. At this altitude begins the stratosphere, where the temperature starts increasing again due to absorption by ozone of part of the ultraviolet (UV) spectrum of the solar radiation. In the mesosphere, which starts at about 50 km, the temperature decreases again with increasing altitude as a consequence to radiative cooling. The temperature reaches a minimum of $130 - 190\,\mathrm{K}$ at about 90 km. Above this minimum (the mesopause), the temperature increases up to thousands of Kelvins due to absorption of very energetic photons. This region is called the thermosphere.

The neutral atmosphere is bombarded by photons coming from the Sun creating plasma. Solar radiation at UV and EUV wavelengths is capable of dislodging electrons from a neutral gas atom or molecule during collisions. This process is known as photoionization. The plasma density profiles are different for daytime and nighttime condition.

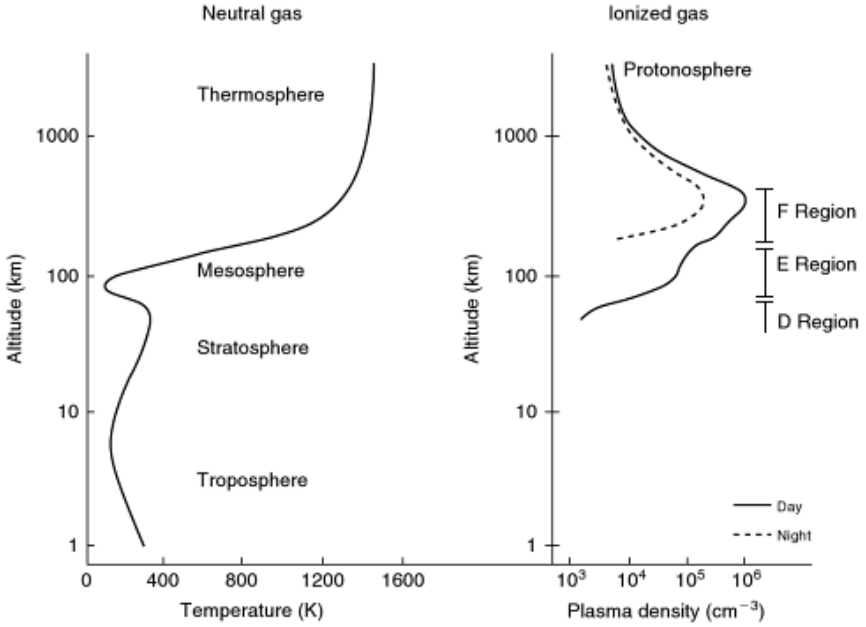

Figure 2.4: Temperature profile of the neutral atmosphere and density profile of plasma for different altitudes. Adapted from Kelley (2009)

During daytime, direct radiation strikes the neutral atmosphere which has an increasing density with decreasing altitude. Thus, more photoionization is occurring at low altitudes implying a decrease of solar radiation intensity. At the same time, both diffusion and recombination, which is the capture of a free electron by a ion, begin to take place as the number of neutrals increase. These processes explain the large scale profiles in Figure 2.4. The region between $150 - 500\,\text{km}$ is called the F region. The maximum of density, the F peak, can attain values such as $10^6\,\text{cm}^{-3}$ around noon. Nearly all the ions are O_+ at this altitude Proelss (2004). Between $90 - 150\,\text{km}$ and below $90\,\text{km}$, the regions are termed the E region and the D region respectively and the dominant ion species in the plasma are NO_+ and O_2^+ (Kelley, 2009).

During nighttime, the profile is similar that of the dayside above the F peak but the density is much reduced at lower altitudes, where molecular ions dominate. This difference is due to the fact that the recombination rate between atomic ions and electrons is much lower than between molecular ions and electrons. The production of molecular ion being curtailed at night, the plasma density will be reduced due to fast recombination between these molecular ions and the electrons. At higher altitudes, the radiative recombinations, producing photons, have a much longer reaction rate than the process described earlier and the concentration of $O+$ can be sustained all night (Pfaff Jr., 2012). Another important source of ionospheric plasma comes from the ionization by energetic particle impact on the neutral gas. A detailed description of this process can be found for example in Pfaff Jr. (2012).

The magnetosphere

When the solar wind encounters the magnetic field of the Earth, it is slowed down and deflected around it. This is a consequence of the frozen in field principle presented in section 2.1.4, implying that the plasma coming from the Sun cannot leave the IMF. The cavity so formed in

the solar wind by the Earth's magnetic field is called the *magnetosphere*. An illustration of the side view of the Earth's magnetosphere and its surrounding is shown in Figure 2.5, where the x-axis points towards the Sun, the y-axis is in the ecliptic plane perpendicular to the Sun-Earth line and the z-axis towards North. These directions correspond to a Geocentric Solar Ecliptic (GSE) coordinate system (Hapgood, 1992) and the electric field and magnetic field components described in this thesis will always refer to this coordinate system.

Since the impinging solar wind is supersonic, a *bow shock* is formed on the dayside (inflowing side) and some of the kinetic energy is converted into thermal energy. There is thus a region located behind the bow shock that is made of denser and hotter plasma than the solar wind. This region is called the *magnetosheath*. The surface separating the magnetosheath from the Earth's magnetic field consists of a current sheet and is called the *magnetopause*.

Due to the dynamical pressure of the solar wind, the Earth's magnetic field is compressed on the dayside and stretched out on the nightside (the side opposite to the dayside) into a long *magnetotail*. Depending on the IMF strength, the IMF direction and the solar wind ram pressure, the location of the magnetosphere can change. The dayside boundary has been observed between ≈ 4.5 to $20\,\mathrm{R_E}$ (Paschmann, 1991).

The plasma contained in the magnetosphere comes mainly from the solar wind and from the ionosphere and is quite unevenly distributed, grouped in different regions with different densities and temperatures (see Figure 2.5). Closest to the Earth is the *plasmasphere*, where the magnetic field lines are closed and filled with cold plasma. Outer of the plasma sphere, at about 2-6 $\mathrm{R_E}$, ions and electrons oscillate back and forth from one hemisphere to another (Baumjohann and Treumann, 1996): this is consequence of a *mirror effect* due to stronger magnetic fields close to the poles (see for example Pécseli (2012) for a description of this phenomenon). This region is called the *radiation belt*. Most of the magnetotail plasma is concentrated in a region called the *plasma sheet*. A more detailed description of the different plasma regions can be obtained for example in Akasofu and Chapman (1972), Sonnerup (1985) or in Proelss (2004).

An important result of the deformation of the Earth's magnetic field by the solar wind is that some of the geomagnetic field lines are no longer closed: in the polar regions, some of them directly connect the Earth and the IMF. The areas which connect via magnetic field lines to the magnetotail lobes are called the polar caps and the indentations separating the closed field lines on the dayside to the open field lines extending into the geomagnetic tail are termed the *polar cusps* (see Figure 2.5). These regions are of particular interest in this study, as it is there that the ICI-2 sounding rocket flew.

The polar cusps are funnel-shaped regions between closed and open field lines of the magnetosphere (Lockwood et al., 1993). They are entirely filled with magnetosheath and ionospheric plasmas (Yordanova, 2005) and are usually situated around magnetic local noon on the high latitude sector of the magnetosphere. Their latitude depends on the shape of the magnetopause. For example, the cusp can be found between $77\,^\circ$ and $90\,^\circ$ invariant latitude (Russell, 2000).

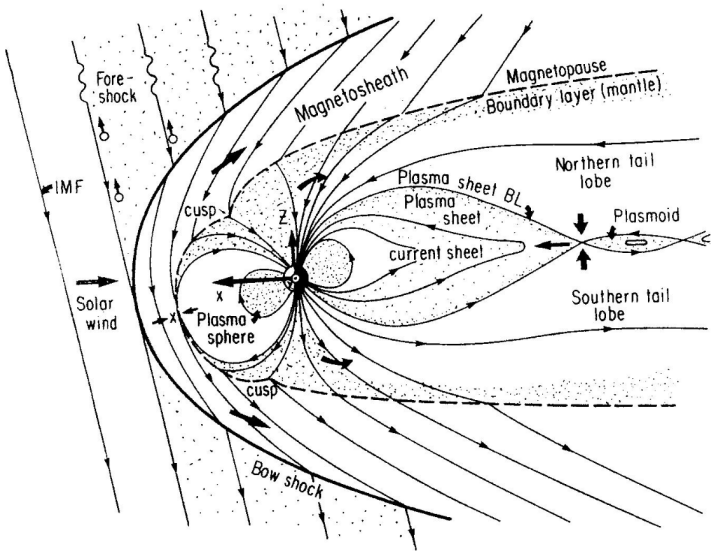

Figure 2.5: Illustration of the magnetosphere and its surrounding. The solar wind is streaming from left to right, deforming the magnetic field of the Earth. Note that this figure assumes that reconnection is occurring (see section 2.3.1), meaning that the IMF connects with the magnetic field of the Earth. Figure from Sonnerup (1985).

The Cusp is a part of the dayside magnetospheric boundary layers, as well as the low latitude boundary layer (LLBL), the entry layer, and the plasma mantle (also called high-latitude boundary layer)(e.g. Haerendel and Paschmann, 1975; Yordanova, 2005). These regions represent important channels for the entry of solar plasma into the the magnetosphere. The LLBL is located at low latitudes, just inside the magnetopause (Siscoe et al., 1991). The plasma contained in the LLBL is a mixture of magnetosheath and maghetospheric plasma. The latter may penetrate the magnetopause via viscous processes (Paschmann, 1991). The entry layer is located just inside the magnetopause and is contiguous with the midlatitude cusp and the mantle (Paschmann et al., 1976). It is filled with turbulent magnetosheath plasma that can diffusively enter into the cusps (Paschmann et al., 1976). The high latitude region poleward of the cusp is the plasma mantle and consists of low-energized magnetosheath plasma (Newell and Meng, 1992).

2.3 Earth-space coupling

The interaction between the solar wind and the magnetopause is complex. In the ideal description, when the plasma is frozen in the field, the IMF and the plasma below the magnetopause are completely separated and no transfer of mass, energy or momentum can be achieved. However, in reality, such transfers can occur. Different models comprising viscous interactions between the solar wind and the magnetopause, or assuming *magnetic reconnection* have been proposed (e.g Dungey, 1961; Axford and Hines, 1961). The coupling between the interplanetary space and the Earth's magnetic field is presented in this section, as well as its consequences on the electrodynamics of the ionosphere.

2.3.1 Transfer from the solar wind through the magnetopause

Magnetic reconnection is a merging of two magnetic field lines with large anti-parallel components. It can only occur when the ideal MHD assumption breaks down, i.e. when the plasma is no longer frozen in **B**. Hence, when the IMF contained in the solar wind is directed oppositely to the magnetic field of the Earth, magnetic reconnection can occur, letting plasma from the solar wind penetrate into the magnetopause. It is thus clear that the direction of the vertical component of the IMF, i.e. B_z (see section 2.2.2) is dictating where the reconnection will occur. Since the Earth's magnetic is directed South-North, an IMF $B_z < 0$ will allow reconnection on the dayside, equatorward of the cusp. In this case, the magnetopause is sometimes referred as *open* (Lepping et al., 2003). For IMF $B_z > 0$, reconnection will occur tailward of the cusp (e.g Crooker, 1992; Chisham et al., 2004). In this work, only the case $B_z < 0$ is presented, since the rocket was launched to study plasma structures associated with dayside reconnection.

The process of reconnection between the solar wind with IMF $B_z < 0$ and the Earth's magnetic field is illustrated in Figure 2.6, showing a side view of the magnetosphere. The IMF merges at the x-line with a closed line of the Earth's magnetic field. This results in an open field line convecting poleward through the polar cap. The convection is due to magnetic pressure and because the open extremity is still embedded in the solar wind flow (Lockwood et al., 1993). The open field lines then reconnects in the tail (see Figure 2.6), implying that particles stream back towards the nightside of the Earth. This return flow maps down to the ionosphere at lower latitudes than the polar caps, in a region called the *auroral oval*. This region is the seat of most of the optical emissions visible for the naked eye (Pfaff Jr., 2012).

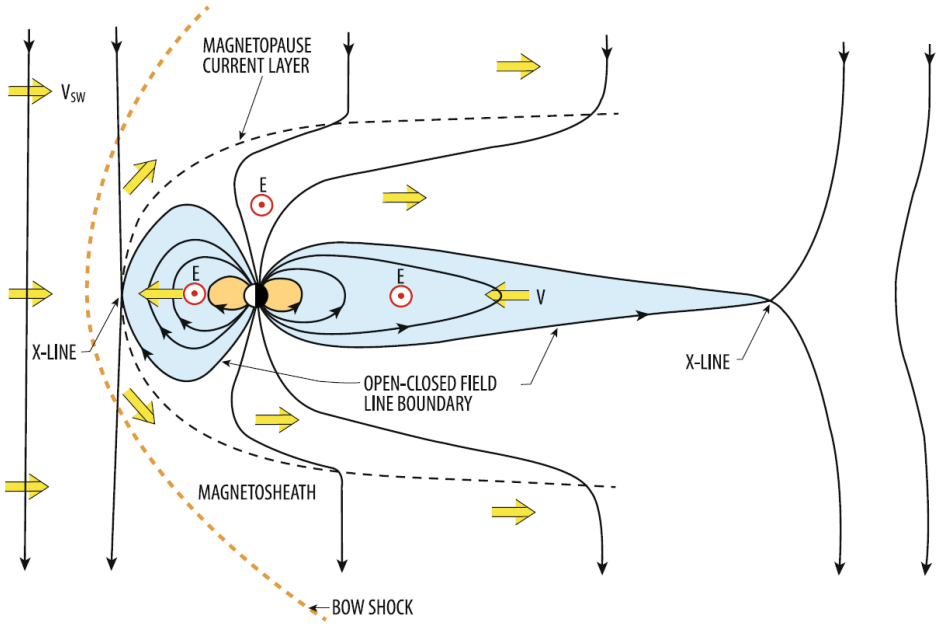

Figure 2.6: Illustration of the magnetosphere for southward IMF. Reconnection takes place at the X-line. On the dayside it connects a closed field line to an open field line, which then convect poleward into the nightisde. The plasma injected at the magnetosheath precipitates down along the new open field lines into the cusps. The dawn-dusk electric field is also shown. Figure from Pfaff Jr. (2012).

The merging allows magnetosheath particles to precipitate along the newly opened magnetic field lines into the ionosphere in the cusps. On the dayside, the principal regions where entry of solar plasma is possible are the boundary layers (section 2.2.2) and their mechanisms are presented, for example, in Haerendel and Paschmann (1975) or in Sandholt et al. (2002). In addition, there are different models of reconnection, where it is either assumed to be a continuous process (Dungey, 1961) or a transient process (e.g Lockwood et al., 1993; Smith, 1994). Extended theory about reconnection can be found in Hughes (1995) or Treumann and Baumjohann (1997).

2.3.2 Large-scale electrodynamics of the high latitude ionosphere

Electric fields and convection patterns

The solar wind can be described by ideal MHD equations (see 2.2.2) and thus, its electric field is given by the relation $\mathbf{E} = -\mathbf{u}_{SW} \times \mathbf{B}$ (from Eq. 2.22), where $\mathbf{u}_{SW}$ is the velocity of the solar wind. When a solar wind with IMF $B_z < 0$ encounters the magnetopause, an electric field directed from down-to-dusk and perpendicular to $\mathbf{B}$ is imposed in the polar cap. This electric field is then mapped down along the magnetic field lines to ionospheric altitudes, causing the plasma to move with the $\mathbf{E} \times \mathbf{B}$-drift in an antisunward direction (Schunk and Nagy, 2009). At slightly lower latitudes, the return flow from the tail into the auroral oval (due to tail reconnection) implies an electric field with opposite direction that in the polar caps.

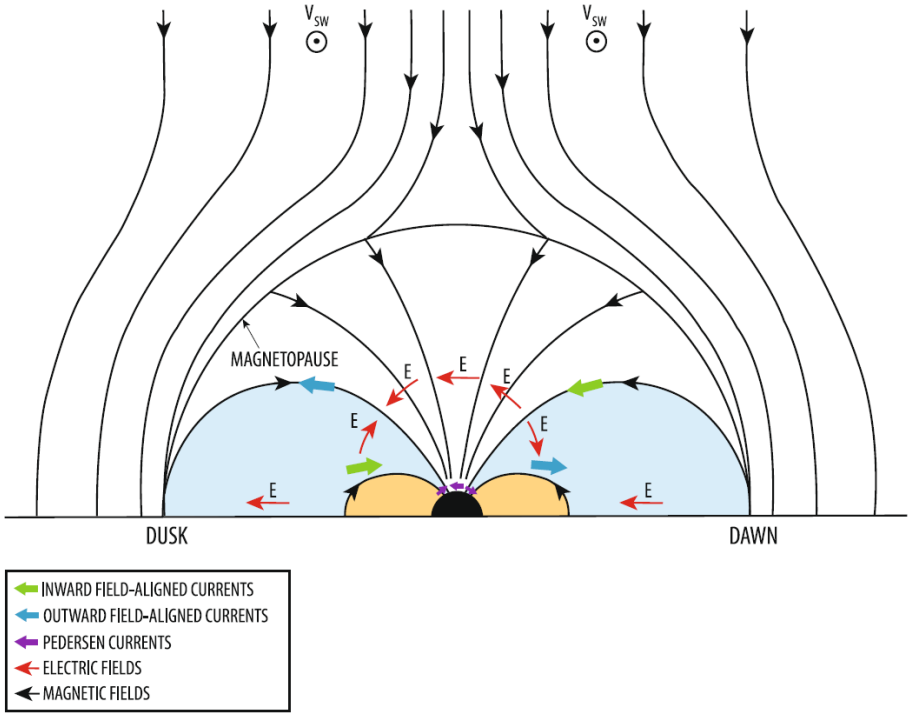

Figure 2.7: Illustration of the northern part of the magnetosphere seen from the tail, looking towards the Sun. The electric fields due to dayside and nightside reconnection for southward IMF are shown. On the boundary between oppositely directed electric fields, currents flow along the magnetic field lines. Figure from Pfaff Jr. (2012).

The different electric fields present inside the magnetosphere resulting from reconnection with IMF $B_z < 0$ are illustrated in Figure 2.7, showing the same configuration as Figure 2.6, but with the perspective of looking from the tail towards the Sun. In the polar caps, the magnetic field lines are approximately vertical and a dawn-dusk electric field maps directly from the magnetosphere down to the ionosphere. On the flanks of the polar caps, the return plasma flow is sunward close to the magnetopause boundary . Hence, when mapping down to the ionosphere, the electric field has a direction opposite to that in the polar caps, i.e., towards the equator on the dawn-side and towards the pole on the dusk-side. These electric fields imply a sunward motion of the plasma in the auroral oval.

The electric fields in the polar cap and in the oval generate a pair of convection cells governing the circulation of the plasma in the high latitude ionosphere. This dual cell pattern is illustrated in Figure 2.9 a), showing the ionosphere from above the North pole.

Experimental results from the Dynamics Explorer-2 (DE-2) satellite showed that these convection cells are highly dependent of the IMF direction (Weimer, 1995). This dependency is not only related to the IMF B_Z component, regulating where reconnection takes place (see section 2.3.1), but it is also due to IMF B_x and B_y. Figure 2.8, displays an example taken from Weimer (1995), where he modeled the high latitude electric potential cells (corresponding to plasma motion lines) with respect to the direction of the IMF for a magnetic field $5.2 < \mathbf{B}_T < 7.25\,\mathrm{nT}$. For IMF $B_z < 0$ and $B_y \approx 0$, the two convection cells are quite similar in size and shape, but when $B_y > 0$ ($B_y < 0$) , the dawn (dusk) cell becomes more important.

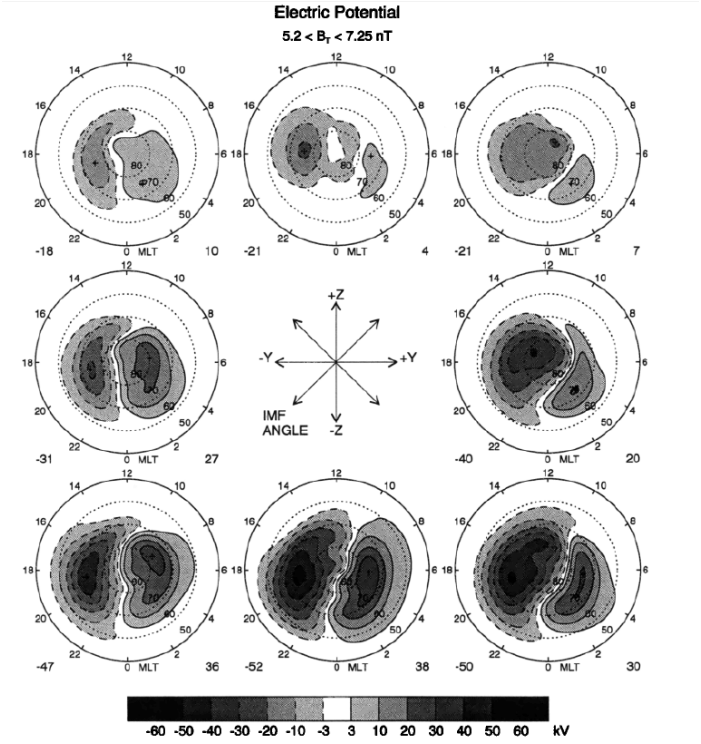

Figure 2.8: Models of the electric potential cells (corresponding to the plasma convection patterns) for different orientation of the interplanetary magnetic field (IMF), when IMF $5.2 < \mathbf{B}_T < 7.25\,\mathrm{nT}$. Figure from Weimer (1995).

Large-scale magnetosphere-ionosphere current systems

On the field lines that separate the oppositely directed electric fields described above, field aligned currents (FAC or *Birkeland currents*) flow between the ionosphere and the magnetosphere (Schunk and Nagy, 2009). Figure 2.9 b) shows an overview of the large scale currents in the high latitude ionosphere. The most poleward FAC are called the *region 1* currents (Cowley, 2000). They are due to stresses on the dayside magnetopoause (Siscoe et al., 1991) and connect the ionosphere to the magnetopause. The *region 1* current flow is directed towards the ionosphere on the dawn-side and out of the ionosphere on the dusk-side of the polar caps. These currents are connected via a *Pedersen* current flowing along **E** across the ionosphere at low altitudes. In the ionosphere, Pedersen currents also flow from the flanks of the polar caps towards the equatorward side of the auroral oval, where they return to the magnetosphere. These currents are named the *region 2* currents and are flowing out of ionosphere on the dawn side, and into the ionosphere on the dusk side (e.g Cowley, 2000; Siscoe et al., 1991).

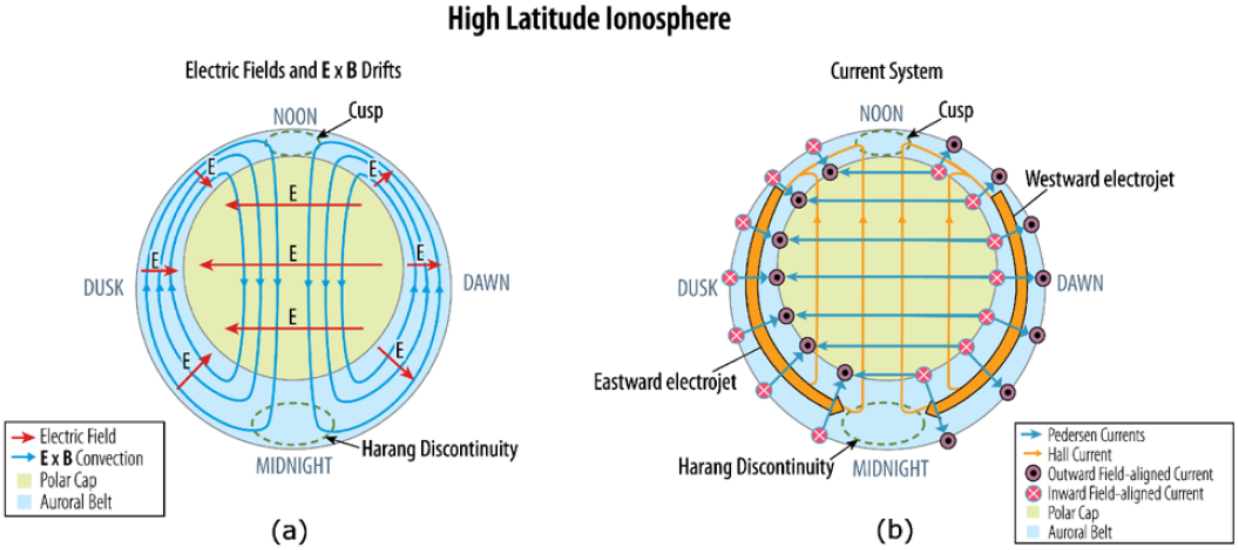

Figure 2.9: Illustration of the idealized large-scale electrodynamics of the polar cap. a) The electric fields and the two convection cells due to the $\mathbf{E} \times \mathbf{B}$-drift are shown. b) The principal large-scale currents are also illustrated. Figure from Pfaff Jr. (2012).

Plasma motion in the ionosphere

As described above, the large-scale plasma circulation is controlled by electric fields with magnetospheric origins. However, the motion of the plasma in the ionosphere is also determined by collisions and by the mobility of the different particles, resulting in currents flowing along and perpendicular to the magnetic field. Thus, to complete this section describing the major currents and plasma circulation in the high-latitude ionosphere, the different drifts resulting from collisions are described here.

By assuming that collisional diffusion is a slow process characterized by time scales longer than the collision times and that the plasma is in equilibrium with the existing force fields, the velocities of the ions and electrons can be calculated from Eq. (2.25).

Let a plasma being quasi-neutral ($n_e = n_i = n$) and having a spatially uniform ion and electron temperature. In the reference frame of the neutrals moving with velocity $\mathbf{u}$ (noted with $'$, and such that $\mathbf{u}'_k = \mathbf{u}_k - \mathbf{u}$), the velocity of species k can be obtained from the expression (Kelley, 2009)

$$\mathbf{u}'_k - \kappa_k \left(\mathbf{u}'_k \times \hat{\mathbf{B}} \right) = -D_k \frac{\nabla n}{n} + \mu_k \mathbf{E}' + \left(\frac{D_k}{H_k} \right) \hat{\mathbf{g}} \tag{2.28}$$

where $\mathbf{E}' = \mathbf{E} + \mathbf{u} \times \mathbf{B}$ and

$$\begin{aligned}
&\kappa_k \equiv q_k B / M_k \nu_{kn}, \\
&D_k \equiv k_B T_k / M_k \nu_{kn}, \\
&\mu_k \equiv q_k / M_k \nu_{kn}, \\
&H_k \equiv k_B T_k / M_k g,
\end{aligned}$$

with $\hat{\mathbf{B}}$ and $\hat{\mathbf{g}}$ being the unit vectors in the direction of $\mathbf{B}$ and $\mathbf{g}$, respectively.

The value $|\kappa_k|$ gives the ratio between the gyroradius and the collision frequency. When the collision frequency is very high ($\kappa_k \ll 1$), the particles will collide many times during one gyro-orbit and the first term of the left-hand side of Eq. (2.28) dominates. The situation is similar to a situation were no magnetic field was present and is described by

$$\mathbf{u}'_k = -D_k \frac{\nabla n}{n} + \mu_k \mathbf{E}' + \left(\frac{D_k}{H_k} \right) \hat{\mathbf{g}}. \tag{2.29}$$

In this case, the velocity is in the same direction as the applied forces. The particles behave as if there was no magnetic field. When the collision frequency is very low ($\kappa_k \gg 1$), the velocity can be separated in two components, one parallel to the magnetic field, and one perpendicular. In the direction parallel to $\mathbf{B}$, the velocity component remains the same, i.e.

$$\left(\mathbf{u}'_k\right)_{\parallel} = \left[-D_k \frac{\nabla n}{n} + \mu_k \mathbf{E}' + \left(\frac{D_k}{H_k} \right) \hat{\mathbf{g}} \right] \cdot \hat{\mathbf{B}}, \tag{2.30}$$

while for the perpendicular direction, we have

$$\left(\mathbf{u}'_k\right)_{\perp} = \frac{1}{\kappa_k} \left[-D_k \frac{\nabla n}{n} + \mu_k \mathbf{E}' + \left(\frac{D_k}{H_k} \right) \hat{\mathbf{g}} \right] \times \hat{\mathbf{B}}, \tag{2.31}$$

which can be rewritten as

$$\left(\mathbf{u}'_k\right)_{\perp} = \frac{1}{B^2} \left[-\frac{k_B T_k}{q_k} \frac{\nabla n}{n} + \mathbf{E}' + \left(\frac{M_k}{q_k} \right) \mathbf{g} \right] \times \mathbf{B}. \tag{2.32}$$

The second term on the right hand side of Eq. (2.32) is charge independent, meaning that both electrons and ions move together with a $\mathbf{E} \times \mathbf{B}$-velocity in a collisionless plasma. The ions and electrons trajectories for $\kappa_k \ll 1$ (collisional) , $\kappa_k \gg 1$ (collision-free) and a combination of both are shown in Figure 2.10. Note that in the intermediate case, the figure shows conditions were the electrons are only subject to the $\mathbf{E} \times \mathbf{B}$-drift.

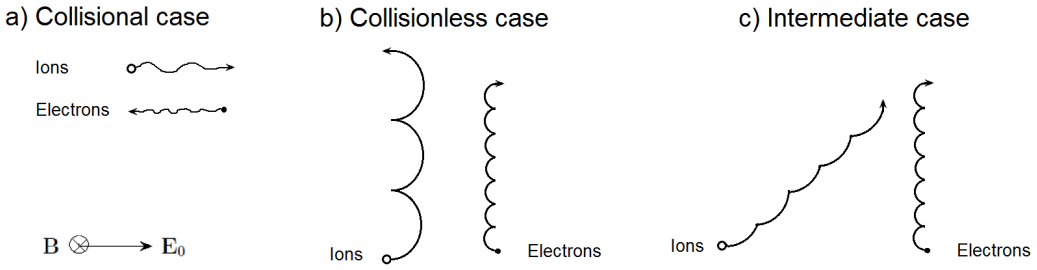

Figure 2.10: Particle motion for collisional, intermediate and collision-free plasma. After Kelley (2009).

Generally, in the high-latitude ionosphere, κ_e remains small in the entire ionospheric altitude range and electrons are subject to the $\mathbf{E} \times \mathbf{B}$-drift at all ionospheric heights. For ions, the collisions are usually so rare above $\approx 250\,\text{km}$ that they move only with the $\mathbf{E} \times \mathbf{B}$-drift at these altitudes. Between approximately 250 km and 125 km altitude, κ_i becomes larger due to the increase of neutral density with decreasing altitude, and the ions motion is a mixture between the $\mathbf{E} \times \mathbf{B}$-drift and a drift along $\mathbf{E}'$ (Cowley, 2000). At altitudes below $\approx 125\,\text{km}$, the ratio κ_i is large and the ions drift in the direction of $\mathbf{E}'$ (Cowley, 2000).

As a direct consequence of these different drifts between electrons and ions, currents must flow perpendicular to the magnetic field in the lower ionosphere. The relation between $\mathbf{J}'$ and $\mathbf{E}'$ can be determined from

$$\mathbf{J}' = ne\left(\mathbf{u}_i' - \mathbf{u}_e'\right). \tag{2.33}$$

This relation can be expressed by $\mathbf{J}' = \underline{\sigma} \cdot \mathbf{E}'$, where the conductivity tensor has been defined as

$$\underline{\sigma} \equiv \begin{pmatrix} \sigma_P & -\sigma_H & 0 \\ \sigma_H & \sigma_P & 0 \\ 0 & 0 & \sigma_0 \end{pmatrix} \tag{2.34}$$

Note that to obtain the form given in Eq. (2.34), $\mathbf{B}$ has been assumed to be along the third component. The parameters σ_0, σ_P and σ_H are called the parallel, the Pedersen and the Hall conductivities respectively and they are given by Kelley (2009)

$$\sigma_0 = ne\left(\mu_i - \mu_e\right) \tag{2.35}$$

$$\sigma_P = ne\left(\frac{\mu_i}{1+\kappa_i^2} - \frac{\mu_e}{1+\kappa_e^2}\right) \tag{2.36}$$

$$\sigma_H = \frac{ne}{B}\left(\frac{\kappa_e^2}{1+\kappa_e^2} - \frac{\kappa_i^2}{1+\kappa_i^2}\right). \tag{2.37}$$

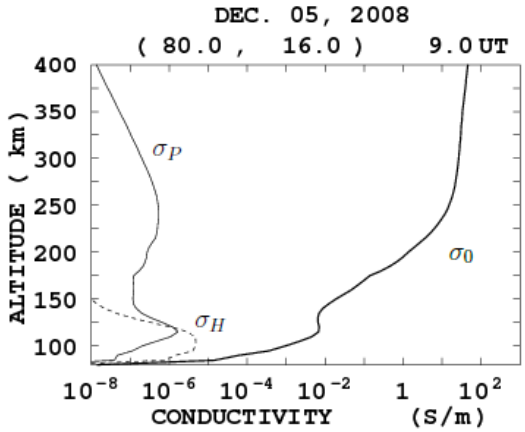

Figure 2.11: Parallel σ_0, Pedersen σ_P and Hall σ_H conductivities over Svalbard (80 °N, 16 °E) on the 5th of December 2008 at 9 UT. This corresponds approximatively to the launch region and time of flight of the ICI-2 sounding rocket. This figure was produced using the International Reference Ionosphere (IRI) model.

The ionospheric conductivity depends on the plasma density and the coupling between the neutrals and the ionized gas. The altitude variation of its components over Svalbard on the 5th of December 2008 (the launch day of the ICI-2 rocket) is presented in Figure 2.11. This figure was obtained using the International Reference Ionosphere (IRI) model, which is an international project created to model several quantities in the ionosphere [1]. The curves shown here present typical values observed in the ionosphere (Pfaff Jr., 2012), with σ_0 much larger than the two other components and $\sigma_H > \sigma_P$ below an altitude $h \approx 130\,\text{km}$ (Cowley, 2000). Note that these values are often integrated over height and defined as Σ_p and Σ_H for the Pedersen and Hall conductivities, respectively.

The currents can be written as

$$\mathbf{J}' = \sigma_P \mathbf{E}'_{perp} + \sigma_H \mathbf{b} \times \mathbf{E}'_{perp} + \sigma_0 \mathbf{E}'_{parallel}. \tag{2.38}$$

The first part of the right hand side of Eq. (2.38) is called the Pedersen current and flows along the electric field but perpendicular to $\mathbf{B}$. This current closes the FAC described in section 2.3.2. The second term of the right hand side is the Hall current and is directed both perpendicular to $\mathbf{B}$ and $\mathbf{E}'$.

By looking at Figure 2.11, one can get an idea about the importance of the different current components in the ionosphere. At high altitudes, where there are only few neutrals, the mobility perpendicular to $\mathbf{B}$ is usually large but since both electrons and ions drift in the same direction, i.e. with the $\mathbf{E} \times \mathbf{B}$-drift, the net current $\perp \mathbf{B}$ is small. At lower altitudes, the direction of the current changes with height, depending on the dominance of σ_H or σ_P. In the direction perpendicular to $\mathbf{B}$, the Pedersen current is dominant above $h \approx 130\,\text{km}$, while the Hall current dominates closer to the ground. These currents close the electrical circuits connecting the ionosphere and the interplanetary space.

[1] The conductivity was calculated using the following link: http://wdc.kugi.kyoto-u.ac.jp/ionocond/sigcal/index.html

2.3.3 Particle precipitation and the visual aurora

At high latitudes, particles can stream along the magnetic field between the upper-atmosphere and the boundary regions of the magnetosphere. The energetic particles precipitating in the ionosphere are a source of both optical emissions and impact ionization, contributing to the plasma environment (Schunk and Nagy, 2009). Depending on their origins, the particles have different energies and precipitate into diverse regions of the ionosphere. Newell et al. (2004) created maps of precipitations, showing the footprints of the different plasma populations under various IMF conditions. They used 11 years of DMSP F6 and F12 (Defence Meteorological Satellites Program) data and Super Dual Auroral Radar Network (SuperDARN) convection data to obtain these maps. An example is shown in Figure 2.12, where IMF $B_z < 0$ and IMF $B_y > 0$. The region of interest in this study is the dayside polar cap/cusp. As described in section 2.2.2, the cusp is a region of direct magnetosheath plasma entry and is recognizable in red. Figure 2.12 also depicts other contributions from the boundary layers such as the LLBL, the mantle (Mant) or the entry layer (OPLL).

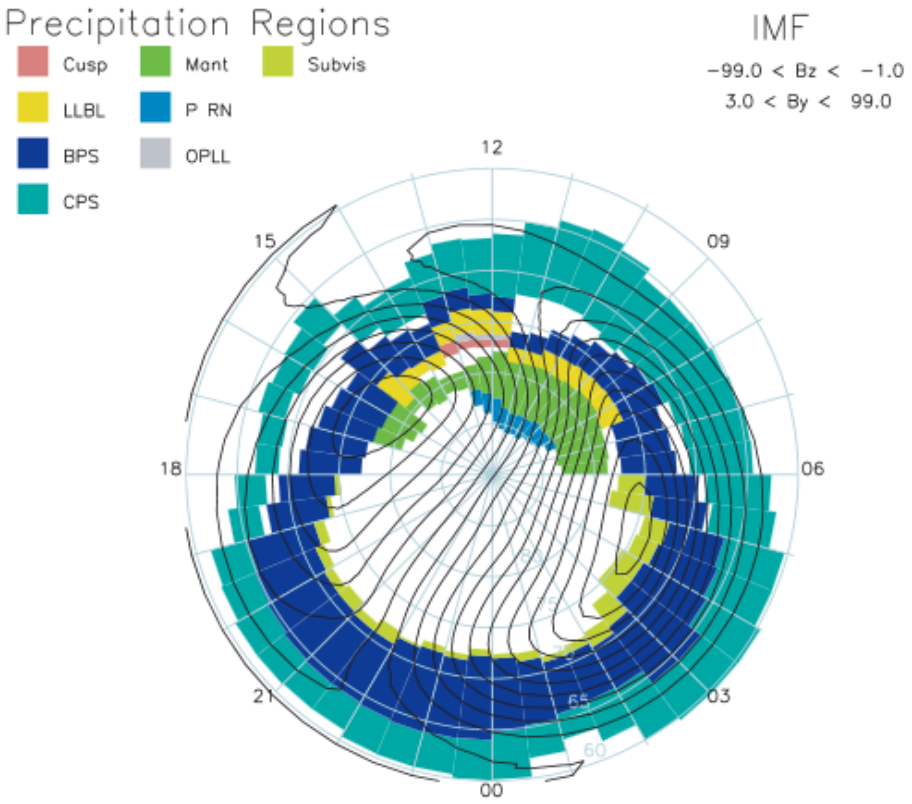

Figure 2.12: Map of the particle precipitation for IMF $B_z < 0$ and IMF $B_y > 0$. The source regions are the cusp, the mantle (Mant), the polar rain (P RN), the LLBL, the open LLBL (OPLL), the boundary plasma sheet (BPS), the central plasma sheet (CPS) and the subvisual region (Subvis). Figure from Newell et al. (2004).

Figure 2.13: Photo of a green aurora. Courtesy of Dr. Tore André Bekkeng, Mai 2013, Following Craig Heinselman.

Optical emissions are often produced when these energetic particles interact with the upper neutral atmosphere. Indeed, the energetic particles precipitating along the magnetic field can both excite neutral atoms or molecules (which release photons when they relax to a lower energy state) and ionized the neutral gas. The auroral optical emissions represent thus the visible signature of the interplay between the solar wind and the Earth's magnetic field. The most common auroras have a yellow-green color and correspond to the emission line $\lambda = 557.7\,\text{nm}$ (Sandholt et al., 2002). They are caused by the interaction between the more energetic electrons with oxygen at the altitude region of $100 - 130\,\text{km}$. An example is shown in Figure 2.13. The other dominant emission is the red glow at $\lambda = 630.0\,\text{nm}$, produced by auroral soft electrons impinging on the oxygen. These *blood red* auroras are generally located at higher altitudes, i.e. above 200 km (Carlson and Egeland, 1995). Note that there are also auroras displaying less common colors such as blue or bright red. These optical emissions are due to the interaction of precipitating particle with other gases such as N_2 (Pfaff Jr., 2012).

Dayside and polar cap auroras

On the dayside, the particles can have direct entry through the magnetopause into the high-latitude ionosphere. The aurora in the cusp is usually due to soft flux of precipitating particles with magnetosheath origins (Newell et al., 2004). It has a diffuse character and its dominant optical emission is the red line ($\lambda = 630\,\text{nm}$). Under normal conditions the cusp auroras are located at $h \approx 250\,\text{km}$ altitude and the energy of the precipitating electrons is lower than 0.2 keV (Carlson and Egeland, 1995). Note however that sporadic enhancements of the green line emission can also occur, typically due to high energy particle with magnetospheric origins (Sandholt et al., 2002).

A detailed description of dayside auroral activity for different IMF configurations can be found in Sandholt and Farrugia (2007) (based on 5 case studies) or in Sandholt et al. (2002, 2004). Here we briefly recall the most important features associated with auroral forms in the cusps and in the dayside polar caps.

The auroral activity on the dayside is directly related to the location of magnetic reconnection and is controlled by the IMF B_z and B_y (e.g. Sandholt et al., 1998; Xing et al., 2013). It

was shown by Sandholt et al. (2004) that two distinctly different auroral configurations were observed. The first one occurs when $|B_z| > |B_y|$ and $B_z < 0$. The aurora is longitudinally wide but latitudinally restricted and has a moderate intensity. In contrast, when $|B_z| < |B_y|$ and $B_z < 0$, the typical auroral activity begins at lower latitudes and moves poleward, as shown in Figure 2.14 for $B_y < 0$. The different steps are associated to the times t_0 to t_4 (after Sandholt et al. (2004)).

The first feature (at t_0) is an equatorward boundary intensification (EBI), accompanied by sequential brightening of fragmented, rayed bands. These bands correspond to particle precipitation with BPS origins. Then (at t_2 and t_3), the cusp aurora expands westward and poleward, resulting in structures called poleward moving auroral forms (PMAFs). Finally, these PMAFs move further poleward (at t_3 and t_4) and fade.

In addition to the spatio-temporal evolution of the auroral activity, Figure 2.14 displays the different auroral forms associated with dayside reconnection (Sandholt et al., 2004)

- *Diffuse aurora* of CPS origin ($\approx 70\,°$MLAT and below).
- Green emission corresponding to a precipitation *void*.
- Fragmented bands due to keV electrons having their source in the *dayside BPS*. This region is also referred to as the *soft electron zone*. Due to their fragmented characteristics, these bands differ from the homogeneous arcs labeled as *nightside BPS*, often observed in the morning or evening sectors.
- The *PMAFs* are located poleward of the BPS aurora. They move poleward and westward for IMF $B_y > 0$. Note that when IMF $B_y < 0$, the dusk-dawn motion is mirrored. PMAFs are considered as a ionospheric signature for transient magnetopause reconnection (see section 2.3.1).

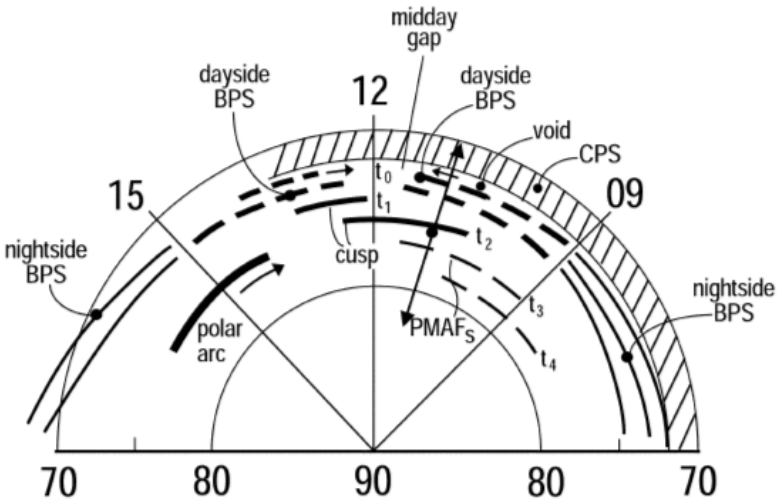

Figure 2.14: Schematic illustration of the dayside auroral activity for IMF $B_y > 0$ and $B_z < 0$. The different auroral forms are named after the location of their particle precipitation origins. The times t_0 to t_4 express the spatio-temporal evolution of the auroral activity. The horizontal numbers refer to the latitudes and the numbers $15 - 12 - 09$ to the time. Figure from Sandholt et al. (2004).

Polar cap patches

Due to magnetic reconnection, the polar ionosphere exhibits different convection patterns and is populated by different plasma structures depending on the IMF B_z orientation. For IMF $B_z > 0$, polar cap arcs are observed (see for example Sandholt et al. (2002)), while for IMF $B_z < 0$, polar cap patches populate the high latitude ionosphere (Carlson, 2012). As mentioned in the introduction, patches exhibit strong density irregularities and are of particular interest for mitigation/circumvention of consequences to satellite communication, GPS navigation and HF communications (e.g. Carlson, 2012; Moen et al., 2013). Here, polar cap patches are introduced. Extended theory can be found for example in Rodger et al. (1994), Carlson (2012) or Moen et al. (2012).

In the polar caps, two types of plasma are generally observed: a low density background and a high density solar EUV ionized plasma. Since the magnetic cusp entry region continuously taps high density plasma of solar wind origin during IMF $B_z < 0$ (due to dayside reconnection), one should expect a continuous tongue of ionized plasma (TOI) beginning at sub-auroral latitudes, crossing the polar cap at F-region altitudes and streaming with the convection pattern described in section 2.3.2 (e.g. Knudsen, 1974; Foster et al., 2005). Yet, the plasma is not continuous but it is chopped into cold islands with high density measuring $\approx 100-1000\,\text{km}$. These islands took the name *patches* due to their patchy appearance in 630 nm images (Carlson, 2012). Patches are driven across the dayside polar caps into the nightside with typical velocities of $\approx 1\,\text{km/s}$. In the return flow on the nightside, the patches are called *blobs* (Tsunoda, 1988).

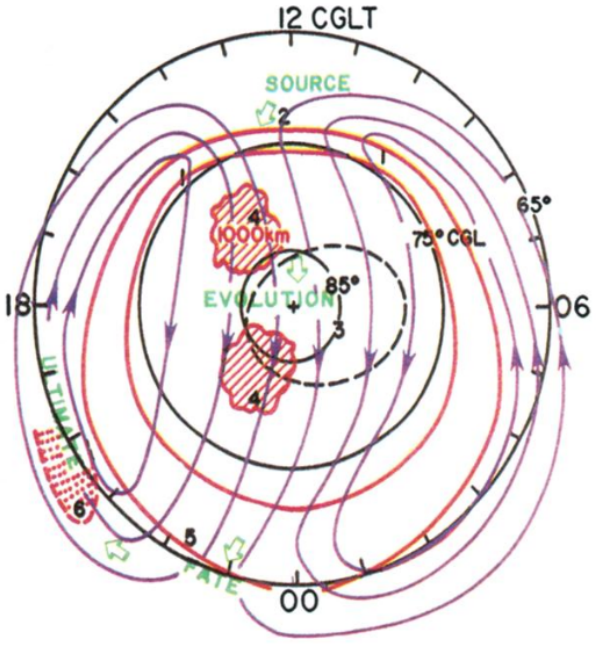

Figure 2.15: Illustration of the northern polar cap activity for IMF $B_y > 0$ and $B_z < 0$. The auroral oval is the red disc at about 65° magnetic latitude. The convection pattern is shown with circular closed lines with arrows overlaid. Two plasma patches are also illustrated, as well as their spatio-temporal evolution: they begin on the dayside at sub-auroral latitudes, move poleward into the nightside and return as blobs at lower latitudes. Figure from Carlson (1994).

By convention, Crowley (1996) defined a patch as having two times (or more) the density of its surrounding. These strong patches are now attributed to a solar EUV production source (Carlson, 2012). However, weak patches ($\sim 10^{11}$ electrons cm^{-3}) can result from soft particle precipitations (Moen et al., 2012). It has indeed been shown by Rodger et al. (1994) that particle precipitation in the cusp does produce plasma density enhancements in the polar cap. Oksavik et al. (2006) also showed that precipitation can produce density enhancements within the polar cap itself.

Many different mechanisms for patch formation have been proposed: we can for example cite changes in convection pattern (e.g. Anderson et al., 1988; Rodger et al., 1994), transient magnetic reconnection (Lockwood and Carlson, 1992) or reconnection driven pulsed convection (Moen et al., 2006). There is no complete agreement on which mechanism is responsible for patch formation and several may apply under one circumstance or another. However, repeated experiments have demonstrated that the majority of the patches (at least in the European sector) were due to the magnetic reconnection mechanism proposed by Lockwood and Carlson (1992) (see Carlson (2012)). In the model of Lockwood and Carlson (1992), transient bursts of reconnection, or flux transfer events (FTE), between the IMF and closed field lines of the Earth's magnetic field allow the open-close boundary to leap equatorward into a region of high density. The boundary is then relaxed and controlled by the transpolar flow within the polar cap, still containing a high density co-rotating plasma that was initially linked to a closed field lines.

Carlson et al. (2006) discovered that velocity shears where inherent patch formation. They then showed, based on experimental results, that plasma patches structuring was initially driven by the velocity-shear instability and not by the gradient-drift instability, as it was believed for decades (Carlson et al., 2007). The gradient-drift instability is expected to dominate later, when the patches have traveled away from their high-speed source and are following the large-scale convection pattern (Moen et al., 2012).

Electron density enhancements in the polar caps are thus highly structured regions, where small scale structures can grow and feed off larger ones, giving rise to radio wave scintillations and coherent HF backscatter targets. Their size can cover large ranges going from several kilometers down to ~ 10 meters (Oksavik et al., 2012; Moen et al., 2012). Since the decameter-scale structures associated with polar patches (or strong density enhancements) are not resolvable for ground based instruments (Moen et al., 2002), it is necessary to use high-sampling rate rockets in order to study them, as it will be discussed later.

To summarize briefly, plasma structures in the near-Earth environment are highly dependent on the coupling between the Earth's magnetic field and the IMF, which is, in turn, highly dependent on the direction of the IMF. Large-scale electric fields and currents are generated from this interaction, dictating both the entry of plasma through the magnetopause and its motion in the ionosphere. When the IMF B_z is directed southward, magnetic reconnection can occur on the dayside, allowing direct entry of plasma in the cusp. As a result, density enhancement or polar cap patches exhibiting irregular structures appear to populate the cusp and the polar cap regions.

2.4 Turbulences in fluids

As noted previously, irregularities covering a wide range of scales are populating the high-latitude ionosphere. The behavior of these plasma structures is still poorly understood but due to their irregular nature, it is believed that fluid-like turbulence theory may be applied to them in order to characterize them (Kintner and Seyler, 1985). In this regard, the basics of fluid turbulence theory are presented here, in order to introduce plasma turbulences and irregularities.

Turbulent processes are part of our everyday life and can be seen, for example, in the flow of a river, in the formation of clouds or in smoke. These phenomena exhibit a lot of structures such as whirls, eddies and filaments with different sizes that seem completely disordered, as can be seen in Figure 2.16, showing the eruption of Mount St. Helen volcano (left) and a simulated Karman vortex street (right). By looking at turbulent flows, we can notice that they are unsteady, chaotic and it seems that many scales are mixed together.

Turbulent processes have been described for more than 500 years and are still very poorly understood, hard to explain and to predict. Leonardo DaVinci used the term *La turbulenza* 500 years ago recognizing two states of fluid motion (Tsinober, 2009). It is since Osborne Reynold's experiment on pipe flow in 1883 that 'modern' research on turbulences really started but we still have problems to give a good definition of turbulences. For example, Tsinober (2009) wrote *"Turbulence is the manifestation of the spatio-temporal chaotic behavior of fluid flows at large Reynolds numbers, i.e, of strongly nonlinear dissipative systems with an extremely large number of degrees of freedom".*
This definition, although containing most of turbulence characteristics, does not help much to predict or describe turbulent flows and it might be helpful to give a few typical features of turbulences:
Turbulent flows have an intrinsic spatio-temporal randomness or irregularity, i.e. they have the property of self-stochastization. This means that there is no need of external (or interior) random forcing to create turbulences. The equations governing them are non-integrable[2] and therefore lack regular behaviors. Turbulent systems are chaotic (but not all chaotic phenomena are turbulent), meaning that they are disordered, sensitive to initial and environmental conditions and can change from "simple" to very complex regimes by *bifurcations*. Their dynamics is thus usually impossible to predict on the long term: two almost identical initial conditions will lead to different sequences. On the other hand, they still have the same statistical properties. Therefore, turbulence is said to be statistically stable (Tsinober, 2009). Another very important feature is that turbulences are non-local; they are characterized by a wide range of degrees of freedom strongly interacting. These features are often pointed as the main reasons for the difficulties in solving the "turbulence problem" and referred as the *3N's : nonlinearity, non-integrability and non-locality.*

[2]There exist no consensus on what integrability means, but most agree that integrable systems are *globally "regular"*, whereas non-integrable ones cannot be solved exactly and show chaotic behaviors (Tsinober, 2009).

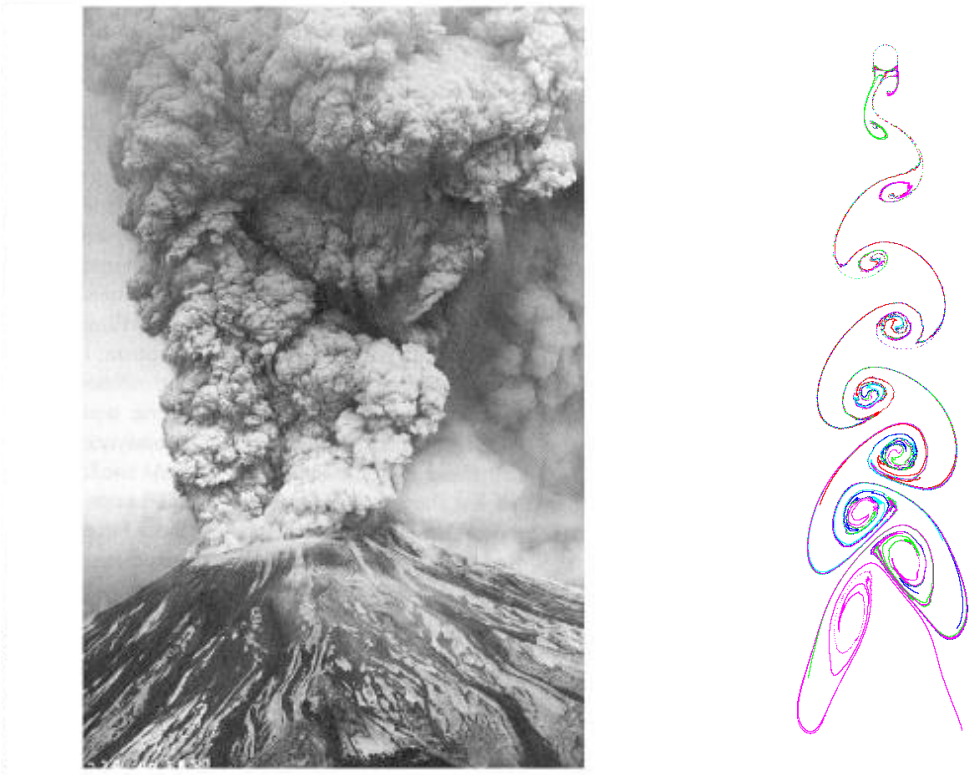

Figure 2.16: Examples of turbulent phenomena showing: (left) the turbulent smoke resulting from the eruption of Mount St. Helen volcano on 18.05.1980, US Geological Survey. Figure from Tsinober (2009); (right) Simulation of a Karman vortex street, which consists of a repeating pattern of vortices caused by the unsteady separation of the flow around a sphere.

Turbulent flows need a source of energy (often at large scales) to be maintained. They are highly dissipative (often at small scales) and strongly diffusive, meaning that they have a great ability to transport or mix fluid efficiently. Turbulent flows are also three dimensional, rotational and intermittent both in space and time.

Several flow regimes exist. They are commonly characterized by a dimensionless number called the Reynolds number Re. It is defined as the ratio of inertial forces to viscous forces, i.e.

$$Re \equiv \frac{Lu}{\nu}, \tag{2.39}$$

where L and u are characteristic length and velocity of the flow respectively. The coefficient $\nu = \mu/\rho$ is the kinematic viscosity and μ is the total viscosity coefficient. Usually, flows with small Re ($\leq O(10^3)$) are defined as *laminar regimes*. Viscous forces dominate and the fluid motion is smooth. Turbulent regimes are associated with high Reynolds numbers. There exists no fixed Reynolds number marking the separation between two types of flows; this separation depends on the speed of the flows, the geometry, the boundary conditions etc.

2.4.1 The origins of turbulences

Turbulent flows are usually thought of as created from some instability in a laminar flow. An *"important common feature of processes resulting in turbulence is that all of them tend to enhance the rotational and dissipative properties of the flow in the process of transition to turbulence" (Tsinober, 2009).* Transition to turbulence is associated with creation of vortices interacting on different scales, with most of the energy on large scales l_0 dissipating on small scales (small eddies) called Kolmogorov's microscales η. As mentioned earlier, the non-linearity of the NSE representing the flow motion leads intrinsically to chaotic behavior. However, it is possible to make a distinction between transition to chaos and transition to turbulences. As a matter of fact, low-dimensional chaotic systems keep their degrees of freedom constant while passing from 'normal' to chaotic regime. This happens typically at an early stage of transition to turbulences. At a later stage, the fluid contains a much higher number of degrees of freedom leading to a drastic change in the flow structure. Despite these difficulties, some statistical properties of turbulent flows are reproducible, meaning that they are statistically stable. Therefore, any theory of turbulence must be a statistical theory, including average, scaling, invariant properties etc. One of the most celebrated theories of turbulences is the Kolmogorov 1941 theory (or K41 theory).

2.4.2 The Kolgomorov 1941 theory

This section will present the process called the Richardson cascade and the two celebrated laws from Kolmogorov's K41 theory, the **two-thirds law** (and **four-third law in Fourier space**). Richardson's hypothesis about fully developed turbulences states that the kinetic energy is continually injected from large scale structures L_0 (integral scales) to small scales (dissipation range) η and then dispatched by viscous stresses (see Figure 2.17). This process is often called *energy cascade* and is described as a multistage process (Davidson, 2006).

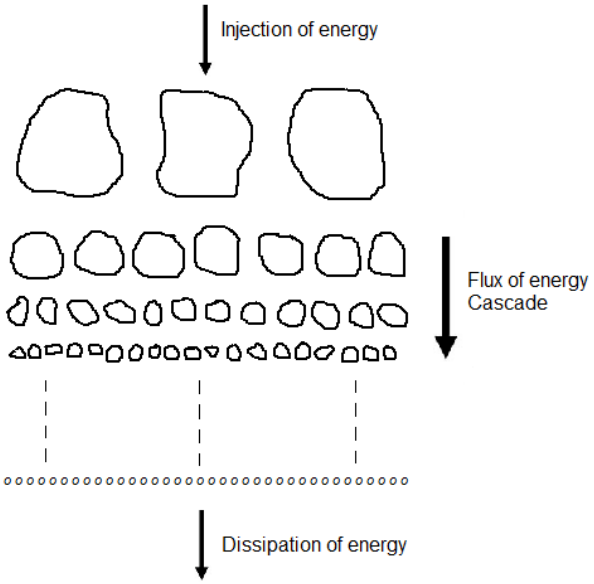

Figure 2.17: Scheme of the Cascade process proposed by Richardson. After Frisch (1995).

Richardson proposed that the main drivers of the cascades on large scales are the inertial forces and that the viscosity becomes important only for small structures, with $Re \approx 1$ based on length scales compared to the dissipation range. Assuming u_L to be the mean velocity of structures of length L (with $L_0 > L > \eta$), the typical time of transfer of energy from scales $\sim l$ to smaller scales is

$$t_L \sim \frac{L}{u_L}, \tag{2.40}$$

The energy flux passing down the cascade is

$$\Pi \sim \frac{u_L^2}{t_L} \sim \frac{u_L^3}{L}. \tag{2.41}$$

In the inertial range, were viscous effects are much smaller than inertial effects, Π must be independent of L and equal to the mean energy dissipation rate ϵ since no direct input of dissipation of energy takes place. Thus, the velocity can be written as

$$u_L \sim \epsilon^{1/3} L^{1/3}. \tag{2.42}$$

The velocity is scale-invariant with exponent $c = 1/3$. We will see later, that this also follows from Kolmogorov's four-fifths law.
At small scales, the viscosity becomes important and the dissipation rate of a flow with velocity u_η and characteristic length η is

$$\epsilon \sim \nu \frac{u_\eta^2}{\eta^2}. \tag{2.43}$$

For homogeneous, isotropic, statistically stable turbulences, the transfer of energy from the 'steady flow' to the larger eddies with length scale L_0 and velocity u_0 must equal the rate of energy transfer at all point in the cascade. Therefore, this flux of energy is also the same in the dissipation range. Thus, we have

$$\Pi \sim \frac{u_0^3}{L_0} \sim \frac{u_L^3}{L} \sim \epsilon \sim \nu \frac{u_\eta^2}{\eta^2} \tag{2.44}$$

Using Richardson's hypothesis about the Reynolds number in the dissipation range, i.e. $Re \approx 1$, values for η can be derived

$$\eta \sim \left(\frac{\nu^3}{\epsilon} \right)^{1/4} \tag{2.45}$$

This length is called *Kolmogorov's microscale*. In this range, viscous dissipation balances energy input due to nonlinear interactions. Its characteristic velocity is

$$u_\eta \sim (\nu \epsilon)^{1/4} \tag{2.46}$$

Even though there are still unanswered questions (can't the cascade go from small structures to bigger structures? Does the cascade have to go through all these steps?) the cascade provides a good intuitive picture of Kolmogorov's 1941 theory and brings out two important assumptions:

the *scale-invariance* within the inertial range and the *localness* of interactions. Kolmogorov made several hypotheses in his paper from 1941. The first one was the so-called *hypothesis of local isotropy* based on his definition of local homogeneity and isotropy[3,4].

The starting point to obtain the famous **two-thirds law** is called the structure function of velocity increment and is defined, for velocity, as

$$S_p(l) \equiv \langle (\delta \mathbf{u}(l))^p \rangle \equiv \left\langle \left\{ [\mathbf{u}(\mathbf{r}+\mathbf{l},t) - \mathbf{u}(\mathbf{r},t)] \cdot \frac{\mathbf{l}}{l} \right\}^p \right\rangle \tag{2.47}$$

where p is an integer, $\mathbf{l}$ is a spatial distance and l its norm. We can then derive the second order structure function

$$S_2(l) \equiv \left\langle (\delta \mathbf{u}(l))^2 \right\rangle \tag{2.48}$$

describing the velocity increment between two points. Kolmogorov's second *similarity hypothesis* (or *Kolmogorov's second universality assumption* (Frisch, 1995, p.75)) states that
in the limit of infinite Reynolds number, all the small-scale statistical properties are uniquely and universally determined by the scale l and the mean energy dissipation rate ϵ.
Thus, for very high Re, the inertial forces dominate. By dimensional analysis, the two-third law can be derived: indeed, the structure function S_2 and the dissipation rate ϵ having dimensions $length^2/time^2$ and $length^2/time^3$ respectively, one can obtain

$$\left\langle (\delta \mathbf{u}(l))^2 \right\rangle = C \epsilon^{2/3} l^{2/3}, \tag{2.49}$$

with C being a universal dimensionless constant. This equation states that the velocity increment between two points distant from l in the inertial range of a turbulent fluid with high Reynolds number is proportional to $l^{2/3}$. This law is very often represented in the Fourier space (see subsection 3.3.2), with $k = 1/l$. The energy spectrum $E(k)$ is then given by

$$E(k) = C_K \epsilon^{2/3} k^{-5/3} \tag{2.50}$$

with C_K a constant. An illustration of relation between the Energy and wavenumber k is shown in Figure 2.18. The slope is constant $p = -5/3$ until the dissipation regime is reached. The two-thirds law (or correspondingly the five-third law) can also be found by using *Frisch*'s hypothesis of *self-similarity* **H2**[5] getting that the second order structure function is proportional to l^{2c}, with $c = 1/3$. Note that this value is the same obtained earlier discussing the Richardson cascade. Many experiments on turbulent flows have given satisfactory results corresponding to the two-thirds law (e.g. Champagne, 1978).

[3] The Kolmogorov (1941a) definition of local isotropy is the following: *The turbulence is called locally-isotropic in the domain G, if it is homogeneous and if, besides, the distribution laws mentioned in Definition 1 are invariant with respect to rotations and reflections of the original system of coordinate axes.*
Kolmogorov's Definition 1 describes local homogeneity and states the invariance of the distributions F_n on space and time translations and Galilean transformation.(Tsinober, 2009)

[4] Frisch gives a relatively similar hypothesis, which he calls **H1**:
H1 *In the limit of infinite Reynolds numbers, all the possible symmetries of the Navier-Stokes equation, usually broken by the mechanisms producing the turbulent flow, are restored in a statistical sense at small scales and away from boundaries* (Frisch, 1995, p.74)

[5] **H2** *Under the same assumptions as in H1, the turbulent flow is self-similar at small scales, i.e, it possesses a unique scaling exponent h.*

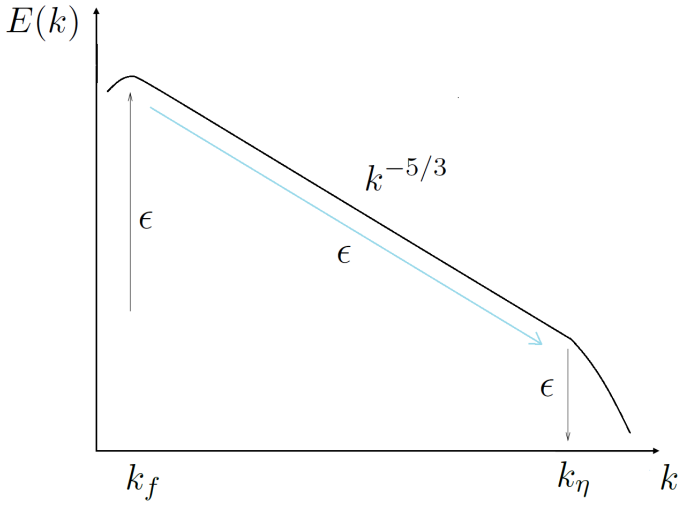

Figure 2.18: Scheme of the energy cascade process predicted by Kolmogorov's 5/3-law. The energy is injected at k_i and decreases with a constant slope $p = -5/3$ for increasing wave number k, until the dissipation scale k_η is reached.

2.4.3 Two-dimensional cascade in fluids

The cascade hypothesis can also been applied to two-dimensional (2D) fluids (e.g Kraichnan, 1967; Batchelor, 1969). Two-dimensional Navier-Stokes turbulences can be particularly important whenever the system presents strong anisotropy in the velocity distribution. It can for example be applied to large-scales meteorological flows, where the horizontal length-scales are much larger than the atmospheric height-scales (e.g. Leith, 1971). In addition, 2D turbulences play an important role in the dynamics of strongly magnetized plasmas (Similon and Sudan, 1990).

For a two-dimensional isotropic and incompressible flow, the vorticity ($\omega = \nabla \times \mathbf{u}$) of each fluid element is an inviscid constant of motion (Kraichnan and Montgomery, 1980). Thus, the mean-square vorticity, called the *enstrophy*, is also an inviscid invariant.

Hence, there are two potentially cascadable quantities, i.e. the kinetic energy per unit mass (as for the 3D cascade) and the enstrophy. Kraichnan (1967) showed that there exists two local similarity laws for $E(k)$, corresponding to well defined inertial ranges. This means that, in k-space, there is one range where $\epsilon(k) = \text{const}$ and $\eta(k) = 0$ and another range where $\epsilon(k) = 0$ and $\eta(k) = \text{const}$. The former corresponds to a constant cascade of energy while the latter corresponds to a transfer of enstrophy without any cascade of energy. Additionally, Kraichnan (1967) argued that both cascades should be oppositely directed in k-space, meaning that the signs of ϵ and η are opposite in their respective inertial ranges. He also claimed that the enstrophy cascades in the same direction as the *direct cascade* for 3D fluids (from small k to large k), while the energy should cascade in the inverse direction (from larger k to smaller k).

Hence, considering a forcing (or injection) band k_f isolated from both the dissipation scale k_η and the large scales structures k_0, one can get a dual-slope power spectra with two inertial ranges (Kraichnan, 1967)

$$E(k) = C_K \epsilon^{2/3} k^{-5/3}, \quad k_0 \ll k \ll k_f \tag{2.51}$$

for the energy and

$$E(k) = C'_K \eta^{2/3} k^{-3}, \quad k_f \ll k \ll k_\eta \tag{2.52}$$

for the enstrophy. A sketch of this dual-slope cascade is shown in Figure 2.19.

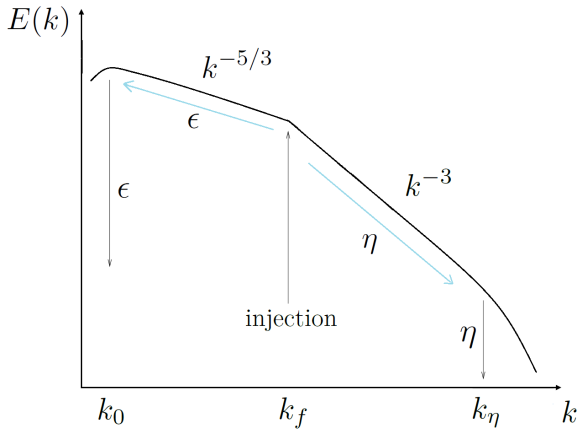

Figure 2.19: Scheme of the dual-slope energy cascade process for a 2D fluid. Two inertial regimes are found separated by a forcing bound. One of the cascading quantity is the energy flux (ϵ), which is transferred from the injection band k_f to smaller wavenumbers, i.e. k_0. The other quantity is the enstrophy (η) and it cascades from the injection band to the dissipation range k_η.

2.5 Electrostatic turbulences in plasmas

The theory of Kolmogorov has had a remarkable success for fluid turbulences (e.g. Frisch, 1995; Kintner and Seyler, 1985). Since plasmas can often be described by a fluid approximation at large scales, one can ask oneself if they exhibit irregularities in the same way as Navier-Stokes turbulences and if the same scaling laws can be applied to obtain the energy cascade. There has indeed been some progress in studying plasma turbulence theory stressing the homology between fluid and low-frequency plasma turbulences allowing an easy and straightforward establishment of the spectrum in the inertial ranges (Similon and Sudan, 1990). However, there exist many differences in fluids and plasma that require some attention. Plasmas have generally more than one invariant (e.g. energy, enstrophy, helicity, etc.). Furthermore, in plasmas, new unstable modes at short wavelengths can grow and feed off larger-scale unstable modes. This means that the k-space can be filled with different spectral characteristics at different regions (Similon and Sudan, 1990). Another important feature is due to the magnetic field, which can create strong anisotropy. The fluctuations vary very fast along the magnetic field but slowly across. However, most of the spectrum should be isotropic perpendicular to $\mathbf{B}$.

Figure 2.20: Photograph of an auroral display taken from a high altitude satellite over Scandinavia and exhibiting highly disordered structures resembling a turbulent fluid. The center-to-center distance of the two white dots at the bottom of the figure is 1220 km and the diameter of each dot is 100 km. Figure from Kelley and Kintner (1978).

Based on the homology between fluids and plasmas, an experimental device conceived to study plasma turbulences in the ionosphere must rely on measurements of the velocity fields, in the same way as it is done for turbulence in fluids. In low β plasmas, i.e. $\beta \ll 1$, where β is given by Eq. (2.5), velocity fluctuations are electrostatic and equivalent to electric field fluctuations ($\mathbf{u}_D = \mathbf{E} \times \mathbf{B}/B^2$). The electric field fluctuations can thus be studied in order get information about the velocity. Passive quantities which are moved by the velocity field can also give indirect insights in the dynamics of the plasma. A typical example of such a passive quantity in plasma is the electron density, which is referred as a *passive scalar*. In this thesis, fluctuations in the electron density were studied.

2.5.1 Plasma macroinstabilities in the ionosphere

Experiments using radars, satellites and sounding rockets have confirmed that the ionosphere hosts strong density irregularities from scale lengths of tens of kilometers to a few meters (e.g. Kivanc and Heelis, 1997; Moen et al., 2002, 2006; Oksavik et al., 2012). The origins of these irregularities is very likely a complex process of which only part is turbulence (Kintner and Seyler, 1985) and several instability mechanisms described by macroscopic plasma models are believed to have a triggering effect on the plasma structures.

Hence, in this section, some macroscopic instability mechanisms are briefly described. All of them are known to lead to turbulence and have been proposed as potential candidates for the observations of ionospheric turbulences, although there is no consensus on to which mechanism is related to which plasma structuring (Kintner and Seyler, 1985). The instabilities presented here comprises the *Rayleigh-Taylor instability* (RT), the *gradient-drift instability* (GDI) (also referred as the $\mathbf{E} \times \mathbf{B}$ instability), the *current-convective instability* (CC) and the *Kelvin-Helmoltz instability* (KH). Note that there exists many more instabilities, but we decided to focus on these mechanisms, as they are the most probable mechanism in the F-region high latitude

ionosphere, and as it was, for instance, also done by Kintner and Seyler (1985).

This section starts with a brief explanation of the generalized RT instability, which is believed to occur mostly in the equatorial regions (Kelley, 2009) and is less present at high-latitudes. However, it is intuitive and helps understanding the $\mathbf{E} \times \mathbf{B}$ and the CC instability.

The Rayleigh-Taylor instability

The mechanism of the Rayleigh-Taylor instability can be understood with the scheme shown in Figure 2.21. Let us consider a density gradient in the x direction (represented by a step function with density n_1 above the interface and $n_2 = 0$ below) with a small perturbation. The gravitational force is directed downward and the magnetic field into the page, i.e. along the z axis. Assuming that the plasma is nearly collisionless, Eq. (2.32) can be applied, i.e.

$$(\mathbf{u}_k')_\perp = \frac{1}{B^2}\left[-\frac{k_B T_k}{q_k}\frac{\nabla n}{n} + \mathbf{E}' + \left(\frac{M_k}{q_k}\right)\mathbf{g}\right] \times \mathbf{B}. \tag{2.53}$$

It is thus possible to determine the electrical current due to pressure gradients and gravity. The pressure-driven current is perpendicular to the density gradient and flows parallel to the perturbed density. It is divergence free and no perturbation electric field is created. The current due to the gravitational force depends on the mass M_k, and since the mass of the ions is larger than the mass of the electrons, the ion velocity dominates. Referring to Figure 2.21, the net current is horizontal, in the $\mathbf{y}$ direction and is given by

$$J_y = \frac{nMg}{B}, \tag{2.54}$$

where J_y is the component of $\mathbf{J}$ in the $\mathbf{y}$-direction (see Figure 2.21). The gravitational drift of ions will cause positive charges to pile up on one side of the perturbation, as illustrated in Figure 2.21. The depletion of ions causes negative charges to build up on the other side of the ripple, creating an electric field $\delta\mathbf{E}$, which will in turn create upward and downward plasma drifts (represented in Figure 2.21 as $\delta\mathbf{E} \times B$). This system is unstable when $\mathbf{g}$ and ∇n are oppositely directed.

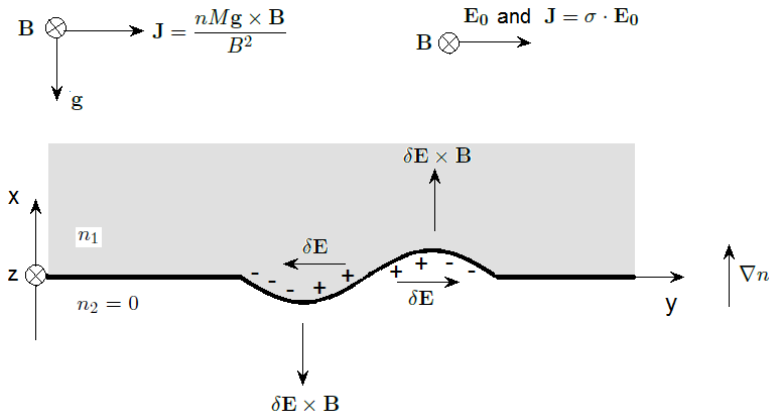

Figure 2.21: Mechanism of Rayleigh-Taylor instability. A dense plasma is supported by a less dense plasma. After Kelley (2009).

The Gradient-Drift Instability (GDI) and Current-Convective (CC) instability

At high latitudes, the gravity has almost no effect on plasma structures since it is almost along **B**, but the electric field can be the driving force for plasma structuring. This electric field-driven instability is referred to as the $\mathbf{E} \times \mathbf{B}$ instability and occurs when $\mathbf{E}' \times \mathbf{B}$ has a component parallel to ∇n. This is equivalent to say that the local convection velocity is in the same direction as the density gradient. The $\mathbf{E} \times \mathbf{B}$ instability can be intuitively understood by looking at Figure 2.22, which reassembles the scheme for the RT instability. The density gradient is in the **x** direction, the background first order electric field $\mathbf{E}_0$ is in the **y** direction and the magnetic field is in the **z** direction (The "'" was dropped for simplicity). When the density profile is slightly perturbed, the pattern associated with the perturbation of the ions will drift in the Pedersen direction in the ionosphere, leaving the electrons behind them. This results in a charge separation and alternating polarization electric field $\mathbf{E}_p$. The resulting $\mathbf{E}_p \times \mathbf{B}$ is amplified by moving from dense plasma to less dense plasma and inversely (moving from low density plasma to denser plasma). This situation is unstable, as it was for the RT instability.

Both analytical and numerical simulations show that high-latitude plasma enhancements can be driven unstable through the $\mathbf{E} \times \mathbf{B}$ instability, generating density and electric field irregularities with scale sizes of kilometers to tens of meters (e.g. Keskinen and Ossakow, 1983; Tsunoda, 1988; Gondarenko and Guzdar, 2004). The resulting irregularities take the form of striation-like figures, or *elongated fingers* (Keskinen and Ossakow, 1983; Gondarenko and Guzdar, 2006).

For the one-dimensional collisional ($\gamma_{GDI} \ll \nu_{in}$) *flute mode* case, with $\mathbf{k} \cdot \mathbf{B} = 0$, the linear growth rate of the GDI is (e.g Ossakow et al., 1978; Tsunoda, 1988; Sojka et al., 1998)

$$\gamma_{GDI} = \frac{v_0}{L}, \tag{2.55}$$

where $L = [(1/n)(\mathrm{d}n/\mathrm{d}x)]^{-1}$ is the typical gradient length scale, v_0 is the magnitude of the velocity relative to the neutrals, referred as the *slip velocity*. When there is no neutral wind, the slip velocity is $v_0 = E_0/B$. For collisionless plasmas satisfying $\gamma_{GDI} \gg \nu_{in}$, ion-inertial effects are included and the growth rate becomes (Ossakow et al., 1978)

$$\gamma_{GDI} = \left(\frac{v_0 \nu_{in}}{L}\right)^{1/2}. \tag{2.56}$$

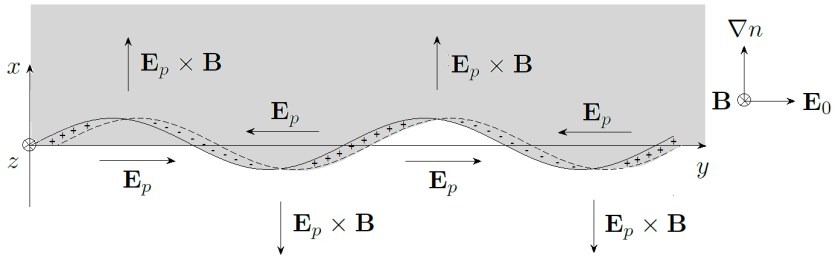

Figure 2.22: Mechanism of F-region gradient-drift instability. The dashed line represents the ions density contour, while the solid line represents the electron density contour. The scheme represents a coordinate system drifting relative to the neutrals. After Tsunoda (1988).

The gradient-drift instability results from a coupling between a density gradient perpendicular to the magnetic field and the convective electric field. When field aligned currents are included, plasma gradients stable to the $\mathbf{E}\times\mathbf{B}$ instability can be driven unstable by the current convective instability. The CC instability results from polarization electric fields that are set up to maintain current continuity perpendicular to the density gradient. A current $\mathbf{j}_{\parallel}$ and a component of the wavevector parallel to the geomagnetic field are thus required. The current of interest is $\mathbf{k}\cdot\mathbf{j}_{\parallel}$, implying a relative drift between ions and electrons which gives raise to polarization fields (Keskinen and Ossakow, 1983). The motion of the $\mathbf{E}_p \times \mathbf{B}$ is then similar to Figure 2.22. It is worth noticing that the CC instability rarely overcomes the stabilizing effects of a configuration stable to the gradient-drift instability (Kelley, 2009). The parallel drift velocity needed for the CC instability to take place refers to field aligned current carried by thermal plasma (Tsunoda, 1988). For a fixed $\mathbf{j}_{\parallel}$, the parallel velocity is inversely proportional to n and, at F-region altitude and average $\mathbf{j}_{\parallel}$, the density is usually too high to create unstable conditions (Tsunoda, 1988).

Kelvin-Helmoltz (KH) instability

Another macroinstability that has often been invoked with high latitude ionosphere irregularities is called the Kelvin-Helmoltz instability (e.g. Keskinen et al., 1988; Basu et al., 1988; Carlson et al., 2008). This instability is not only relevant for polar cap arcs containing inherent flow shears, but it is also believed to be a dominant mechanism in patch formation in the cusps (Carlson, 2012).

The KH instability is hydrodynamic in nature and also occurs in neutral fluids (Kintner and Seyler, 1985). It results from velocity-sheared plasma flows perpendicular to the magnetic field (Kintner and D Angelo, 1977). Figure 2.23 shows the geometry of the problem when two media move in opposite directions. When the shear is sufficiently large, the KH instability can occur along the interface (Treumann and Baumjohann, 1997). A complete theory of this instability at high-latitude can been found in Keskinen et al. (1988).

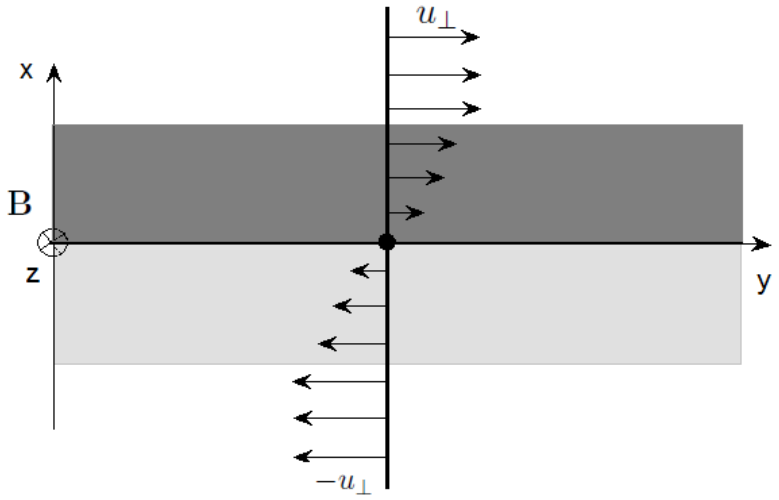

Figure 2.23: Illustration of a plasma configuration which might lead to the Kelvin-Helmoltz instability: The KH can grow on the interface separating two oppositely directed flows.

The growth rate of the KH instability can be estimated from Keskinen et al. (1988). For ionospheric applications, the maximized KH linear growth rate is proportional to the velocity difference $\Delta \mathbf{v_{plasma}}$, and a velocity difference scale length L (Carlson et al., 2008)

$$\gamma_{KH} = 0.2 \frac{\Delta v_{plasma}}{L}. \tag{2.57}$$

2.5.2 Characterization of instabilities by power-laws

In-situ experiments have shown that the density fluctuations in the high-latitude ionosphere exhibited power-law spectra (e.g. Dyson et al., 1974; Phelps and Sagalyn, 1976; LaBelle and Kelley, 1986; Basu et al., 1988, 1990; Mounir et al., 1991). Theoretical work and simulations have also been done for the different instabilities cited above to obtain spectral indices. The derivations of the power-laws expected for the GDI, the CC and the KH instabilities are reviewed in Kintner and Seyler (1985) and his results are given in Table 2.1 for both the electron density and the electric field. In addition, Kintner and Seyler (1985) present the spectral slopes expected for the low-frequency drift wave (DW) instability. DW are waves driven by inhomogeneities in the plasma, such as gradients in density or temperature. They propagate transverse to the gradients and can be driven unstable. In this section, the results shown in Table 2.1 for the electron density are described, forming a reference for comparison with the observations made by the ICI-2 sounding rocket.

The equations governing the GDI and the CC are similar and based on collisional, macroscopic plasma models. There is thus no difference between the features of the nonlinear evolution of the GDI and the CC. Note also that the essential dynamics of the GDI and the RT irregularities are identical and the same power laws should be obtained (Sudan and Keskinen, 1984). There has been two theories concerning the spectrum of the equations governing the GDI (also the CC, and the RT) having both supportive evidences from both simulations and observations (Kintner and Seyler, 1985).

One spectral theory (which was initially formulated for the RT) states that the indices are due to coherent mode coupling, which are likely to result in steepened structures observationally (Chaturvedi and Ossakow, 1977). The slopes expected from this theory are $p = -2$. Indeed, the theory suggests that the sharp gradients of the finger-like structures are approximated by step functions, whose Fourier transform gives $p = -2$, and that diffusion smoothes the step functions. Hysell et al. (1994) also argued that the power spectra were due to steepened, shock-like structures superposed with diffusion at small scales.

Another theory is based on turbulence and scaling law theory in two dimensions (Kintner and Seyler, 1985). Using an extension of Kolmogorov's theory, Sudan and Keskinen (1984) developed a unified treatment of the power spectrum for intermediate-scale electron density fluctuations in the equatorial and high-latitude ionosphere. They concluded that the spectral slope in two dimensions should be $p_{2D} = -8/3$. Sudan and Keskinen (1984) argued also that this would correspond to $p = p_{2D} + 1 = -5/3$ when measured by a spacecraft. In addition, Kintner and Seyler (1985) used dimensional analysis to obtain an inverse cascade at larger scale, giving $p = 1$. Thus, for the GDI and the CC, one can get a direct cascade

$$E(k) = C_K \epsilon^{2/3} k^{-5/3}, \quad k_f \ll k \ll k_\eta \tag{2.58}$$

and an inverse cascade

$$E(k) = C'_K \eta^{2/3} k^{-1}, \quad k_0 \ll k \ll k_f. \tag{2.59}$$

Note however that Kintner and Seyler (1985) argued that the inverse cascade range was suspect and might only be due to the linearization of the equations. They also state that more theoretical work should be done.

The equations governing inertial plasma associated with the Kelvin-Helmoltz instability are closely related to the Navier-Stokes equations and hence, the power spectrum of the electron density for the KH is similar to the spectrum for passive scalar in 2D fluid turbulences (Kintner and Seyler, 1985), i.e.,

$$E(k) = C_K \epsilon^{-1/3} k^{-5/3}, \quad k_0 \ll k \ll k_f \tag{2.60}$$

and

$$E(k) = C'_K \eta^{1/3} k^{-1}, \quad k_f \ll k \ll k_\eta. \tag{2.61}$$

The indices for the GDI and the KH are similar, but in the different frequency ranges (direct and inverse cascade). From Table 2.1, one can see that some ambiguities can occur when calculating the spectral indices for only the electron density. Hence, the electric field power spectra should also be computed in order to obtain a better knowledge about the different instability mechanisms.

The DW turbulence are believed to grow on larger scale structures, as a secondary process (e.g. LaBelle et al., 1986; Similon and Sudan, 1990). The slopes of the power spectrum of the electron density associated with DW processes are steeper than for the other irregularities (see Table 2.1).

In his derivation, Kintner and Seyler (1985) assumed idealized situations where the injection band was narrow and well separated from the dissipation region. For low-frequency phenomena, the effective dissipation scale is near the ion gyroradius (Kintner and Seyler, 1985).

The spectral indices mentioned in this section provide a basis for comparison and for the discussion of the results obtained using ICI-2 density data. They also show the importance to consider several quantities, for example both the electron density and the electric field fluctuations, when characterizing the power spectra.

Type of spectrum	**GDI/CC**	**KH**	**DW**	**Type of Cascade**
$\Delta Ne/Ne$	$-5/3$	-1	-5	Direct
	-1	$-5/3$	$-11/3$	Inverse
ΔE	$-5/3$	-3	-3	Direct
	-1	$-5/3$	$-5/3$	Inverse

GDI : Gradient-Drift Instability
CC : Current-Convective Instability
KH : Kelvin-Helmoltz Instability
DW : Drift waves

Table 2.1: After *Kintner et al., 1985.*

3 Instrumentation and Data Processing

In this chapter, the set of instruments used in this study is presented as well as the data analyzing techniques. The main quantity analyzed was the electron density measured by the Investigation of Cusp Irregularities 2 sounding rocket. Thus, emphasis is put on the description of the ICI-2 rocket and the *multi-Needle Langmuir Probe* system, which was the instrument collecting the data. Spectral analysis techniques comprising both Fourier and wavelet transforms are also presented here, as well as some general assumptions and considerations regarding the study of plasma structures using spacecrafts.

3.1 Instruments providing the space physics context for the ICI-2 flight

Rocket data without any knowledge about the environment in which the spacecraft flew do not provide enough information for discussing the physical phenomena occurring. Hence, for completeness, this chapter starts with a section briefly describing the different ground-based instruments used to acquire information concerning the *space physics conditions*.

3.1.1 Meridian Scanning Photometer (MSP) in Ny-Ålesund

The MSP instrument is a five-channel photometer that measures the intensity of light from 0° to 180° along the geomagnetic meridian plane. The sky is scanned by a rotating mirror, which delivers the intensity through the five channels, where each channel corresponds to a narrow bandpass filter. The filters are mounted in front of a cooled photomultiplier. The MSP has a time resolution of 16 s. The figures obtained from MSP data and used in this thesis were made by Lorentzen et al. (2010), who used the following emission wavelengths: 427.8 nm (N_2^+), 557.7 nm (O I), and 630 nm (O I).

3.1.2 All-sky imager (ASI)

The all-sky imager is a camera composed of a fish-eye lens, used to inspect the intensity, the temporal evolution and the two-dimensional appearance of auroral optical emissions. The camera has a wide field of view (180°) and can produce circular images centered on zenith, showing the emission intensities at different wavelengths. In this study, the ASI images used were obtained by Lorentzen et al. (2010), who focused on the red-line emissions at 630 nm. A complete description of the ASI instruments can be found in Rinne (2006).

3.1.3 Radars

Radar stands for **Ra**dio **d**etection **a**nd **r**anging. In general, a radar transmits a pulse or a phase-coded radio wave towards a target volume and receives a backscattered echo. The physical properties of the target volume can be determined using the spectral properties of the

backscattered signal. Radars can emit in different frequency ranges and the most common for studying the ionosphere are HF (high frequency, $3-30$ MHz), VHF (very high frequency, $50-330$ MHz) and UHF (ultra-high frequency, $300-1000$ MHz). In this thesis, the measurements made by the European Incoherent Scatter (EISCAT) Svalbard Radar (ESR) and the Super Dual Auroral Radar Network (SuperDARN) were used to obtain some insights in the mechanisms occurring in the F-region ionosphere before and during the rocket flight. They are thus both briefly presented. For a more complete description, see Barth (2009).

European Incoherent Scatter (EISCAT) Svalbard Radar (ESR)

EISCAT is an international research organization supported by China, Finland, Germany, Japan, Norway, Sweden, and the United Kingdom. There are ten incoherent scatter radars in the world, and EISCAT operates three of them in northern Scandinavia. Incoherent scatter radars send electromagnetic wave pulses into the ionosphere. The energy contained into the waves pulses is transmitted via Thomson scattering to the electrons, which start oscillating. Consequently, these excited electrons emit electromagnetic energy in all directions, from which a small percentage is emitted back towards the radar. The radar can then measure a weak *backscattered signal* for different travel-times of the wave pulses and find the Doppler power spectrum. The ion lines are generally offset of a few kHz from the emitted frequency whereas the electron lines (or plasma lines) can be offset of several MHz (Rinne, 2006). From this power spectrum, one can obtain the electron density N_e, the ion velocity v_i and the ion and electron temperatures T_e and T_i, as shown in Figure 3.1 displaying a typical spectrum. From the displacement between the *transmitted frequency* and the center of the double-hump, one can calculate the line-of sight of the Doppler shift of the bulk plasma. The electron density is given by the integral of the power spectrum, the height between the bumps and the center gives T_e/T_i and T_i can be calculated by measuring the width of the spectrum, which depends on the ratio T_i/m_i.

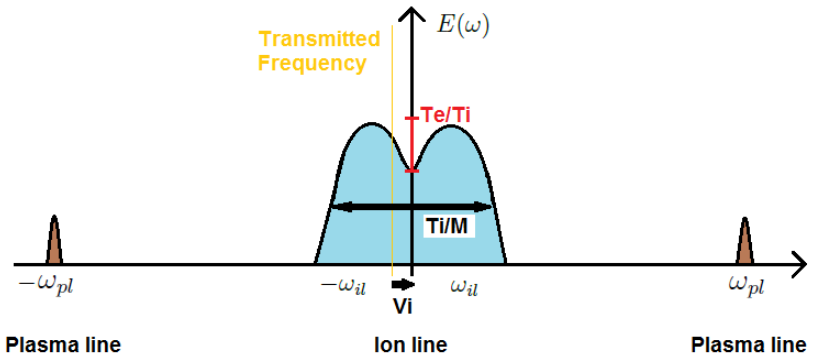

Figure 3.1: Illustrations of the Doppler power spectrum containing the two plasma lines and the double-humps ion-line. The electron density (N_e) can be calculated by measuring the area under the curve, the width of the power spectrum gives the ratio T_i/m_i and T_e/T_i is given by the height of the humps with respect to the height at the center of the spectrum. The line-of-sight bulk velocity corresponds to the displacement between the center of the spectrum and the transmitted frequency. After Rinne (2006).

The EISCAT Svalbard Radar is an UHF system composed of two monostatic antennas located in Longyearbyen, Svalbard. A monostatic radar implies that the antenna both emits and receives the signal. The ESR has one antenna which is a steerable 32 m parabolic dish and one which is fixed along the magnetic field.

Super Dual Auroral Radar Network (SuperDARN)

SuperDARN is a network of 32 HF and VHF coherent backscatter radars looking into the polar regions of the Earth. They were originally designed for measuring and studying plasma convection in the ionosphere but they are also capable of sensing backscatter from ionospheric irregularities in the E and F-region (Chisham et al., 2007). An extensive description of the SuperDARN network can be found in Greenwald et al. (1995) and Chisham et al. (2007)[1]. Figure 3.2 shows the locations of the different radars in 2007 in the northern (panel a)) and southern hemispheres (panel b)), respectively.

Coherent backscatter radars are sensitive to Bragg scattering from small-scales irregularities in the electrons density. These irregularities are typically decameter scale-size structures and are aligned with the magnetic field, meaning that their wavevector is nearly perpendicular to $\mathbf{B}$. In order to be refracted, the waves emitted by the radars must have a component in the same direction as the wavenumbers of the irregularities (principle of constructive interferences).

SuperDARN radars are usually based on the design of the Goose Bay HF radar (Greenwald et al., 1995) and utilize an array of antennas that can be phase steered in 16 beam directions stepping in azimuth. The resolution for a complete scan of the field of view is usually 1 or 2 minutes. The information concerning the elevation of the backscatter echo are provided by a secondary system of 4 antennas. Hence, by emitting sequences of pulses from different locations, Doppler characteristics of the volume targets can be determined and information about the convection flows can be obtained. Providing enough scattering, one can for example, obtain the large scale convection pattern described in section 2.3.2.

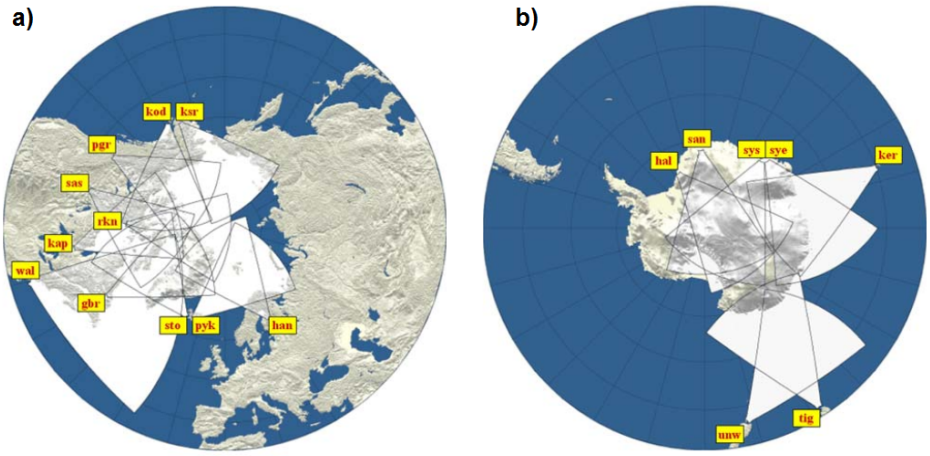

Figure 3.2: Locations of the SuperDARN radars in the a) northern hemisphere and b) southern hemisphere. The abbreviations of the different places can be found in Chisham et al. (2007). Figure from Chisham et al. (2007).

[1]Real-time data can also be obtained at http://superdarn.jhuapl.edu/.

3.2 The Investigation of Cusp Irregularities 2 rocket (ICI-2)

Electron density irregularities are a common feature in the high latitude F-region ionosphere (see section 2.3.3). However, the resolution of the ground based instruments described above is too poor to investigate in depth these small-scales irregularities. Indeed, Moen et al. (2002) pointed out an ultimate need for high-resolution in-situ measurements in order to be able to characterize these structures and assess the role of different instability mechanisms.

Consequently, a series of sounding rockets has been designed by the University of Oslo in order to study irregularities and turbulence in the ionosphere at high latitudes. In this study, the electron density data obtained from measurements made on the ICI-2 sounding rocket is analyzed. This rocket was mainly designed to resolve density gradients/structures down to meter scales and to investigate the role of the gradient-drift instability. Thus, the payload hosts a suite of instruments specially designed to explore plasma structuring in a range involving both kilometer and meter scales, and it was launched when the radars described in section 3.1.3 identified backscatter targets associated with decameter-scale irregularities. The following section presents the main characteristics and instruments on the ICI-2 rocket with emphasis on the multi-Needle Langmuir probes (m-NLP), which were collecting the electron density data.

The ICI-2 sounding rocket was launched from Ny-Ålesund, Svalbard, Norway (78.9° N, 11.9° E, geographic coordinates; 76.4° N, 110.2° E Corrected Geomagnetic Coordinates (CGM) coordinates) at 1035 Universal Time (UT) on the 5th of December 2008. The rocket measurements were made between $73.7 - 76.0°$ Magnetic Latitude (MLAT) and $13.0 - 13.6°$ Magnetic Local Time (MLT) (Oksavik et al., 2012). Ny-Ålesund is located below the cusp region and the inclination angle of the Earth's magnetic field was 82.1° on the day of the launch. The rocket could thus be launched almost along the magnetic field line and directly study plasma structures in the cusp. It was indeed launched with an angle of 21° with respect to the magnetic field and reached its apogee after $t_{of} = 302$ s of flight at an altitude $h = 328.7$ km. The rocket was located in the F-region ionosphere during approximately 400 s.

The total rocket measured 9278 mm and comprised a payload (see Figure 3.3 for a illustration) mounted on a two Stages Motor and hosted the following instruments:

- An **AC/DC Electric field** and wave experiment. The AC and DC electric field are measured in two frequency ranges. In this thesis, the DC electric field data have been considered. Their sampling frequency was $Fs = 180$ Hz.

- Two types of **Langmuir probes** for electron density measurements; a fixed bias Langmuir probe mounted in the front of the rocket and four cylindrical fixed bias Langmuir probes mounted on the E-field booms, symmetrically around the spin axis of the rocket. The latter instruments provided the electron density data analyzed in this thesis with a sampling frequency $Fs = 5787$ Hz. An extended description of this instrument will be given later.

- A **low-energy electron spectrometer** (LEP) for an energy range between 10 eV and 10 keV and a time resolution of 16 ms. This instrument was used to measure the electron precipitation during the flight. The data available from the LEP device start at $t_{of} \approx 200$ s, corresponding to an altitude $h \approx 283$ km.

- A **solid-state spectrometer** for ions and electrons measuring energies above 20 keV.

- An altitude determination system and sun sensors.

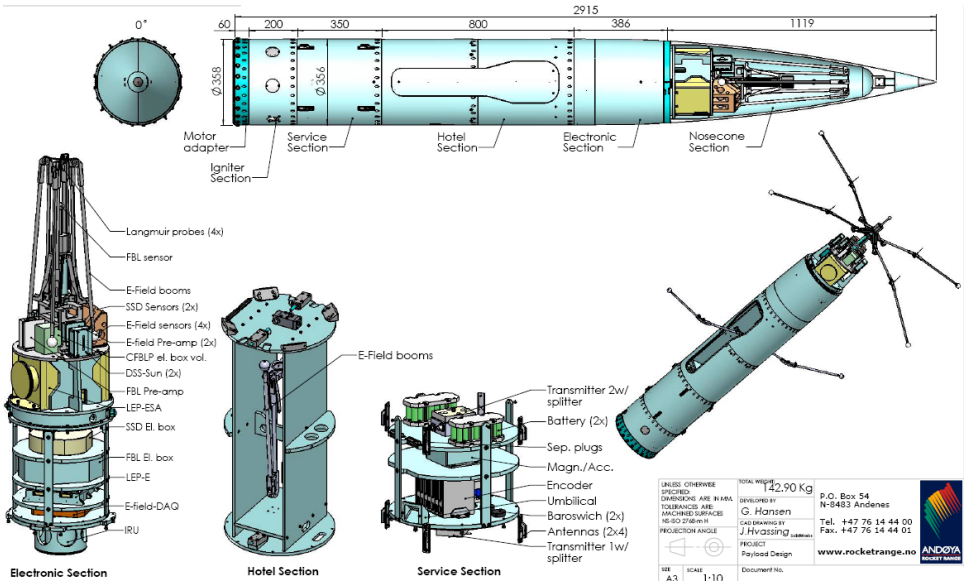

Figure 3.3: Illustration of the different components of the ICI-2 sounding rocket payload. The instruments of interest in this work are the 4-needle Langmuir probes, located on the booms in the front. Courtesy of Jøran I. Moen, Oslo, 2013.

3.2.1 Langmuir probes

The electron density data was calculated from the measurements made by Langmuir probes. Consequently, this section is dedicated to the description of the probe mechanism and design.

A Langmuir probe is a device made to measure characteristic plasma parameters, such as the plasma potential, density, or temperature. The probe consists of a metal wire with a small exposed tip which is biased at a certain potential with respect to the plasma potential. Thus charged particles are either attracted or repelled by the probe and a current is measured. When the probe potential has a large positive bias with respect to the plasma potential, the electrons are attracted by the probe and form a sheath around it. This sheath extends out to a distance of about the Debye length λ_{Def} (see section 2.1.1). Beyond the sheath's limit, the electrons and ions do not feel the presence of the probe and the current is determined by the electron thermal velocity. This current, which is almost potential independent, is called the electron saturation current. If the probe potential is equal to or slightly negative with respect to the plasma potential, only the electrons with a high enough thermal velocity are able to pass the barrier of potential of the probe and contribute to the current. The potential at which the current vanishes is called the floating potential (V_f), meaning that the ion and electron current contributions cancel each other. Note that rockets and other spacecrafts are expected to be at the floating potential with respect to surrounding plasma (Pécseli, 2012). For low enough probe potentials, only the ions are attracted and form a sheath around the probe. The current thereby obtained is the ion saturation current. The typical Current-voltage characteristic of a Langmuir probe is given in Figure 3.4.

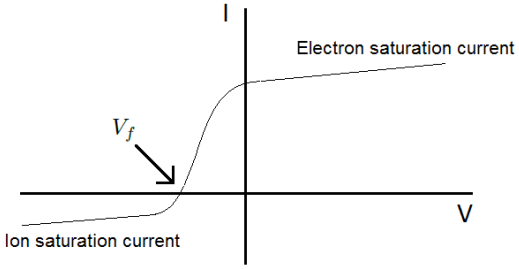

Figure 3.4: Typical voltage-current characteristics. When the probe potential is positive with respect to the plasma potential (here set to $\phi = 0$), electrons form a negative sheath around the probe. Beyond the sheath's limit, the current is limited to the random thermal motion of the electrons. This is the electron saturation current. When the probe potential is below the plasma potential, only the electrons with large enough thermal velocity are collected. The potential at which the current vanishes is defined as the *floating potential* V_f. When the probe potential is sufficiently negative with respect to the plasma potential, a positive sheath is formed around the probe and the collected current is given by the ion saturation current.

The m-NLP probes

The multi-needle Langmuir probe (m-NLP) system, developed at the University of Oslo (Bekkeng et al., 2010) allows measuring the electron current without any information about the plasma potential or the electron temperature. It consists of multiple cylindrical Langmuir probes with a diameter of 0.51 mm and a length of 25 mm, each operating at a different bias voltages. The size of the probes is such that the diameter is much smaller than the electron Debye length expected in the F-region of the ionosphere (7.7 mm $< \lambda_D <$ 8.9 mm) and thus avoid complex sheath effects (Bekkeng et al., 2010). To measure the electron current, the probes are positively biased with respect to the spacecraft potential. Assuming a Maxwellian plasma (the velocity distribution does not change the result, see Jacobsen et al. (2010)), the equation giving the squared of the electron current is

$$I_c^2 = \frac{k_B T_e}{2\pi m_e}(n_e q 2\pi r l)^2 \frac{4}{\pi}(1 + \frac{qV}{k_B T_e}), \tag{3.1}$$

where V is the probe potential, r the probe radius and l the probe length. By separating the temperature and density parts of Eq. (3.1) and subtracting it from one probe to another, we get

$$\Delta(I_c^2) = I_{c2}^2 - I_{c1}^2 = \frac{2q}{m_e}(n_e q 2rl)^2 \Delta V. \tag{3.2}$$

The use of two probes gives a current-voltage characteristic independent of the spacecraft potential. Indeed, as shown in Figure 3.5, it is only the difference between *Probe 2 potential* and *Probe 1 potential* that matters. Note however, that to assess the linearity assumption of the I^2-V slope, more than two probes are needed. Two points are insufficient to distinguish between a line or a curve.

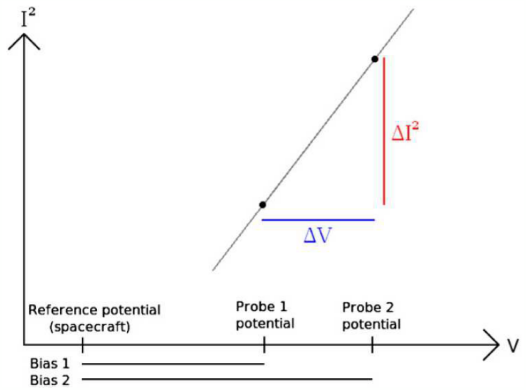

Figure 3.5: Illustration of the m-NLP concept. The square of the current I is proportional to the potentials of the probes V. The slope of the linear curve is given by $\Delta I^2/\Delta V$. Courtesy of *Tore André Bekkeng, Mai 2013, Oslo.*

From Eq. (3.2), it is possible to obtain the electron density n_e

$$n_e = \sqrt{\frac{m_e}{2q(2qrl)^2}\frac{\Delta(I_c)^2}{\Delta V}} \tag{3.3}$$

which is independent of the temperature and the plasma potential (spacecraft potential).

On ICI-2, four cylindrical probes were placed in the front of the payload, on the E-field booms, symmetrically around the spin axis. They were biased at 2.5, 4, 5.5, and 10 V . The sampling rate of the system was 5787 Hz, implying a measurement of the absolute electron density every $1.7280 \cdot 10^{-04}$ s. The electron density samples can then be arranged as a time series, with each data corresponding to a time of flight t_{of} or an altitude of the rocket h (more about time series in given in the following section).

3.3 Time series analysis

The electron density data measured by the 4-NLP described in section 3.2.1 corresponds to a series of measurements obtained at different times and can be considered as a *time series*. Hence, this section begins with a general description of time series and a brief reminder of different statistical tools needed for the study of data records. Then, a procedure referred as *spectral analysis* using windowed *Fourier transforms* is presented in details. This method allows to compute *power spectra* of a series, giving a measure of its variability. The windowed Fourier transforms were chosen as a main technique to study the data obtained from the ICI-2 rocket because they are well established. In addition, several power spectra of plasma density fluctuations measured during previous rocket or satellite campaigns were derived with this method (e.g. Hysell et al., 1994; Jahn and LaBelle, 1998a; Earle and Kelley, 1993; Rodrigues et al., 2009). Furthermore, Fourier transforms are very powerful tools to study spectral characteristics of time series. However, a small downside of Fourier analysis is that it requires the assumption of *stationarity* (see section 3.3.2) (Glover et al., 2011).

Another method called *wavelet analysis* was performed on the data in order to see whether

the results would be different using an alternative method. Wavelet transforms can be used to study non-stationary time series (e.g. Emery and Thomson, 2004; Torrence and Compo, 1998) and can be thought as a generalized form of Fourier transforms (Farge, 1992; Lau and Weng, 1995). Indeed, wavelet analysis' ability to decompose a time series into both time and frequency space provides the possibility to determine both the dominant modes and how they vary in time.

3.3.1 Time series and statistical tools

A statistical time series is loosely defined as a continuous function x of time t, or as a discrete time ordered sequence of observations $\{x_t\}$, exhibiting random or fluctuating properties (Jenkins and Watts, 1968). This means that the exact future behavior of a time series is unpredictable. Statistical and probabilistic laws are thus necessary to analyze a series. In a set of data $x(t)$, each observed value x_1 can be regarded as a realization of a function $X(t)$ at time t_1 called a random variable (rv) and the probability of obtaining this value. This probability is given by a probability distribution function (pdf) $f_{X(t)}(x_1)$. Hence, a whole time series can be described as one realization of an ensemble of random variables $\{X(t)\}$ and their associated probability distribution functions. This set is referred to as a *stochastic process* (Wei, 2006).

Since time series are directly related to statistics, it is relevant to recall here a few basic statistical tools that will be used later in this section. The following list is based on Glover et al. (2011) and Jenkins and Watts (1968)

- **The mean**: the mean μ, or *expected value*, of the probability distribution function associated with the random variable X equals the value X will take on average. The mean corresponds to the first moment of the pdf. For the continuous case, it is given by

$$\mu = E[X] = \int_{-\infty}^{\infty} x f_X(x) dx \tag{3.4}$$

  and gives information about the center of gravity of the distribution. For a group of measurements x_t of length N, the *sample mean* $\bar{x}$ is defined by

$$\bar{x} = \frac{1}{N} \sum_{t=1}^{N} x_t. \tag{3.5}$$

  By letting N go to $+\infty$, the sample mean $\bar{x}$ is equal to the expected value of the pdf, i.e.,

$$\mu = \lim_{N \to \infty} \left(\frac{1}{N} \sum_{t=1}^{N} x_t \right). \tag{3.6}$$

- **The variance**: the variance σ^2 which is the second moment of the pdf reflects how the distribution is spread out around the mean μ. Mathematically, the variance is

$$\sigma^2 = Var[X] = E\left[(X-\mu)^2\right] = \int_{-\infty}^{\infty} (x-\mu)^2 f_X(x) dx. \tag{3.7}$$

For a dataset of length N, the *sample variance* s^2 is given by

$$s^2 = \frac{1}{N-1}\sum_{t=1}^{N}(x_t - \bar{x})^2. \tag{3.8}$$

The square root of the variance is called the standard deviation and is written as σ or s for the continuous and discrete case, respectively. The higher moments of the distribution are called the skewness and kurtosis, and they describe how far a the distribution is from being symmetrical and how *pointy* the distribution is.

- **The covariance**: The covariance is a measure the dependency between random variables. For two rv's X_1 and X_2, it is defined (this definition can be generalized for N variables) as

$$Cov\left[(X_1, X_2)\right] = E\left[(X_1 - \mu_1)(X_2 - \mu_2)\right]. \tag{3.9}$$

If X_1 and X_2 are independent, the covariance becomes $E\left[(X_1 - \mu_1)\right] E\left[(X_2 - \mu_2)\right] = 0$. Note also that $Cov\left[(X, X)\right] = Var\left[X\right]$.

- **The autocovariance function**: The autocovariance function (acvf) of a pdf describes the linear dependency between two values of a time series obtained at different times t_1 and t_2.

$$\gamma_{XX}(t_1, t_2) = E\left[(X(t_1) - \mu(t_1))(X(t_2) - \mu(t_2))\right]. \tag{3.10}$$

The properties of the autocovariance functions for a time series are identical to the ones of the covariance. Note also that $\gamma_{XX}(t_1, t_1) = \sigma^2(t_1)$. The acvf gives information about the correlation between different events in a time series.

3.3.2 Fourier analysis

Fourier analysis techniques are widely used in applied mathematics. They are particularly useful to approximate periodic and non-periodic functions, which can play an important role in mapping data and reliably separate periodic oscillations from random fluctuations. Fourier transforms can therefore be thought as very powerful tools to analyze stationary time series. In the following sections, some of the most important features of Fourier analysis are presented. First, the stationarity assumption and a process called detrending are explained. Then, a more extended description of the discrete Fourier transform (DFT) is given, followed by the introduction of the concept of power spectrum. Note that these two latter parts are principally following the derivations of Jenkins and Watts (1968) and Emery and Thomson (2004). In the end, the *Matlab* routine used in this thesis as well as the windowing process are presented.

Stationarity and autocovariance

Even though properties of a stochastic process are often time dependent, the assumption of *stationarity* has to be made to obtain a statistically valid spectrum using the Fourier transform method (e.g Emery and Thomson, 2004). By assuming stationarity, the series is considered to be in a type of statistical equilibrium or steady state, implying some of its statistical properties to be time independent. The minimum condition for assuming stationarity, called *weak stationarity*

is that the pdf $f_{X(t)}(x(t))$ is time independent. This is equivalent to say that the mean μ and the variance σ^2 stated in section 3.3.1 are constants. Concretely, this means a sub-sequence of the time series looks similar to another sub-sequence. To assume that a process is *strictly stationary*, the multivariate pdf for any set of time $t_1, t_2, ..., t_n$, corresponding to the joint probability distribution function of the rv's associated with the times $t_1, t_2, ...t_n$, must be identical to the pdf of another time set obtained by a translation relative to the initial set $t_1, t_2, ..., t_n$. In particular, stationarity implies that the autocovariance function, giving the dependence between two neighboring points t_1 and t_2, can be expressed as a function of the time difference $\tau = t_2 - t_1$ only

$$\gamma_{XX}(\tau) = E\left[(X(t) - \mu)(X(t+\tau) - \mu)\right] = Cov\left[(X(t), X(t+\tau))\right], \tag{3.11}$$

where the value τ is called *lag*. As stated earlier, the autocovariance is a statistical measure of the dependence between two measurements. If two neighboring values are dependent, they are said to be *correlated*. In practice, the autocovariance $\gamma_{XX}(\tau)$ can be estimated by (Jenkins and Watts, 1968)

$$c_{xx}(\tau) = \frac{1}{N} \sum_{t=1}^{N-\tau} (x_t - \bar{x})\,(x_{t+\tau} - \bar{x}), \tag{3.12}$$

where $\bar{x}$ is the mean described in section 3.3.1.

By plotting the autocovariance function with respect to the lag, one can obtain a measure of the decorrelation time, corresponding to the time interval during which data points are dependent of one another. The decorrelation time is given by the first *zero crossing* of the autocovariance function (see Glover et al. (2011) for examples).

Detrending

In practice, time series are not often in a steady state. They can reveal undesirable features such as *trends* or reflect different types of stationarity: some processes can be regarded as in equilibrium during long time intervals while others are stationary only for shorter time lapses or just locally. These features must be taken into account and trends must be removed from the data in order to perform a Fourier analysis (due to the stationarity assumption, see section 3.3.2).

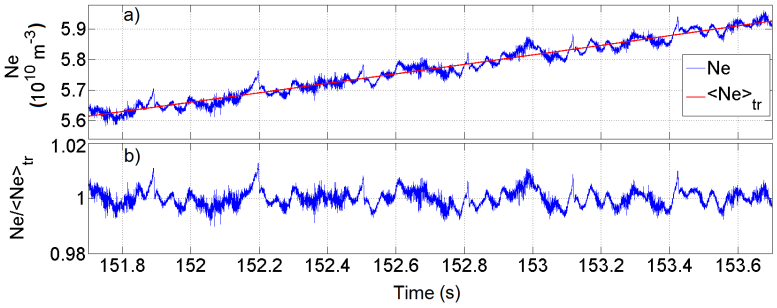

Figure 3.6: a) Electron density showing a trend and the corresponding average electron density $\langle N_e \rangle_{tr}$ given by the smooth spline function s. b) Electron density detrended by dividing the spline function s to the actual data.

In a time series, trends are gradual changes of a statistical property, such as the mean or the variance. They can often be eliminated by a process called *detrending*, leaving a residual series satisfying the stationarity assumption. Detrending is thus a mathematical operation removing a trend from a series. For example, an obvious trend can be observed in Figure 3.6 a), showing two seconds of data from the ICI-2 sounding rocket. The electron density clearly increases over time and, consequently, its mean too.

Several methods of detrending exist. One can for example fit a straight line to a time series exhibiting a linear trend and subtract it from the data, obtaining a new detrended series. The method selected in this thesis is called the *cubic smoothing spline*. This technique consists of measuring the trend in the data by fitting piecewise polynomials of time t to different parts of the time series and to remove it by either subtraction or division. More precisely, cubic smoothing spline give a smooth version s of a time series x_t by fitting a cubic polynomial ($\propto t^3$) every three data points and by keeping the first and second derivative continuous at each point. The technique requires the specification of a *spline parameter* $p \in [0, 1]$, determining how close the fitted curve is to the data. The selection of p allows choosing between a least-square fit ($p = 0$), a curve passing through all points ($p = 1$), or a mix between the two ($0 \leq p \leq 1$). It is this possibility of adjusting the fit that determined the choice of the smoothing spline function as a detrending process in this thesis. Note also that this method is directly given by a Matlab function called `csaps`.

When the spline function has been computed, the trend in the time series can be removed by subtracting or dividing x_t by s. An example of trend removal is given in Figure 3.6 a) and b), showing two second of electron density and the corresponding detrended time series. The curve shown in Figure 3.6 b) has been obtained by dividing the initial time series by the spline function $< Ne >_{trend}$. This *division* method has the advantage of giving a dimensionless data set.

It is obvious that removing a trend from data results in a loss of the large-scale patterns of the time series. Hence, one needs to be careful when analysis the frequency components of a time series and keep in mind that the low frequency structures (corresponding to large scales, long wavelengths structures) are damped or removed. In this thesis, spectral analysis was performed on the data and therefore, this facet of the detrending process was important. It was taken care of by simply not considering the low frequency components of the signal.

The Discrete Fourier Transform (DFT)

In theory, it is possible to represent any arbitrary function as a combination of basis functions, provided a basis spanning the whole function space. The *cosine* and *sine* series can provide such a basis and, Fourier's approach was to use a linear summation of them to reproduce a finite length time series. Let $x(t)$ being a finite-amplitude, continuous and periodic function over a range $[0, T]$, it can be represented as the *Fourier series* of the form (e.g. Emery and Thomson, 2004)

$$x(t) = \sum_{p=0}^{\infty} [A_p \cos(\omega_p t) + B_p \sin(\omega_p t)] \tag{3.13}$$

where A_p and B_p are constants. The angular frequencies ω_p, $p = 1, 2, ..$ are called harmonics and are multiples of the *fundamental frequency* $\omega_1 = 2\pi f_1 = 2\pi/T$. The fundamental frequency corresponds to a period equal to the length of the series.

In data analysis, the sampled values can be thought as being derived from a continuous signal $x(t)$ over a certain time interval $[0, T]$. Let x_n be the data spaced by Δt. Supposing that $N = 2m$ (for simplicity), this corresponds to having $N = T/\Delta t$ sampled intervals where

$$x(t_n) = x(n\Delta t) \equiv x_n \quad n = -m, ..., 0, 1, ..., m-1. \tag{3.14}$$

Using Fourier's idea, it is then possible to build an approximation $\tilde{x}(t)$ of the initial signal such that the discrete and continuous values coincide at the times $t = n\Delta t$. This approximation can be represented, for example, by (Jenkins and Watts, 1968)

$$\tilde{x}(t) = A_0 + \sum_{p=1}^{m-1} [A_p \cos(\omega_p t) + B_p \sin(\omega_p t)] + A_m \cos(\omega_p t). \tag{3.15}$$

By substituting $t_n = n\Delta t$ and $\omega_p = 2\pi p/T = 2\pi p f_1$ in Eq. 3.15, one can obtain a set of N equations with N unknowns given by

$$x_n = A_0 + 2\sum_{p=1}^{m-1} [A_p \cos(2\pi p f_1 n\Delta t) + B_p \sin(2\pi p f_1 n\Delta t)] + A_m \cos(2\pi m f_1 n\Delta t), \tag{3.16}$$

where $\tilde{x}(t_n)$ has been written x_n for simplicity of notation and A_0 is the mean of x_n

The function x_n is thus the sum of sine and cosine whose frequencies are multiple of the fundamental frequency f_1. The highest frequency component that can be resolved is the $N/2$ harmonic and is called the *Nyquist* frequency. Mathematically, it is expressed as

$$f_N = \frac{N/2}{N\Delta t} = \frac{1}{2\Delta t}. \tag{3.17}$$

From solving the system of equations given by Eq. 3.16, one can determine the coefficients A_p and B_p, which provide a measure of the relative importance of each frequency component. Note that it is only possible to determine a maximum of $N/2$ different coefficients (Emery and Thomson, 2004). Indeed, for $0 > p > -N/2$, the trigonometric functions cause a repetition of the same coefficients obtained for $0 \leq p \leq N/2$. Hence, for N even and $p = 0, 1, ...m$, A_p and B_p are given by (Jenkins and Watts, 1968)

$$A_p = \frac{1}{N}\sum_{n=-m}^{m-1} x_n \cos(\frac{2\pi pn}{N}) \tag{3.18}$$

$$B_p = \frac{1}{N}\sum_{n=-m}^{m-1} x_n \sin(\frac{2\pi pn}{N}). \tag{3.19}$$

Note that similar expressions can be obtained for an odd number N.

When dealing with such sums of *sine* and *cosine*, it can be easier to consider the *complex Fourier series*. The coefficients can be rewritten as

$$X_p = R_p e^{i\Phi_p} = A_p - iB_p \quad \text{with} \quad i^2 = -1, \tag{3.20}$$

where $R_p = \sqrt{A_p^2 + B_p^2}$ is the amplitude and $\Phi_p = \tan^{-1}\left(-\frac{B_p}{A_p}\right)$ of the pth harmonic.

From the relation $\cos(2\pi ft) - i\ \sin(2\pi ft) = e^{-i2\pi ft}$, and using Eq. 3.20, Eq. (3.15) can be rewritten as

$$\tilde{x}(t) = \sum_{p=-m}^{m-1} X_p\ e^{i\frac{2\pi pt}{T}}, \tag{3.21}$$

where the amplitudes X_p are

$$X_p = \frac{1}{N} \sum_{n=-m}^{m-1} x_n\ e^{-i\frac{2\pi pn}{N}}, \quad p = -m, ..., 0, 1, ..., m-1. \tag{3.22}$$

Thus, Eq. 3.22 allows one to transpose a discrete sequence of time-domain sampled values $x_n = x(t_n)$ into a discrete frequency-domain sequence. This equation is called the *Discrete Fourier transform* (DFT) and can be rewritten as

$$X(p) = \frac{1}{N} \sum_{n=-m}^{m-1} x(t_n)\ e^{-i\frac{2\pi pn}{N}}. \tag{3.23}$$

For completeness, it is worth noting that this equation is an approximation of the continuous Fourier transforms, which can represent a signal exactly and is given by

$$X(f) = \int_{-\infty}^{\infty} x(t) e^{-i2\pi ft} \mathrm{d}t \tag{3.24}$$

and

$$x(t) = \int_{-\infty}^{\infty} X(f) e^{i2\pi ft} \mathrm{d}f. \tag{3.25}$$

Unfortunately, computing the DFT is very inefficient and the so called radix-2 Fast Fourier Transform (FFT) algorithm is a better alternative. This algorithm produces the same results as the Discrete Fourier Transform, but much faster. The FFT is based on the constraint that the number of points used for the DFT is an integral power of two (N=2^k, where k is in positive integer). This constraint implies that the FFT algorithm requires $N/2 \log_2 N$ operations for a series of length N, while it would need N^2 operations for the normal DFT. For example, when $N = 512$, it would be 200 times shorter to use FFT than DFT (Lyons, 2004). A complete derivation of the FFT algorithm can be found in Lyons (2004), for example.

The spectrum

Once the DFT (or FFT) is applied to the data, a spectrum can be computed to show how the variance of the time series is distributed over the frequencies. The basic idea for computing a spectrum comes from *Parseval's theorem* which states that the mean square or average power of the signal $x(t)$ can be decomposed into contributions from individual harmonics of the fundamental frequency $f_1 = 1/(N\Delta t) = 1/T$. It can be shown that the variance, or average power

is given by (Jenkins and Watts, 1968)

$$s_n^2 = \frac{1}{N}\sum_{n=-m}^{m-1} x_n^2 = \sum_{p=-m}^{m-1} |X_p|^2, \tag{3.26}$$

where X_p is equivalent as in Eq. 3.22. Thus, each $|X_p|^2$ corresponds to the contribution to the average power at frequency f_p or equivalently, it gives a measure of how important each harmonic is in the signal.

For deterministic signals, it can be shown that the *sample power spectrum* S_{xx} can be obtained from the *continuous Fourier spectrum* Γ (Jenkins and Watts, 1968), where

$$\sigma^2 = \int_{-\infty}^{\infty} \Gamma(f)\mathrm{d}f, \tag{3.27}$$

and

$$\Gamma(f) = \lim_{T\to\infty} T|X_p|^2. \tag{3.28}$$

For a discrete series this becomes

$$S_{xx}(f) = \frac{\Delta t}{N}\left|\sum_{n=-m}^{m-1} x_n e^{-i2\pi f n\Delta t}\right|^2, \quad \text{where} \quad -\frac{1}{2\Delta t} \leq f < \frac{1}{\Delta t}. \tag{3.29}$$

For random processes, the sample spectrum S_{xx} has to be thought of a realization of a random variable S_{XX}. However, for a stationary process, a theorem (e.g Priestley, 1981; Bloomfield, 2000) states that the power spectrum $\Gamma(f)$ and the autocovariance function γ_{XX} can be related by

$$\Gamma(f) = \int_{-\infty}^{\infty} \gamma_{XX}(\tau)e^{-i2\pi p f\tau}\mathrm{d}\tau. \tag{3.30}$$

Hence, knowing the autocovariance function or the spectrum provides the same information. The spectrum method is often easier to apply and and more directly related to the physical process behind the time series (Jenkins and Watts, 1968).

The inverse Fourier transform of Eq 3.30 is

$$\gamma_{XX}(\tau) = \int_{-\infty}^{\infty} \Gamma(f)e^{i2\pi p f\tau}\mathrm{d}f, \tag{3.31}$$

and, setting $\tau = 0$, one gets

$$\gamma_{XX}(0) = \sigma^2 = \int_{-\infty}^{\infty} \Gamma(f)\mathrm{d}f. \tag{3.32}$$

This shows that the spectrum $\Gamma(f)$, defined as the Fourier transform of the aurocorrelation function, reflects how the variance of the random variable $X(t)$ is distributed over the frequencies. Remembering that the signal is approximated by a superposition of waves, the value of the spectrum at a given wavelength or frequency is the mean energy in that wave.

In the discrete case, one can thus simply consider the sample power spectrum to be the

Fourier transform of the sample autocorrelation function, i.e

$$S_{XX}(f) = \Delta t \sum_{\tau=-(N-1)}^{(N-1)} c_{XX}(\tau) e^{-i2\pi f \tau \Delta t}, \quad \text{where} \quad -\frac{1}{2\Delta t} \leq f \leq \frac{1}{2\Delta t}. \tag{3.33}$$

The spectrum can be used to study turbulences and/or irregularities. It can indeed be shown that for a stationary process, the acvf function provides the same information (except for a constant factor) as the structure function $S_p(l)$ described in section 2.4.2 (Schultz-Dubois and Rehberg, 1981). Thus, remembering that $S_p(l)$ was the starting point for Kolmogorov's *five-third law* to describe turbulences, the power spectrum, which is given by the Fourier transform of the acvf, see Eq. 3.33), provides similar informations that in the theory of Kolmogorv. One can thus compute the power spectra of a time series to characterize its behavior and see whether it follows a power law.

Windowing

When using the FFT algorithm to study a frequency spectrum, a process called *spectral leakage* can occur. To understand this problem, consider a series of measurements restricted to a finite time interval. The FFT algorithm supposes that the signal is repetitive, and, by repeating the signal, sharp discontinuities are created at the end of each sequence. This results in a spreading of the energy over the different frequencies and is called *spectral leakage* (Glover et al., 2011). However, there is a method called *windowing* that can reduce this undesirable effect. This technique is achieved by convoluting the signal with *window* functions.

Generally, a data set of finite time can be thought as a signal multiplied by a rectangular function of unit amplitude and lasting as long as the signal. This function is referred to a rectangular window. By selecting an appropriate window, one can reduce leakage effects: by multiplying the measured sequence by a function that smoothly approaches zero at both ends it is possible to diminish considerably the discontinuities created by the FFT. There exists several types of windows, each with their advantages and preferred application. The window used in the thesis is the *Hann window* because it has been used for previous spectral density estimations based on rocket measurements (e.g. Jahn and LaBelle, 1998b; Rodrigues et al., 2009; Singh et al., 1985; Earle and Kelley, 1993). Figure 3.7 shows three types of windows that are often used (Emery and Thomson, 2004).

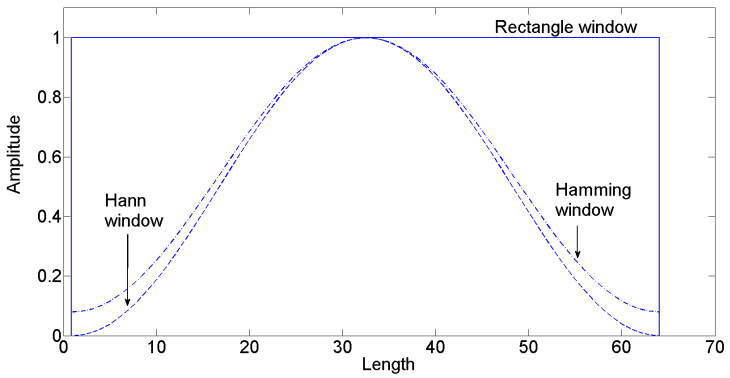

Figure 3.7: Different types of windows commonly used. After Glover et al. (2011).

FFT algorithm

In this section, I present the way the radix-2 FFT algorithm was implemented in this thesis. The corresponding code is given in Appendix 4.7.

1. The time interval of interest is selected and the electron density data is detrended. Let's call the interval *longueur*, which for example can correspond to 1 second of flight, corresponding to approximately 1000 km, and, for the ICI-2 rocket, 5787 data points.

2. The relative density is computed and Hann windowed. The window used had a length corresponding to 1.1× *longueur*. As required by the FFT method, the frequencies are separated into $nfft = 2^n$ bins, where $nfft$ is the smallest power of two that is greater than or equal to the absolute value of *longueur*. In the example cited above, this corresponds to $nfft = 8192$ and all the values between 5789 and 8192 are filled in with zeros. Note that since the data have been detrended and normalized, adding zeros at the end does not change the results of the Fourier transform.

3. The FFT is then applied to the electron density fluctuation (separated into $nfft$ frequency bins) and squared to obtain the power spectrum (corresponding to Eq. (3.29)). Since the FFT procedure gives a symmetric series, only half of it is needed but it must be multiplied by two to obtain the same total power (required by Parseval's theorem).

3.3.3 Wavelet analysis

Conventional data analysis is often done in either the time domain or in the frequency domain. Wavelet transforms can combine the two by their ability to unfold a signal into both space/time and scale/frequency. Indeed, wavelets are functions that are localized in space/time and that can be dilated or contracted in order to obtain a scale/frequency decomposition of a signal. Due to their spatial restriction, wavelets can be used to synthesize time series locally. This is a major difference between the wavelet transforms and the Fourier transforms: the latter are inherently nonlocal. Fourier transforms are based on trigonometric functions that are globally uniform in time and that have an infinite span. The time dependency of a Fourier transformed signal is thus *spread* among the coefficients. Therefore, this technique is not well suited to provide *local* information regarding the time evolution of the spectral characteristics (Farge, 1992). The time-windowed Fourier analysis also presents some handicaps that are overcome by wavelets. For windowed FFT, the data are assumed stationary and the time resolution and the frequency resolution are kept constant. This makes it difficult to study phenomena occurring simultaneously at different scales. Assuming that a time series possesses a wide range of scales, the number of high frequency cycles inside a time window is often larger than the number of low frequency cycles (of which some of them might be *cut* by the window), implying an over-representation of the high-frequency components (Lau and Weng, 1995).

The wavelets have flexible resolution both in space and time. The time-frequency domain (or wavelet domain), is thus spanned by adaptive windows that narrow when sequencing high frequency signals and widens for longer scales (For a comparison between the time-frequency domains associated with the different methods, i.e., FFT, windowed FT and wavelets, see Fig. 1 in Lau and Weng (1995)). In this manner, the wavelets can be thought as *mathematical microscope* (Kumar and Foufoula-Georgiou, 1997): they have the property of *zooming in* and localizing very short lived high frequency structures, while still accurately resolve lower frequency structures.

In this thesis, wavelets have mainly been used as a secondary technique in order to compare the results with the power spectra obtained by the windowed FFT transforms. The principal tools needed to perform wavelet analysis on a time series are presented in this subsection. The description mostly follows the practical guide written by Torrence and Compo (1998). A more theoretical approach can be found in Daubechies (1992) or in Farge (1992).

Definitions

A one dimensional function $\psi(t)$ is admissible as a (mother) wavelet if (Farge, 1992)

$$c_\psi = \int_0^\infty \frac{|\hat{\psi}(\omega)|^2}{|\omega|} \mathrm{d}\omega < +\infty, \tag{3.34}$$

where $\hat{\psi}$ is the Fourier transform of ψ

$$\hat{\psi}(\omega) = \int_{-\infty}^{\infty} \psi(t) e^{-i2\pi\omega t} \mathrm{d}t. \tag{3.35}$$

If $\psi(t)$ is integrable, it implies that its mean is zero, i.e.,

$$\int_{-\infty}^{\infty} \psi(t) \mathrm{d}t = 0 \tag{3.36}$$

The wavelet functions are derived by translating the *mother wavelets* with a factor b and by dilating them by a factor s. The wavelets can thus be written as (Kumar and Foufoula-Georgiou, 1997)

$$\psi_{b,s}(t) = \frac{1}{\sqrt{s}} \psi\left(\frac{t-b}{s}\right). \tag{3.37}$$

The wavelet transform of a real signal $f(t)$ is defined as a convolution integral

$$W(b,s) \equiv \frac{1}{\sqrt{s}} \int_{-\infty}^{\infty} f(t) \psi^*\left(\frac{t-b}{s}\right) \mathrm{d}t, \tag{3.38}$$

where ψ^* is the complex conjugate of ψ. $W(b,s)$ is the wavelet coefficient at time b and scale s. The integral measures the similarities between the shape of the signal and the shape of the wavelets. The signal $f(t)$ can be reconstructed via the inverse wavelet transform (Daubechies, 1992)

$$f(t) = \frac{1}{c_\psi} \int_{-\infty}^{\infty} \frac{\mathrm{d}s}{s^2} \int_{-\infty}^{\infty} \psi\left(\frac{t-b}{s}\right) W(b,s) \mathrm{d}b. \tag{3.39}$$

Choice of wavelet: The Morlet wavelet

Several types of wavelets are commonly used to analyze data. Wavelets can generally be separated into two main categories: continuous or nonorthogonal wavelets and orthogonal wavelets. Orthogonal wavelets (such as the *Haar* or *Daubechies*) are useful for signal processing with minimal bases while continuous transforms (such as the Morlet or Mexican hat) are useful for time series analysis, where the redundancy at large scales are correlated and yields enhanced information on the time-scale localization (e.g Lau and Weng, 1995; Torrence and Compo, 1998).

Several factors should be considered when opting for a wavelet function (see Farge (1992) for more details).

- **Real or Complex**: The real functions are well adapted to isolate peaks or discontinuities. The complex functions are able to return both the amplitude and phase of the wavelet coefficients, which might give information about the oscillating nature of a signal.

- **Width**: The width is directly related to the resolution in the time and frequency domain. The selection of a long-lasting wavelet function allows a good frequency resolution, while a narrow function signifies a poor frequency resolution.

In this study, the Morlet wavelet has been chosen. The principal reasons are the following: it is probably the most used wavelet (Farge, 1992); due to its width, it gives a good compromise between time and frequency resolution; since it is complex, the amplitude and the phase of the coefficients can be computed. Another reason is that it was used in the article by Lagoutte et al. (1992) to study turbulences in the high-latitude ionosphere. The complex Morlet wavelet is a plane wave modulated by a Gaussian. For a non-dimensional time parameter $\eta = t/s$, it is given by (e.g. Kumar and Foufoula-Georgiou, 1997)

$$\psi_0(\eta) = \pi^{-1/4}(e^{-i\omega_0\eta} - e^{-\omega_0^2/2})e^{-\eta^2/2} \tag{3.40}$$

which, if $\omega_0 \geq 5$, satisfies the admissibility condition (Eq. (3.36)) and can be approximated by

$$\psi_0(\eta) = \pi^{-1/4}e^{-i\omega_0\eta}e^{-\eta^2/2}. \tag{3.41}$$

The Fourier transform of Eq. (3.41) is

$$\hat{\psi}_0(s\omega) = \pi^{-1/4}e^{-(s\omega-\omega_0)/2}. \tag{3.42}$$

In Figure 3.8, the Morlet function with $\omega_0 = 6$ is presented both in the time domain (Figure 3.8 a)) and in the frequency domain (Figure 3.8 b)).

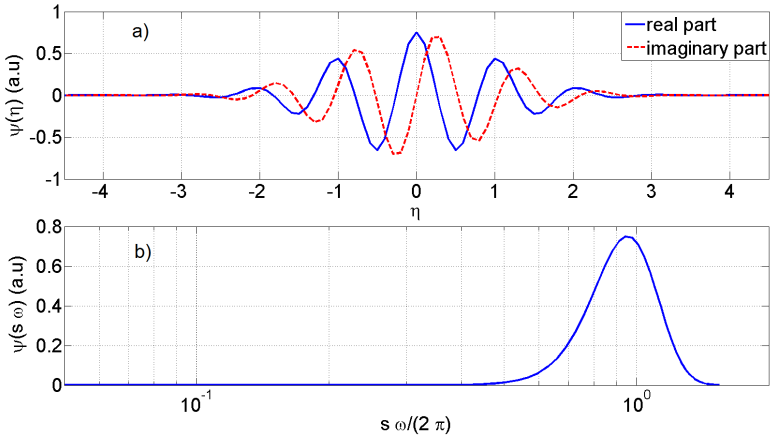

Figure 3.8: a) Real (solid line) and imaginary (dashed line) part of the Morlet wavelet in the time domain. b) Fourier transform of the Morlet wavelet. The scale is $s = 10\Delta t$. Inspired by Torrence and Compo (1998).

Application to time series

The wavelet transforms can be applied to time series. Let x_n being a time series, with time spacing Δt and $n = 0, ..., N-1$. As in Eq. (3.38), the continuous wavelet transform of the discrete sample x_n is defined as the convolution of x_n with the scaled and translated function $\psi_{n,s}$. Thus, by convoluting the signal and the wavelet N times for each scale, a picture revealing both the amplitude of any feature and their time dependency can be drawn. This process can be intuitively understood by looking at Figure 3.9 showing two steps of a wavelet transform.

1. The first wave function is compared to the beginning of the signal, giving a coefficient (high if the wavelet and the signal are much alike). The wavelet is then translated and convoluted with another part of the data series. This translation/convolution process is repeated for the whole signal, giving N coefficients for the first scale. See Figure 3.9. a)

2. The scale of the wavelet changes and is compared to the signal, as in point 1. Step 1 is then reiterated with the new scaled wavelet. 3.9. b)

This procedure is repeated until all the scales have been analyzed.

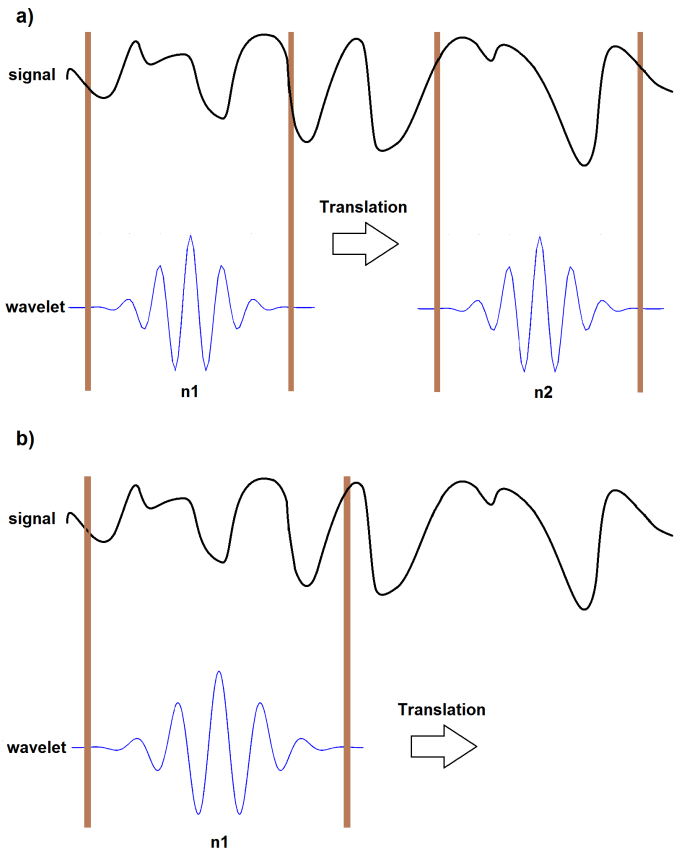

Figure 3.9: a) Step 1: The wavelet of a certain scale is convoluted with the beginning of the signal, resulting in a wavelet coefficient. The same wavelet is then translated and convoluted again. b) Step 2: The same procedure as in step 1 occurs, but with a wavelet of different scale.

A common way to normalize the wavelets is by constraining them to have the same energy at any scale. The wavelets can thus be normalized to have unit energy at each scale s, with ψ_0 defined such that

$$\int_{-\infty}^{\infty} \hat{\psi}_0(\omega')\mathrm{d}\omega' = 1 \tag{3.43}$$

and

$$\hat{\psi}(s\omega_k) = \sqrt{\frac{2\pi s}{\Delta t}}\hat{\psi}_0(s\omega_k). \tag{3.44}$$

The mathematical expression for the normalized wavelet transform is thus

$$W_n(s) = \sum_{n'=0}^{N-1} x_{n'}\psi^*\left(\frac{(n'-n)\Delta t}{s}\right). \tag{3.45}$$

It is also possible to compute this equation in Fourier space, using the Fourier transform of both the time series $\hat{x}_k$ (see Eq. (3.23)) and the wavelet $\hat{\psi}(s\omega)$. The wavelet coefficients can then be obtained by taking the inverse Fourier transform of the product

$$W_n(s) = \sum_{k=0}^{N-1} \hat{x}_k\hat{\psi}^*\left(s\omega_k\right)e^{2\pi i\omega_k n\Delta t}, \tag{3.46}$$

with the angular frequencies being defined as

$$\omega_k = \begin{cases} \dfrac{2\pi k}{N\Delta t}, & k \leq \dfrac{N}{2} \\ -\dfrac{2\pi k}{N\Delta t}, & k > \dfrac{N}{N}. \end{cases} \tag{3.47}$$

When the analyzing wavelet functions ψ are complex, the coefficients $W_n(s)$ are also complex. It follows that the wavelet transforms can be represented by their real part, their imaginary part, their amplitude or their phases. It is also possible to define *the wavelet power spectrum* as (Torrence and Compo, 1998)

$$P_n = |W_n(s)|^2. \tag{3.48}$$

Thus, one can create a wavelet plot (called scalogram or wavelet spectrogram if frequencies are used) with time/distance in the horizontal axis, frequency/scale in the vertical axis, and power in the third axis. For example, Figure 3.10 shows the wavelet spectrogram of the function

$$f(t) = \begin{cases} \sin(2\pi 4t), & t \leq \dfrac{1}{2}s \\ \sin(2\pi 8t), & t > \dfrac{1}{2}s. \end{cases} \tag{3.49}$$

with random noise of random amplitude. The wavelet spectrogram clearly shows two distinct regions with high power at frequencies of about 4 and 8 Hz.

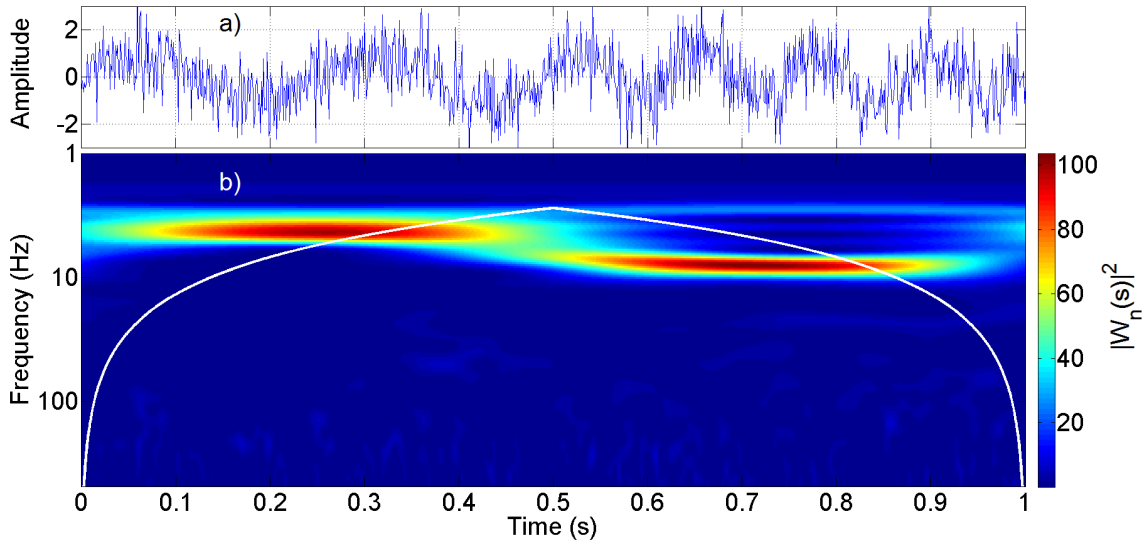

Figure 3.10: a) Sinus function with random noise. The sinus has a frequency of 4 Hz before $t = 0.5$ s and 8 Hz after $t = 0.5$ s. b) The wavelet spectrogram of the function above, showing the enhanced power at the frequencies abovementioned. The white line shows the cone of influence.

Each slice through the y axis is then a measure of the local wavelet spectrum. The *global wavelet spectrum* of a time series is obtained by averaging the power spectrum over the whole time interval, i.e.

$$\bar{W}^2(s) = \frac{1}{N}\sum_{n=0}^{N-1}|W_n(s)|^2. \tag{3.50}$$

The wavelet global spectrum can then be compared to the power spectrum obtained by applying the FFT transform of a time series. It has been analytically proved that for a function f, the Fourier power spectrum $P_F(\omega) = |\hat{f}(\omega)|^2$ and the wavelet global spectrum $P_W(s) = \int |W(b,s)|^2 \mathrm{d}b$ are related by (Hudgins et al., 1993)

$$P_W(s) = \frac{1}{2\pi}\int_{-\infty}^{\infty} P_F(\omega)P_{Ws}(\omega)\mathrm{d}\omega, \tag{3.51}$$

where $P_{Ws}(\omega)$ is the power spectrum of the wavelet at scale s. The wavelet global power spectrum is equivalent to the weighted average Fourier spectrum, with $P_{Ws}(\omega)$ as weights. Note also that a test has been performed to check that the wavelet global power spectrum of a single peak gives a flat spectrum, as it does for the Fourier transforms.

In practice one needs to select a wavelet function and a set of scales s in order to compute Eq. (3.46). In this project, the Morlet wavelet with $\omega_0 = 6$ has been chosen (following Torrence and Compo (1998) and in order to satisfy the admissibility condition, Eq. 3.36), accompanied by scales following a logarithmic progression

$$s_j = s_0 2^{j\delta j}, \qquad j = 0, 1, ..., \delta j^{-1}\log_2\left(N\Delta t/s_0\right), \tag{3.52}$$

where $s_0 = 2\Delta t$ is the smallest resolvable scale and δj is the spacing between the scales in logarithmic units. For the Morlet wavelet, the relation between the scale s and the Fourier wavelength λ is given by (Torrence and Compo, 1998)

$$\lambda = \frac{4\pi}{\omega_0 + \sqrt{2 + \omega_0^2}} s, \tag{3.53}$$

which, for $\omega_0 = 6$, is $\lambda = 1.03s$. Consequently, the frequency is approximately $1/s$.

Time series have a finite length. When Eq. (3.46) is applied to the data it is assumed that the samples are cyclic and errors will arise at both ends of the wavelet power spectrum. This effect can be minimized by padding the data with zeros, i.e. adding 0's at the extremities of the data. Note, however, that the addition of zeros results in a decrease of amplitude of the power spectrum at large scales near the edges. Wavelets are vanishing outside a certain time interval. It is thus possible for each scale to find a region in the wavelet domain (b,s) that can be influenced by a point (b_0, s_0). This region, or e-folding time, is called the *cone of influence* (COI) and is defined by $|b - b_0| = s\Lambda$, where $\Lambda = \sqrt{2}$ for the Morlet wavelet (Lau and Weng, 1995). Hence, one can describe the regions where edge effects are considerable, by finding the COI at the boundaries of the wavelet domain. The e-folding time is chosen such that the power for a discontinuity at one edge drops by a factor of e^{-2} (Torrence and Compo, 1998). An example of COI can be seen in Figure 3.10. The size of the COI at each frequency provides an estimate of the decorrelation time for a single spike in the data. Hence, it is possible to compare the width of enhanced power in the wavelet spectrum with the decorrelation time at the peak frequency in order to distinguish between a spike in the time series and a harmonic component.

3.4 Considerations and assumptions

Fundamental difficulties arise when analyzing data from rockets, balloons, satellites etc. These difficulties can be divided into three categories :

- *Dynamic range in wavenumber space*: in the ionosphere and the magnetosphere, the density fluctuations of fluid turbulences may occur over scales going from a few meters (the ion gyroradius) to several earth radii and no single instrument is capable of covering this entire range.

- *Statistical significance*: it is an issue when studying turbulences by rockets and few have addressed this problem in the literature (Kintner and Seyler, 1985). Homogeneous and isotropic turbulence theories involve spatial averaging over the whole volume while a spacecraft only samples a small part of the medium at specific times.

- *Interpretation of the data and transformation from frequency-space into wavenumber-space*: in fluid turbulence theories, power laws are represented in wavenumber-space space but spacecrafts are sampling in time domain. This raises the issue of distinguishing between temporal and spatial fluctuations. Without any preliminary assumptions about the plasma flow considered, there is no simple way to transform fluctuations measurements from frequency- to wavenumber-space.

In the following part, the last problem cited above is addressed in more details.

3.4.1 Transformation from frequency-space to wavenumber-space

The energy cascades derived from turbulence theory are usually computed in the spatial domain, i.e. plotting power with respect to wavenumbers (see section 2.4.2). However, the data obtained from a spacecraft are acquired at a certain sampling frequency Fs, that is, in the time domain. As described in section 2.4.2, to characterize turbulences by power laws, frequency should be translated to wavenumber. This process is not straightforward since the measurements made by the spacecraft are related to Fs and not to the intrinsic frequencies associated with sampled systems. Hence, to achieve this, it is common to make a critical simplification known as *Taylor's hypothesis* (Taylor, 1938) (also referred as the *frozen in turbulences* assumption) (Kintner and Seyler, 1985): the time series measured by the rocket corresponds to a simple one-dimensional spatial sample. In essence this means that the motion of dynamic waves of the plasma changes over a timescale much longer than the time needed for the spacecraft to pass through the wave fluctuations. The movement of the fluctuations can therefore be neglected and frequency can be converted into wavenumbers.

Data acquired by the spacecraft at times t_i can be considered as a straight line sample in the plasma frame of reference at points $\mathbf{r}_i = \mathbf{r}_0 - \mathbf{v}_{rel}\ (t_i - t_0)$, where $\mathbf{v}_{rel}$ is the velocity of the plasma relative to the rocket. This corresponds to a one dimensional cut through the medium, but it contains information about fluctuations in all directions at the same time. Using the *frozen in turbulences* assumption, the spacing between two measurements made by a rocket with velocity $\mathbf{v}_{rel}$ and sampling frequency f_s is $\lambda = |\mathbf{v}_{rel}|/f_s$. This is equivalent to a Doppler shift and the wavenumber can be related to the sampling frequency by $2\pi f_s = \mathbf{k} \cdot \mathbf{v}_{rel}$. From this relation we get that if the relative velocity is zero, the spacing between two intervals is also zero and the data points are measured in the same region. Oppositely, the higher the relative speed is, the more plasma is being investigated.

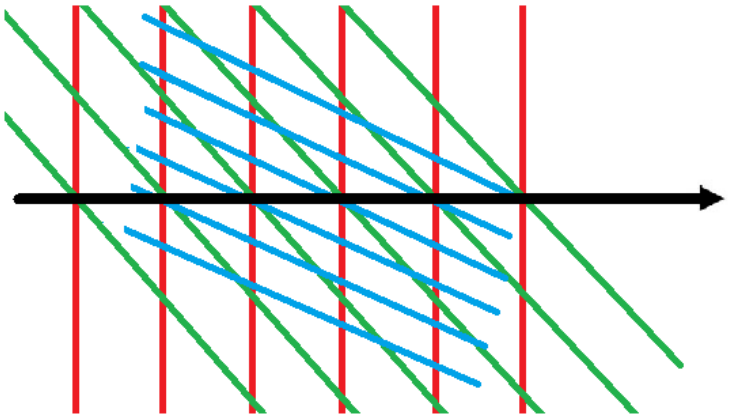

Figure 3.11: Scheme of the waves observed by a rocket. The black arrow is the rocket trajectory and the colored lines correspond to crests of different waves. Every fluctuation with a component of the wavevector of $2\pi f_s/\mathbf{v}_{rel}$ along the rocket path contributes to the power at the spacecraft frequency f_s. From the rocket it seems that all three waves have the same apparent wavelength along the trajectory and it is impossible to distinguish between the different frequencies, even though there orientation and wavelengths are different in the plasma. After Horbury et al. (2011).

The fact that the rocket only samples a *cut* in the plasma has also some influence on the power spectra. If all the fluctuations were parallel to the flow direction, the power spectrum obtained would be the same as the one in the plasma. However, power is expected in several directions in wavevector-space and the spectrum measured by a spacecraft contains the contributions of all the wavevectors with a component along the track. This phenomenon is called *aliasing* (Horbury et al., 2011) and it is represented in Figure 3.11, where the black line is the rocket trajectory. The three waves (red, green and blue) have different orientations and wavelengths but they have the same apparent wavelength along the spacecraft. The problem of aliasing is less important at high frequencies (wavenumbers) because small eddies usually have about the same size in all directions.

The one dimensional power spectrum measured by a spacecraft is called the *reduced spectrum* (Horbury et al., 2011) of the true spectrum $S(\mathbf{k})$ and is given by (Shkarofsky, 1969)

$$C(k_x) = \frac{1}{(2\pi)^3} \iint_{-\infty}^{\infty} S(\mathbf{k}) \mathrm{dk_y dk_z}, \tag{3.54}$$

where the flow is along the **x**-direction (**y** and **z** are in the plane perpendicular to x). Due to the points evoked above, there is in general no way to relate the frequency f_s of a moving spacecraft and the wavevector $\mathbf{k}$ for turbulent phenomena without making some assumptions about the plasma structures. An assumption often made when studying ionospheric irregularities is that the turbulence is purely spatial, i.e. time independent (Fredricks and Coroniti, 1976). It has been shown by Fredricks and Coroniti (1976), that even with the hypothesis of time-independence and isotropy, a sample power spectrum having the shape $C(f_s) \sim f_s^{-2}$ might correspond, in the rest frame of the plasma, to

$$\begin{aligned} &S(k) \sim k^{-2} \quad \text{in one dimension} \\ &S(k) \sim k^{-3} \quad \text{in two dimension} \\ &S(k) \sim k^{-4} \quad \text{in three dimension.} \end{aligned}$$

This shows the ambiguity to determine the spectrum in the rest frame of the plasma.

Assuming time independent and isotropic structuring in the plane perpendicular to **B**, one can obtain a wavenumber spectrum from the frequency spectrum using the relation (e.g. Earle and Kelley, 1993; LaBelle et al., 1986)

$$2\pi f_s = \mathbf{k} \cdot \mathbf{v}_{rel}. \tag{3.55}$$

The power spectrum then becomes

$$C(k) = C(\mathbf{k} \cdot \mathbf{v}_{rel}) \frac{|\mathbf{v}_{rel}|}{2\pi}. \tag{3.56}$$

The relative velocity of the plasma $\mathbf{v}_{rel}$ can been obtained by using the DC electric field measured by the rocket. This is shown in the following lines. The electric field measured by the rocket is given by

$$\mathbf{E}_{rock} = \mathbf{E}_{ind} + \mathbf{E}_e + \mathbf{E}_{cor}, \tag{3.57}$$

where the three terms on the right hand side are: an electric field in the Earth frame of reference

$\mathbf{E}_e$, a small amplitude electric field due to the co-rotation of the atmosphere $\mathbf{E}_{cor}$ and n induced electric field $\mathbf{E}_{ind}$, due to the movement of the rocket in the magnetic field $\mathbf{B}$. Mathematically, the latter is expressed as

$$\mathbf{E}_{ind} = \mathbf{v}_{rock} \times \mathbf{B}. \tag{3.58}$$

The relative velocity of the plasma seen from the rocket can be expressed as

$$\mathbf{v}_{rel} = \mathbf{v}_{plasma} - \mathbf{v}_{rock}, \tag{3.59}$$

where $\mathbf{v}_{plasma}$ is given by the $\mathbf{E} \times \mathbf{B}$-drift in the high latitude ionosphere (see section 2.3.2), i.e.

$$\mathbf{v}_{plasma} = \frac{\mathbf{E}_e \times \mathbf{B}}{\mathbf{B}^2}. \tag{3.60}$$

Considering only the plane perpendicular to $\mathbf{B}$, Eq. (3.58) can be transformed into

$$\frac{\mathbf{E}_{ind} \times \mathbf{B}}{\mathbf{B}^2} = -\mathbf{v}_{rock}. \tag{3.61}$$

Neglecting E_{corr} it is therefore possible to rewrite Eq. (3.59) as

$$\mathbf{v}_{rel} = \frac{\mathbf{E}_e \times \mathbf{B}}{\mathbf{B}^2} + \frac{\mathbf{E}_{ind} \times \mathbf{B}}{\mathbf{B}^2} \approx \frac{\mathbf{E}_{rock} \times \mathbf{B}}{\mathbf{B}^2}. \tag{3.62}$$

Thus, $\mathbf{E}_{rock}$ and $\mathbf{B}$ data enable one to determine the relative velocity of the plasma perpendicular to the magnetic field. The values of $\mathbf{B}$ for computing the velocity were obtained from the IGRF model described in section 2.2.1, which is assumed vertical at the location of the rocket flight. The magnetic field used here was thus $\mathbf{B} \approx -5 \cdot 10^{-5}\,\mathrm{T}$. Figure 3.12 shows the magnitude of $\mathbf{v}_{rel}$ calculated using the electric field measurements from ICI-2. The magnitude was $||v_{rel}|| \approx 1200\,\mathrm{m/s}$ until $t_{of} = 150\,\mathrm{s}$ of flight and was highly fluctuating until about $t_{of} = 230\,\mathrm{s}$. Between $t_{of} = 230\,\mathrm{s}$ and $t_{of} = 350\,\mathrm{s}$, the velocity was $||v_{rel}|| \approx 1200\,\mathrm{m/s}$ and decreased later to $||v_{rel}|| = 1000\,\mathrm{m/s}$. The values shown in Figure 3.12 will be used in the next sections to convert from temporal to spatial structures. For this purpose, the magnitude of the relative velocity has been chosen in order to obtain minimal wavenumbers and maximal wavelengths.

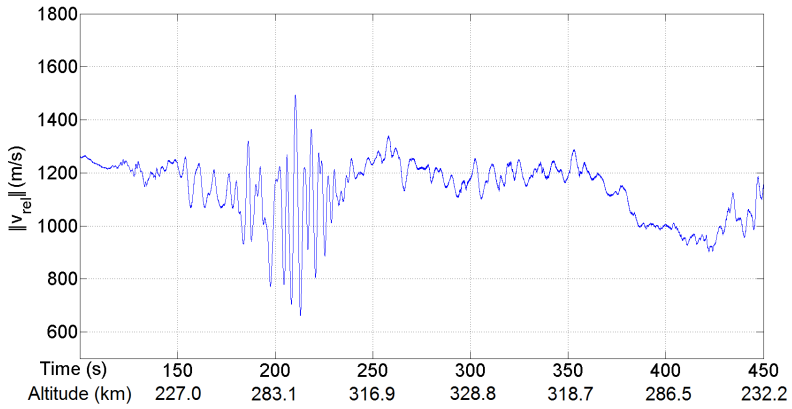

Figure 3.12: Magnitude $||v_{rel}||$ of the relative velocity $\mathbf{v}_{rel} = \frac{\mathbf{E}_{rock} \times \mathbf{B}}{\mathbf{B}^2}$.

4 Observations and Discussion of the Results

In this chapter, the description of the observations made by the ICI-2 rocket and the discussion of the results are presented. The plasma-flow conditions of the rocket flight are given, as well as the electron density structures measured by the rocket. The windowed FFT and the Morlet wavelet power spectra of the electron density are described and analyzed. These results are compared with previous in-situ studies and discussed with respect to several instability mechanisms.

4.1 Flight conditions for ICI-2

As it was shown in paragraph 3.4.1 assumptions about the plasma have to be made to be able to study irregularities or turbulences by means of power spectra. Therefore, it is important to have a good overview of the time history of the auroral activity and the plasma flows in the area where the rocket flew. The article of Lorentzen et al. (2010) gives a detailed overview of the solar wind and auroral conditions of the morning hours of December 5, 2008, i.e., when the ICI-2 sounding rocket was launched. A few important features are nevertheless recalled here.

The ICI-2 rocket was launched from from Ny-Ålesund, Svalbard, at 1035 UT almost along the magnetic field lines (see section 3.2). The solar wind speed was about 390 km/s before launch and increased slightly later. While the IMF B_x was fluctuating around $B_x = 0$ nT, the IMF B_z was steady negative $B_z \approx -6$ nT and the IMF B_y was steady positive about $4 - 5$ nT. Note that the information concerning the solar wind were obtained from the ACE satellite (Lorentzen et al., 2010). Due to the long-lasting negative B_z, magnetic reconnection occurred on the dayside equatorward of the cusp, allowing direct entry of plasma from the solar wind into the cusps, as described in section 2.3.1. The positive B_y and negative B_z imply the dual-cell convection pattern with poleward flow (PMAFs) into the polar cap at high latitude (see section 2.3.2). Thus plasma structures created at lower latitudes can convect through the polar cap into the nightside.

The dayside auroral oval was located south of zenith, at about $140° - 150°$ scan angle from the MSP. Several auroral intensifications followed by poleward moving auroral forms took place during the morning, as expected for IMF $B_z < 0$, see section 2.3.3. The sky conditions can be seen in Figure 4.1, showing ASI data, MSP 6300 Å(corresponding to red emission) and ESR 42 m field aligned data for the time interval $1000 - 1100$ UT. The vertical black line represents the launch time of the ICI-2. On the top right panel (MSP data), two poleward moving auroral forms can be observed at 1002 UT and at 1030 UT. Two plasma enhancement seen as faint traces starting around 90°scan angle 'detach' from the poleward moving auroral forms and move northward. They can be detected more clearly as two double-humped peaks in the second picture on the right, showing the MSP data of intensity versus time at a scan angle of 98°. The 98° coincides with the field of view of the 42 m ESR antenna and is marked with a white line on all panels in the figure. The three next plots on the right are ESR data. We can note that the electron densities and temperatures are high between $h = 150$ and $h = 250$ km altitude, implying low-energetic particle precipitation in the F-region ionosphere. In addition,

no enhancement in the ion temperature is observed, meaning that no local Joule heating due to collisions between the ions and the neutrals is occurring.

The four plots on the left show 6300 Å all-sky Imager data from Longyearbyen at different times (corresponding to the numbers 1, 2 3 and 4) superposed on a geographic reference frame. The rocket path is shown as a dashed black line. At 1022 UT (picture top left) the auroral oval is well south of Svalbard and nine minutes later, its poleward boundary is located close to the south of Svalbard. The emission intensity increases matching the poleward moving auroral form seen in the MSP data at 1031 UT. At launch time (panel 3 left), the oval had retracted leaving a region of enhanced emission compared to the background along the rocket path. The rocket was launched at this precise time because the enhanced emission had started to drift into the polar cap and would be intersected by the spacecraft. The goal of the mission was indeed to investigate the structures of polar cap patches (see section 2.3.3) or poleward moving density enhancements at meter-scales, and the optimal conditions were satisfied (see 3.2). The last plot on the left shows the situation at apogee. The ICI-2 spacecraft flew north of the auroral oval except for the last hundred seconds where it intersected a region with cusp precipitation.

To have a better overview of the plasma encountered by the rocket, Oksavik et al. (2012) used SuperDARN convection data to obtain the plasma history presented in Figure 4.2 (see section 3.1.3 or more information about the SuperDARN). Due to a north-west large-scale convection pattern, the plasma crossing the rocket actually originated at lower latitudes in the dusk sector. This pattern is consistent with stable IMF B_z negative and B_y positive. In Figure 4.2, the black lines represent plasma stream lines that intersected the rocket every $t_{of} = 100\,\mathrm{s}$ and the black dots indicate the time history every 2 minutes. The gray lines correspond to the universal time. By comparing the panels on the left of Figure 4.1 and the convection pattern shown in Figure 4.2, it is possible to have an idea about the plasma structures crossing the spacecraft's trajectory. For example, the transient brightening that happened 1031 UT (see panel 2 left in Figure 4.1), moved towards north-west and crossed the rocket path around $t_{of} = 120\,\mathrm{s}$ after the launch.

This convection pattern calculated from ground based instruments can be verified using the in-situ electric field data. The electric field measured on board provides more precise information due to its higher sampling rate than the ground based instruments. Using the magnetic field data from the International Geomagnetic Reference Field (IGRF) model and assuming that $\mathbf{B}$ is in the z-axis ($\sim$ perpendicular to the ground over Svalbard) it is possible to compute the $\mathbf{v}_{plasma} = \mathbf{E} \times \mathbf{B}/B^2$ velocity. Figure 4.3 a) shows the norm and the components perpendicular to the magnetic field of $\mathbf{v}_{plasma}$ in an Earth-fixed coordinate system North-East-Down (NED), using $\mathbf{B} \approx B_z \hat{\mathbf{z}} \approx -5 \cdot 10^{-5}\,\mathrm{T}$, where $\hat{\mathbf{z}}$ is a unit vector in the $\mathbf{z}$-direction. The velocity does not exhibit much features, except a wave-like pattern between $t_{of} = 170\,\mathrm{s}$ and $t_{of} = 230\,\mathrm{s}$. The flow was directed towards west during the entire flight and pointed slightly northward until $t_{of} = 370\,\mathrm{s}$. The direction of $\mathbf{v}_{plasma}$ can be better appreciated in Figure 4.3 b) showing the velocity vector with respect to the azimuth angle. Note that uncertainties in the method of electric field extraction lead to an underestimate of the values up to 30% in magnitude but no major impact on the direction should be expected (private communication, Dr. Lasse Clausen, Olso, April 2, 2013).

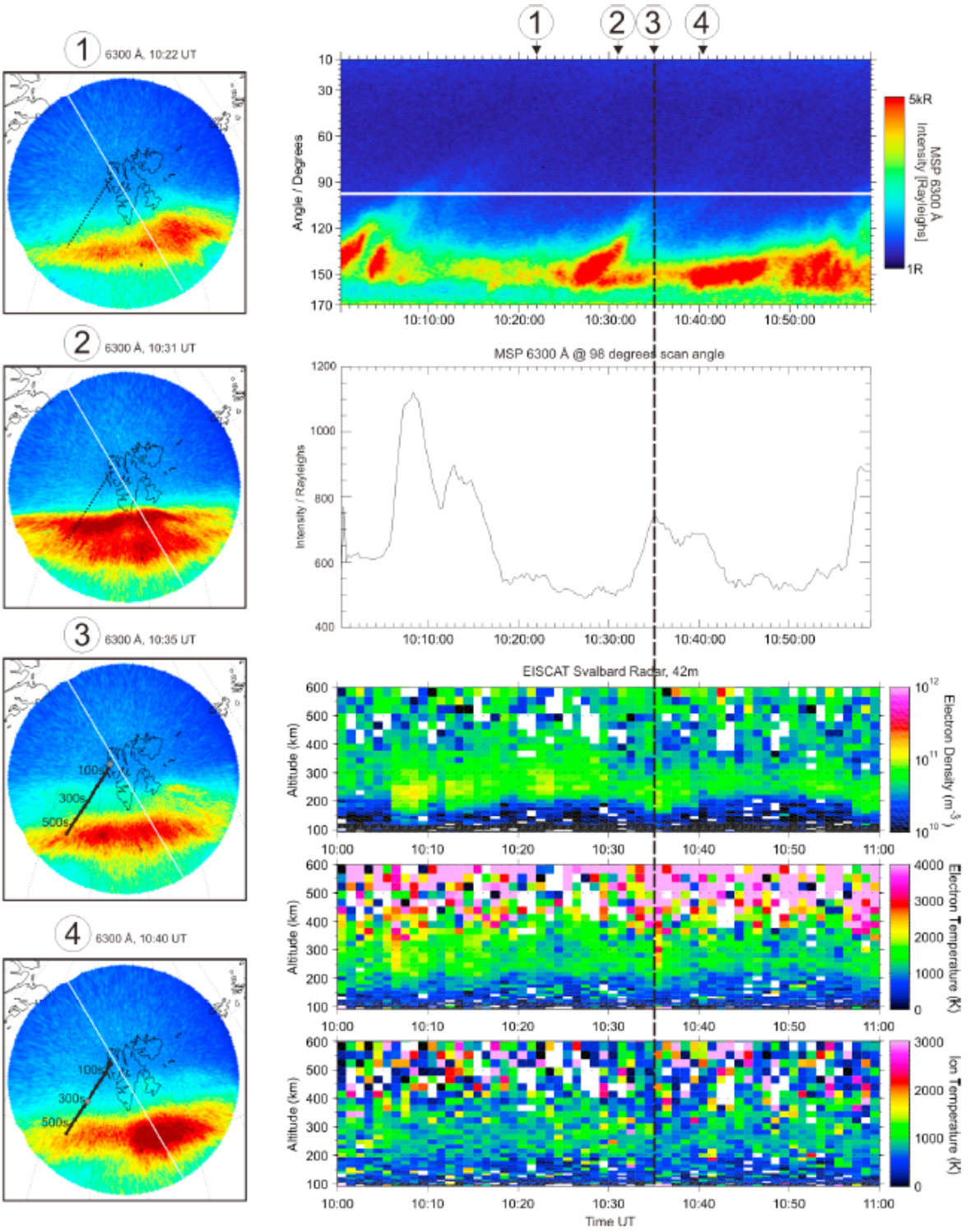

Figure 4.1: left row) All-sky Imager data for different times mapped at $h = 220\,\text{km}$ altitude onto a geographical reference frame. The white line shows the field of view of the 42 m Eiscat Svalbard Radar (ESR) and the dashed black line represents the rocket trajectory with the flight times. right row) Meridian Scanning Photometer and ESR field aligned data on the 05.12.2008. Figure from Lorentzen et al. (2010).

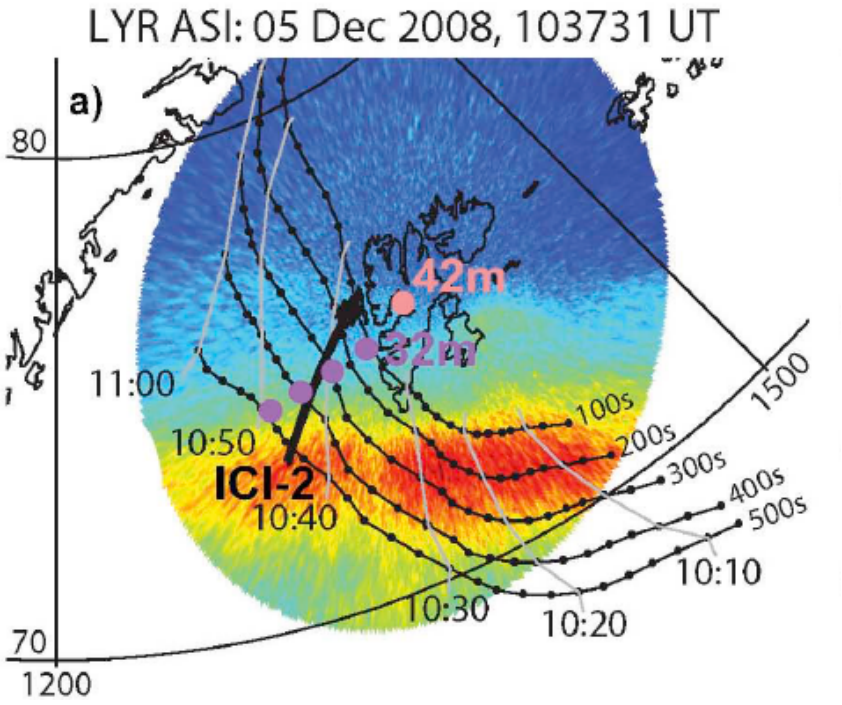

Figure 4.2: Plasma history at $h \approx 200\,\mathrm{km}$ altitude over Svalbard around ICI-2 flight time using superDARN data superposed on All-sky Imager data. The black lines show the time history of individual plasma parcels and the black dots indicate 2 minutes intervals. The gray lines indicate the universal time every 10 minutes. Figure from Oksavik et al. (2012).

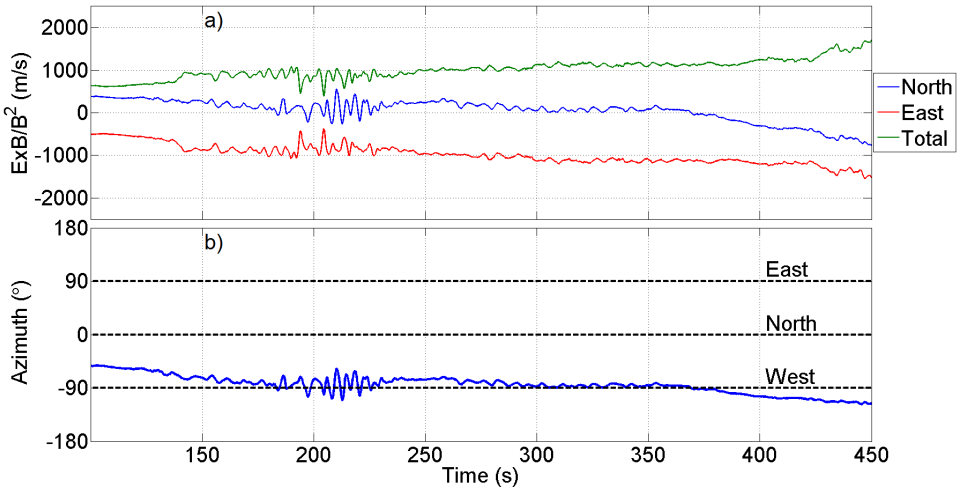

Figure 4.3: a) Norm (green), northward (blue) and eastward (red) components of the $\mathbf{E} \times \mathbf{B}/B^2$ velocity in an Earth-fixed reference frame (NED). b) The direction of the plasma flow with regard to the azimuth angle. The velocity was predominantly directed towards west.

The velocity orientation and magnitude are consistent with the flow history presented above and the superDARN data. Figure 4.4 shows four velocity maps close to Svalbard obtained from superDARN, the transpolar potential and the direction of the magnetic field before the launch and during the ICI-2 rocket flight. In all four panels, the flow is mainly directed towards west with velocities in the range $\mathbf{v} \in [1000, 1250]\,\mathrm{m/s}$. The measurements obtained on board of the spacecraft provide thus reliable information concerning the plasma flow orientation and magnitude.

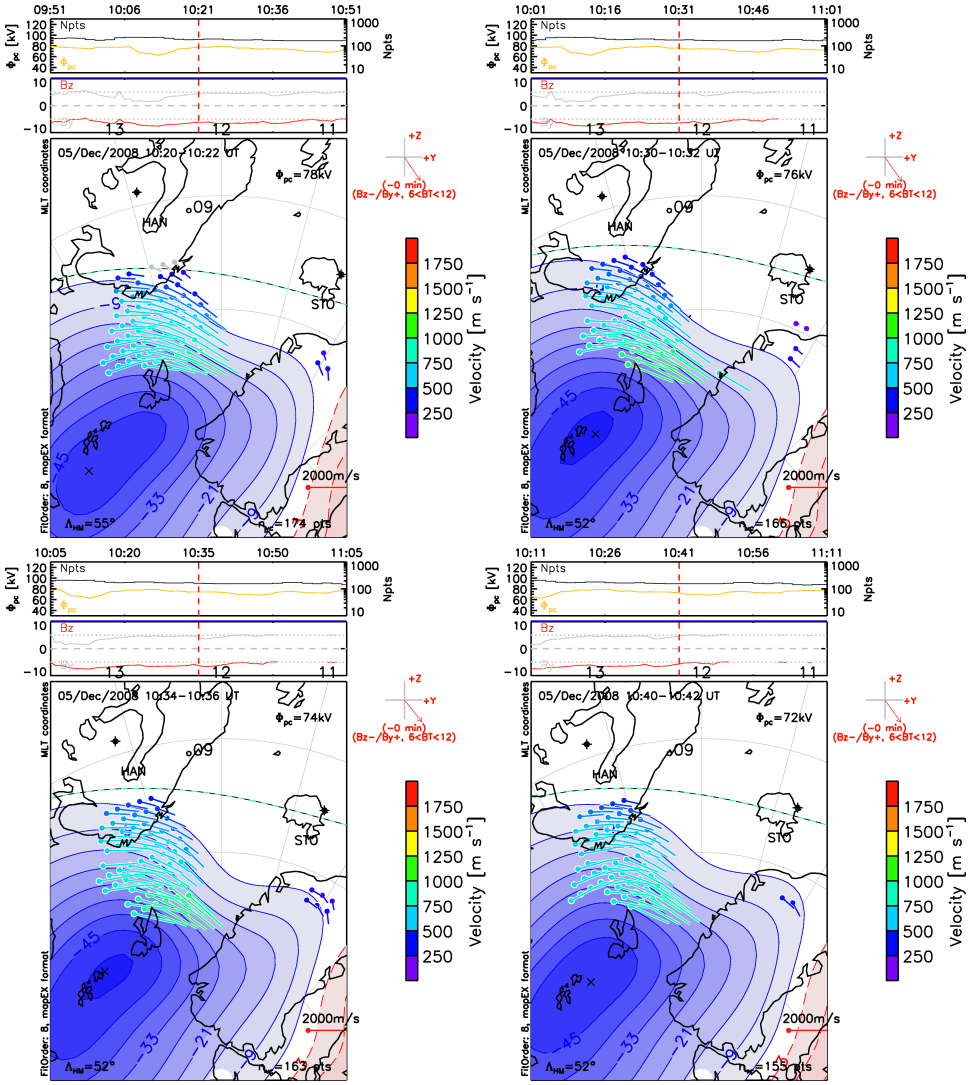

Figure 4.4: SuperDARN velocity maps over Svalbard. The bottom-left corner of each panel corresponds roughly to the geographic north direction. The ICI-2 rocket flew from Svalbard (in the center) approximately towards Iceland, were STO is written. On top of each panel, the polar-cap cross potentials are shown, as well as the IMF B_z component. The two top panels and the two bottom panels show the plasma velocities before and during the ICI-2 launch, respectively. The flow close to Svalbard was mostly westward, in the range $\mathbf{v} \in [750, 1250]\,\mathrm{m/s}$. Courtesy of Dr. Lasse Clausen, Olso, April, 2013.

To summarize, transient dayside reconnection occurred during the minutes prior the launch of the ICI-2 sounding rocket, allowing direct entry of plasma into the polar cusps at F-region altitudes. Several PMAFs were observed and moved westward and poleward in agreement with the convection pattern for IMF $B_y > 0$ and IMF $B_z < 0$ (see section 2.3.3 and Figure 4.4). The electron density enhancements encountered during the ICI-2 flight were probably created South-East of the rocket trajectory and moved into the polar cap. For example, at 1031 UT, the aurora at $h \approx 250\,\text{km}$ altitude intensified, from which a large density enhancement associated with cold plasma moved into the polar cap (Lorentzen et al., 2010).

The ICI-2 sounding rocket was launched with an azimuth angle of 205° towards South-West in a westward moving plasma (see Figure 4.2 and 4.3). In order to know the origin and the direction of motion of the density sampled by the rocket, one needs to consider the relative velocity between the plasma and the spacecraft. It is then possible to know whether the rocket measures structures moving towards it or away. Figure 4.5 a) shows the northward and eastward components of the relative plasma flow. The northward value is about $v_{rel} = 1000\,\text{m/s}$ until $t_{of} = 370\,\text{s}$, where it starts decreasing and the westward component changes gradually from approximately $v_{rel} = 0\,\text{m/s}$ to $v_{rel} = -1000\,\text{m/s}$. This implies that $\mathbf{v}_{rel}$ is pointing northward at the beginning of the flight and rotates westward. The flow direction seen by the rocket can be better observed in Figure 4.5 b) showing $\mathbf{v}_{rel}$ with respect to the azimuth angle. The direction is indeed facing North at $t_{of} = 100\,\text{s}$ and West at $t_{of} = 450\,\text{s}$, which correspond to altitudes $h = 148.3\,\text{km}$ and $h = 232.2\,\text{km}$ respectively and is well located in the F-region.

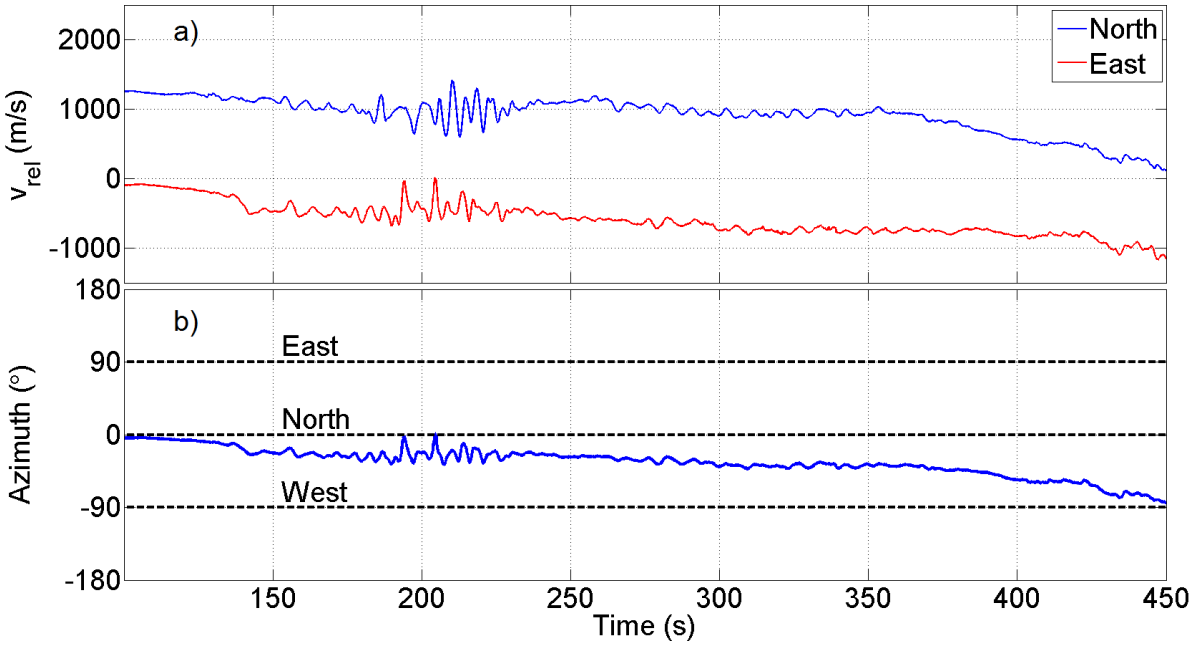

Figure 4.5: a) Relative velocity of the plasma seen by the rocket. b) The direction of $\mathbf{v}_{rel}$ with regard to the azimuth angle. The velocity was pointing north in the beginning and rotated towards west during the flight.

4.2 Overview of the electron density measured during the ICI-2 flight

From the currents measured by the 4-needle Langmuir probes on the ICI-2 sounding rocket, the raw electron density was obtained using Eq. (3.3). Figure 4.6 a) shows the raw density between $t_{of} = 100\,\text{s}$ of flight, corresponding to an altitude $h = 148.28\,\text{km}$, and $t_{of} = 450\,\text{s}$ of flight, when the rocket was at $h = 232.25\,\text{km}$. Referring to section 2.2.2, the F-region ionosphere usually begins at approximately $h = 150\,\text{km}$, meaning that the altitude range considered is located in the F-region. The data appears very noisy due to the spinning of the rocket at a frequency $f = 3.25\,\text{Hz}$. The measurements were filtered using band-reject filters to remove the spin frequency of the spacecraft and its three following harmonics (2nd,3rd and 4th harmonics). The filtering process is explained in more details in Jacobsen et al. (2010). The processed electron density measured with respect to the time of flight t_{of} and the altitude h is shown in Figure 4.6 b).

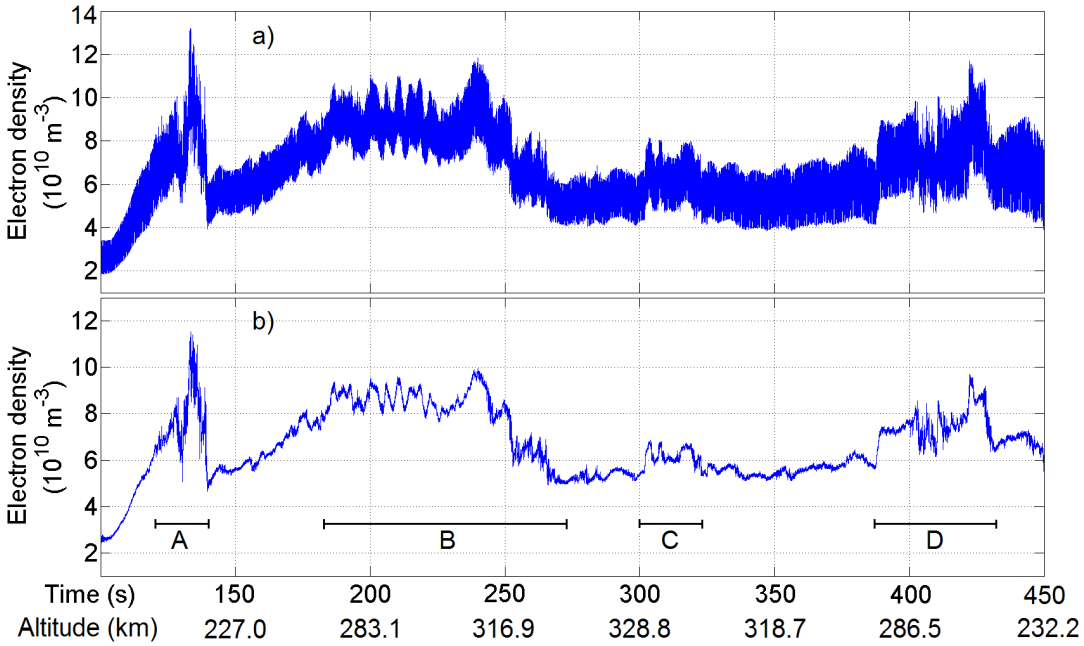

Figure 4.6: a) Raw electron density measured by the 4-Needle Langmuir Probes on the ICI-2 sounding rocket. The data is dominated by the spin rotation of the rocket. b) Processed electron density. The maximum density was $11.5 \cdot 10^{10}\,\text{m}^{-3}$ at $t_{of} \approx 135\,\text{s}$. Four large-scale density enhancements are visible. They are labeled **A**,**B**,**C** and **D**.

Four large structures of density enhancements can be seen in Figure 4.6, labeled **A**, **B**, **C** and **D**. As a consequence of the westward plasma motion presented in 4.1, it is possible to make the assumption that the left-hand sides of the density enhancements seen in Figure 4.6 correspond to their leading edges while the right hand sides match their trailing edges. In other words, the positive gradients correspond to the front side of the structures, while the negative gradients correspond to their backsides. Note however that since the motion of the plasma was not exactly in the same direction as the rocket, zonal flows cannot be completely excluded. The four structures abovementioned are:

- **Region A**: The first strong density enhancement crossed the path of the rocket on the up-leg between $t_{of} = 120\,\mathrm{s}$ and $t_{of} = 140\,\mathrm{s}$ of flight. It coincides with the bottom of an intense F-region plasma patch that has been traveling from lower latitudes, as described in Lorentzen et al. (2010) and Oksavik et al. (2012). The density reached a maximum of $N_e = 11.5 \cdot 10^{10}\,\mathrm{m}^{-3}$ at $t_{of} = 135\,\mathrm{s}$, corresponding to an altitude $h = 205\,\mathrm{km}$. This value was also the maximum density encountered during the entire ICI-2 flight. On the trailing edge of the patch, the density decreased very abruptly from $N_e = 9.8 \cdot 10^{10}\,\mathrm{m}^{-3}$ to $N_e = 5 \cdot 10^{10}\,\mathrm{m}^{-3}$ in $t_{of} \approx 6\,\mathrm{s}$. Using the horizontal velocity $v_{rel} \approx 1200\,\mathrm{m/s}$, the density gradient is $\Delta Ne/\Delta x \approx -6.7 \cdot 10^{9}\,\mathrm{m}^{-3}/\mathrm{km}$ and contains strong fluctuations, implying that some irregularity might be taking place.

- **Region B**: The second density enhancement was also observed on the up-leg, between $t_{of} \approx 180$ s and $t_{of} \approx 270\,\mathrm{s}$ of flight. This region is much broader than the first one. On the top of the structure, between $t_{of} \approx 200\,\mathrm{s}$ and $t_{of} \approx 225\,\mathrm{s}$, the electron density exhibits a wave pattern at about $N_e \approx 9 \cdot 10^{10}\,\mathrm{m}^{-3}$ with frequency $f \approx 0.25\,\mathrm{Hz}$. As it will be shown later, the trailing edge of the density enhancement exhibits sawtooth-like structures with strong fluctuations between $t_{of} \approx 250\,\mathrm{s}$ and $t_{of} \approx 270\,\mathrm{s}$ of flight. The strong fluctuations might imply that some irregularity process is developing. Note indeed that Hysell et al. (1994) found the same type of density structures, i.e. ressembling saw-teeth, in the equatorial region and associated them with plasma irregularities.

- **Region C**: The rocket encountered an increase in density around apogee between $t_{of} \approx 300\,\mathrm{s}$ and $t_{of} \approx 320\,\mathrm{s}$ of flight. Apogee was indeed achieved after $t_{of} = 302\,\mathrm{s}$ of flight (see section 3.2). The density increment is about $1.8 \cdot 10^{10}\,\mathrm{m}^{-3}$ above the background. By looking at Figure 4.7 showing the particle precipitation measured on board for pitch angle $0 - 30°$ (panel b) corresponding to the electrons flowing down along $\mathbf{B}$) and $150 - 180°$ (panel c) corresponding to the electrons flowing up along $\mathbf{B}$), one can see that the plasma enhancement at $t_{of} = 300\,\mathrm{s}$ correlates well with an inverted V-like structure. The low energetic particle experiment (LEP) data are provided by the courtesy of Professor Yoshifumi Saito (ISAS/JAXA), responsible for the LEP experiment (see section 3.2). This correlation between the density enhancement and the inverted V might indicate that particle precipitation played a role in the formation of the density intensification between $t_{of} = 300\,\mathrm{s}$ and $t_{of} = 320\,\mathrm{s}$ of flight.

- **Region D**: On the downleg, the rocket intersected an electron density structure at $t_{of} = 387\,\mathrm{s}$ of flight and $h = 297\,\mathrm{km}$ altitude, corresponding to a cusp electron precipitation region (Moen et al., 2012) and still located in the F-region. The particle precipitation data presented in Figure 4.7 exhibits another inverted V structure well collocated with this region with energies reaching 200 eV. It has been shown by Vickrey and Kelley (1982), that strong precipitation can considerably change the ionospheric conductivity in the E-region, having for consequence that F-region structures would diffuse faster than without precipitation. However, the 200 eV energy cusp precipitations measured by the on-board instrument are not sufficient to affect the E-region conductivity significantly, implying that kilometer scale structures can convect over long distances from their origin (Moen et al., 2012). From the optical recordings, it is known that the auroral activity increased around 1038 UT, i.e., two minutes before encounter (Lorentzen et al., 2010). The density enhancement seen between $t_{of} = 400\,\mathrm{s}$ and $t_{of} = 431\,\mathrm{s}$ might thus be a spatial structure modulated by particle precipitation.

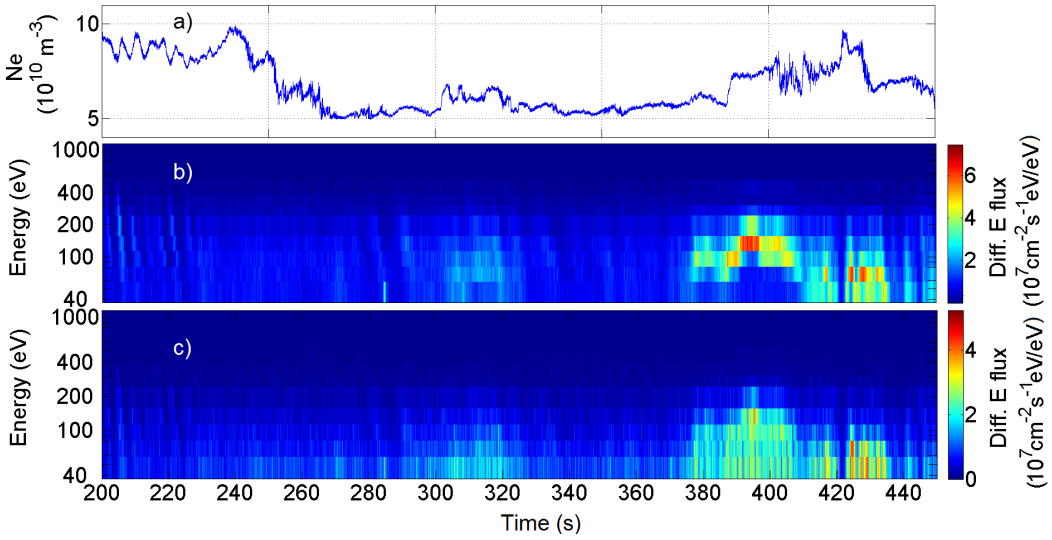

Figure 4.7: a) Electron density measured by the 4-NLP from $t_{of} = 200\,\mathrm{s}$, when the LEP instrument was turned on. b) $0-30°$pitch angle low energetic particle (LEP) precipitating electron flux. c) $150-180°$pitch angle low energetic particle (LEP) precipitating electron flux. Two larger inverted V can be seen at about $t_{of} = 310\,\mathrm{s}$ and $t_{of} = 400\,\mathrm{s}$ of flight. The strongest energy reached is about 200 eV during the second inverted V.

4.3 Spectral analysis using the windowed FFT

In this section, the power spectra obtained by applying windowed Fourier transforms to the electron density fluctuations measured by the ICI-2 sounding rocket are presented. Two parts of the flight have been selected for a more detailed presentation. The first region corresponds to the density enhancement associated with particle precipitation encountered in the end of the flight, i.e. **region D** and the second region matches the large density structure encountered before apogee, i.e. **region B** (see section 4.2). In the end of this section, a general overview of the spectral indices calculated for the entire ICI-2 flight is provided.

4.3.1 Plasma structures at the end of the flight - Region D

The rocket flew through a region of high electron density between $t_{of} = 390\,\mathrm{s}$ and $t_{of} = 430\,\mathrm{s}$ of flight, corresponding to $h = 294.8\,\mathrm{km}$ and $h = 256.7\,\mathrm{km}$ altitude. This part of the flight is the first one investigated since it was described in several articles (e.g. Moen et al., 2012; Oksavik et al., 2012). Figure 4.8 a) shows the electron density enhancement corresponding to a region with cusp electron precipitation (Moen et al., 2012). The maximum density reached during this interval was $9.7 \cdot 10^{10}\ \mathrm{m}^{-3}$ at $t_{of} = 422\,\mathrm{s}$. From the relative motion of the plasma shown in Figure 4.5, one can assume that the increasing density at $t_{of} = 387\,\mathrm{s}$ corresponds to the leading edge of the plasma enhancement while the negative gradient at $t_{of} = 430\,\mathrm{s}$ matches with the trailing boundary of the density structure. The leading edge is very smooth compared to the trailing gradient. Indeed, the electron density contained in the latter is highly fluctuating and contains decameter scales irregularities (Moen et al., 2012). This *preferred direction* with

density fluctuations only on the trailing edges has been observed before (e.g. Cerisier et al., 1985; Basu et al., 1988).

Figure 4.8 b) shows the $0-30°$pitch angle LEP electron flux measured between $t_{of} = 370\,\mathrm{s}$ and $t_{of} = 440\,\mathrm{s}$ of flight. The ICI-2 rocket intersected a 30 km wide inverted V marked INV and four beam filaments (F1-F4) with also an inverted V shape. Comparing 4.8 a) and 4.8 b), we note that the increases in electron density are well correlated with the INV and the beam filaments (see for example F2). Nevertheless, most of the small scales strong perturbations of the density are not associated with the peaks F1, F2, F4 and the largest part of INV (confirmed in Moen et al. (2012)). The exception is the data between $t_{of} = 427\,\mathrm{s}$ and $t_{of} = 431\,\mathrm{s}$, showing strong fluctuations associated with both F3 and a steep density gradient. This interval is thus studied in more details.

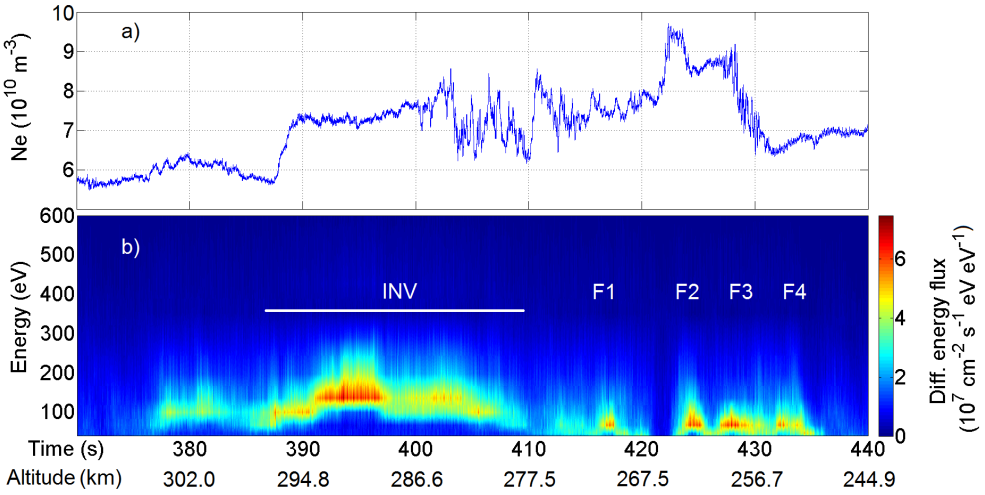

Figure 4.8: a) Electron density enhancement between $t_{of} = 370\,\mathrm{s}$ and $t_{of} = 440\,\mathrm{s}$ of flight. b) $0-30°$pitch angle low energetic particle (LEP) precipitating electron flux.

Figure 4.9 is a close up on the trailing density gradient collocated with an electron beam filament. The density decreased from $N_e = 8.8 \cdot 10^{10}\,\mathrm{m}^{-3}$ to $N_e = 6.5 \cdot 10^{10}\,\mathrm{m}^{-3}$ between $t_{of} = 427\,\mathrm{s}$ and $t_{of} = 431\,\mathrm{s}$ of flight. The relative velocity of the plasma being $\mathbf{v}_{rel} \approx 990\,\mathrm{m/s}$ (see Figure 3.12) during this time interval, the horizontal length scale investigated by the rocket was $L \approx 3970\,\mathrm{m}$, giving a density gradient of $\Delta Ne/\Delta x \approx 5.40 \cdot 10^9\,\mathrm{m}^{-3}/\mathrm{km}$. The fluctuations on the density gradient have both kilometer and meter scales irregularities (as noticed in Moen et al. (2012)). A better overview of these fluctuations can be seen in the top panel of Figure 4.10, showing the Hann windowed density fluctuation $\Delta N_e/N_e$ relative to the trend $(N_e/\langle N_e\rangle_{trend} - 1$, where $\langle N_e\rangle_{trend}$ is the average electron density, shown as a black line in Figure 4.9). The fluctuations are ranging between $-9\,\%$ and $8\,\%$ and resemble squared bite-outs modulated by smaller structures.

The lower panel of Figure 4.10 displays the power spectrum of the abovementioned density fluctuations with logarithmic axis. Since the power spectra at low frequencies are dependent on the detrending process (see section 3.3.2), the figures are only shown from $f_s = 0.8\,\mathrm{Hz}$. In addition, the depletion at approximately $f_s \approx 3.3\,\mathrm{Hz}$ is due to the spin removal and has not been taken into account for the fitting process. From $f_s \approx 300\,\mathrm{Hz}$ ($\lambda = 3.5\,\mathrm{m}$), the quantization noise level is reached, which is detectable in Figure 4.10 as the flat portion at high frequencies, similar to the spectrum of a white noise.

In this thesis, all the structures are assumed to be *frozen in turbulences*. Indeed, Doppler spectra from HF backscatter radars associated with small-scale irregularities indicate that they are low frequency processes, with small phase velocities compared to the convection velocities (e.g. Tsunoda, 1988; Kelley, 2009). However, knowing the ambiguity of such assumption (see section 3.4), the wavelengths and wavenumbers are given as simple indications of length-scales and should not be considered as being exact. As a consequence of Taylor's hypothesis, the time domain can be translated to spatial domain. This implies that low frequencies f_s correspond to long wavelengths λ (or short wavenumbers k) and high frequencies correspond to short wavelengths (or long wavenumbers).

The power spectrum shown in Figure 4.10 b) exhibits two different linear regimes in the frequency interval $f_s = [2, 300]\,\text{Hz}$: one for low frequencies and one for high frequencies. Both ranges join at a *break frequency* $f_{sb} \approx 35\,\text{Hz}$ or $\lambda_b = v_{rel}/f_{sb} = \dfrac{2\pi}{k_b} \approx 29\,\text{m}$. The two slopes are $p_1 = -1.8 \pm 0.3$ and $p_2 = -4.77 \pm 0.2$, implying that the slope at high frequencies is steeper than the slope at lower frequencies. To compute the fits, the data points below 1 Hz and around the spin frequency of the rocket were removed from the series in order to minimize the errors due to the detrending and the filtering processes (see section 3.3.2). Linear least squares were then fitted to each of the linear parts of the spectrum separately, giving the coefficients p_1 and p_2 of a first order polynomial, i.e. $y(x) = p_1 x + p_2$. Note that p_1 gives the slope of the power spectrum in the frequency range selected. The fits were computed both using the *graphical Matlab fitting toolbox*, and the *polyfit* function (see code in Appendix 4.7). The former method is more subjective but it was utile to have a better control over the frequency domains selected (since the spectral knees changes positions and the low frequency part did not have many points to fit). The latter function was then used to automatize the fitting process and minimize the subjectivity. The goodness of the fits was estimated with the coefficient of determination, R^2, ($R^2 \in [0, 1]$, $R^2 = 1$ if the fit is optimal) and the confidence bounds were defined with a level of certainty of 95 %

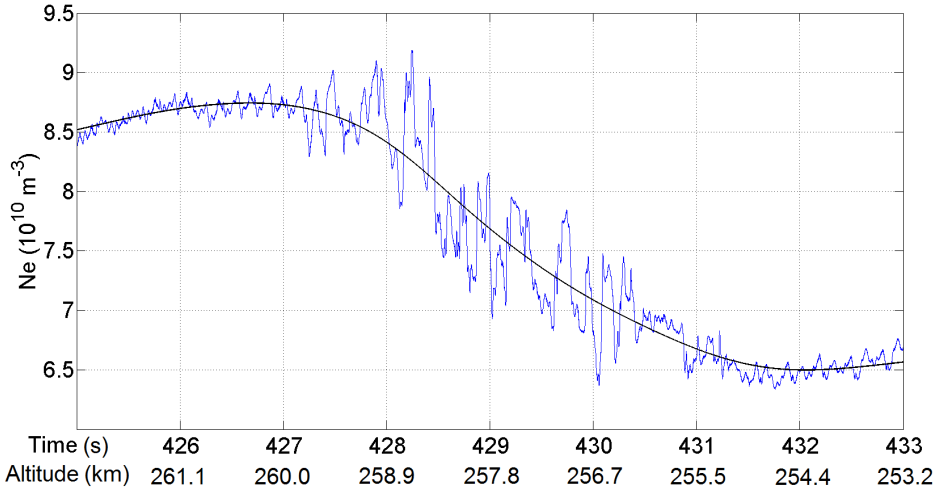

Figure 4.9: Electron density at about $t_{of} = 430\,\text{s}$ of flight. This corresponds to the gradient containing strong irregularities collocated with an electron beam filament. The average electron density is shown as a black line.

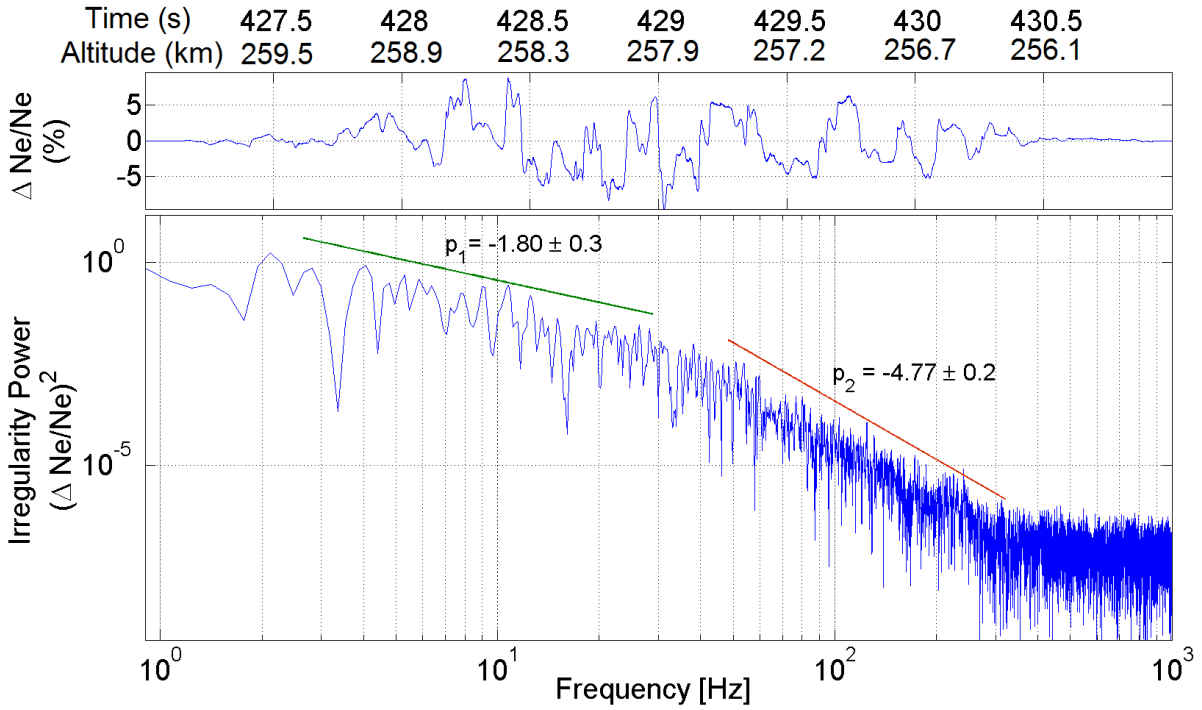

Figure 4.10: (top) Relative electron density fluctuation. (bottom) Power spectrum of the relative electron density fluctuations between $t_{of} = 427\,\mathrm{s}$ and $t_{of} = 431\,\mathrm{s}$ of flight. The slopes of the two parts of the spectrum are $p_1 = -1.80 \pm 0.3$ (with coefficient of determination $R^2 = 0.6$) and $p_2 = -4.77 \pm 0.2$ ($R^2 = 0.81$). The frequency at which the slope changes is $f_{sb} \approx 35$ Hz, which corresponds to a wavelength of $\lambda_b \approx 29$ m.

In order to see whether the power spectra of smooth or strongly fluctuating structures in the plasma density are different, the density shown in Figure 4.9 has been divided into two intervals of 2 seconds, one before the density gradient (between $t_{of} = 425\,\mathrm{s}$ and $t_{of} = 427\,\mathrm{s}$) and one in the middle of the strong irregularities (between $t_{of} = 428\,\mathrm{s}$ and $t_{of} = 430\,\mathrm{s}$). Since the relative velocity of the plasma was $v_{rel} \approx 990\,\mathrm{m/s}$ both intervals correspond to horizontal length scales of $L \approx 1980\,\mathrm{m}$.

The power spectra of the relative electron density obtained for the smooth and highly fluctuating regions are shown in Figure 4.11 a) and b), respectively. The irregularity power is much lower in Figure 4.11 a) than in Figure 4.11 b) and it does not exhibit the dual-slope shape. The spectral index associated with the smooth density is $p_1 = -2.44 \pm 0.3$. Note that the same feature, i.e. a unique slope $p_1 = -2.5 \pm 0.4$ (not shown), is observed when doing a power spectrum for another smooth 2 seconds time interval after the density gradient ($t_{of} = [432, 434]\,\mathrm{s}$). Oppositely the power spectrum of the strongly fluctuating region exhibits two slopes with $p_1 = -1.74 \pm 0.3$ and $p_2 = -4.70 \pm 0.3$. The steepening occurs at a frequency $f_{sb} \approx 35\,\mathrm{Hz}$, corresponding to $\lambda_b \approx 29\,\mathrm{m}$.

The observations suggest that regions with strong density fluctuations are associated with an enhancement of power over the whole frequency range and with the emergence of a dual slope power spectrum.

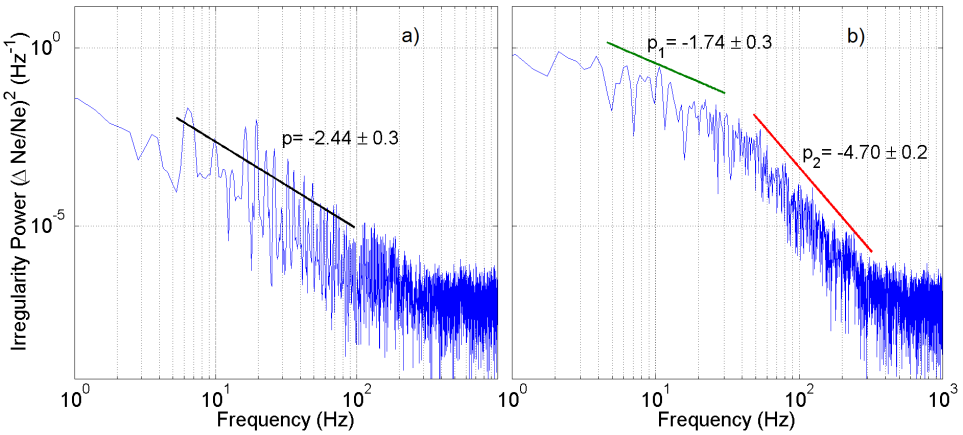

Figure 4.11: a) Power spectrum between $t_{of} = 425\,\mathrm{s}$ and $t_{of} = 427\,\mathrm{s}$ of flight, i.e. just before the strong fluctuations. Only one slope with $p_1 = -2.44 \pm 0.3$ can be fitted to the data. (b Power spectrum between $t_{of} = 428\,\mathrm{s}$ and $t_{of} = 430\,\mathrm{s}$ of flight, i.e. in the middle of the strong fluctuations. The power is much higher than in a) over the whole frequency range and a characteristic dual slope can be observed. The slopes are $p_1 = -1.74 \pm 0.3$ and $p_2 = -4.70 \pm 0.3$.

4.3.2 Plasma structures close to apogee - Region B

The rocket encountered another region with large density irregularities between $t_{of} = 240\,\mathrm{s}$ and $t_{of} = 270\,\mathrm{s}$ of flight, corresponding to the end of region **B**. In contrast to the plasma structures studied in the previous part, there are no electron precipitations in this region. It was selected for closer investigation in order to compare it with the gradient from region **D**, discussed in section 4.3.1. In addition, the rocket being close to apogee, it flew almost perpendicular to the magnetic field, meaning that it was sampling the plasma in the direction $\perp \mathbf{B}$.

According to the convection pattern described in Figure 4.2 and the relative velocity of the plasma presented in Figure 4.5, this region corresponds to the trailing edge of region **B**, described in section 4.2. Figure 4.12 shows the electron density measured by the ICI-2 between $t_{of} = 238\,\mathrm{s}$ and $t_{of} = 275\mathrm{s}$ of flight. Strong fluctuations can be observed on the gradients at $t_{of} = 243\,\mathrm{s}$ and $t_{of} = 252\,\mathrm{s}$ and the region between $t_{of} = 257\,\mathrm{s}$ and $t_{of} = 270\,\mathrm{s}$ exhibits sawtooth-shaped structures with strong fluctuations. These patterns have also been observed in the equatorial regions and Hysell et al. (1994) assimilated them to coherent steepening.

The plasma density between $t_{of} = 262\,\mathrm{s}$ and $t_{of} = 271\,\mathrm{s}$ of flight, or altitude $h \approx 322\,\mathrm{km}$, shown with a black line in figure 4.12 has been chosen and studied in more details here. During this time interval, the rocket sampled plasma on a length scale $L \approx 11000\,\mathrm{m}$ and the Hann windowed relative electron fluctuation is shown in the top of Figure 4.13. The fluctuations range between -12% and 13% and exhibit assymetric structures. The density pertrbations inscrease gradually on the left hand side of the structures and decrease very abruptly on their right hand side. These patterns are different to the ones visible in Figure 4.10, showing structured bite-outs with amplitudes mostly in the range $[-5, 5]\,\%$.

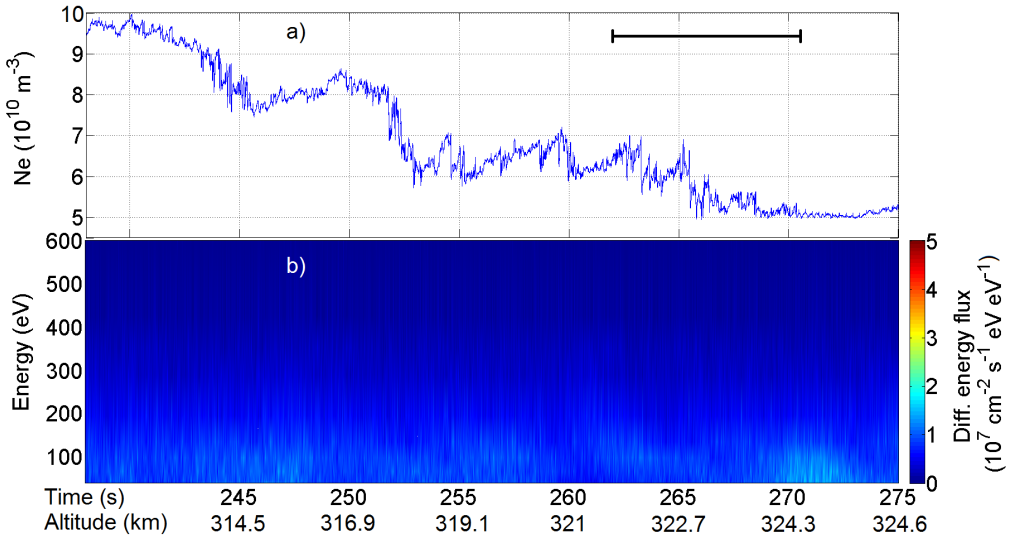

Figure 4.12: a) Electron density between $t_{of} = 248\,\mathrm{s}$ and $t_{of} = 275\,\mathrm{s}$ of flight. This corresponds to the trailing edge of region **B**. The horizontal black line represents the interval considered for analysis. b) $0 - 30°$pitch angle low energetic particle (LEP) precipitating electron flux. Note that the color bar is two order of magnitude smaller than in Figure 4.8 and still, almost no precipitation is seen.

The power spectrum of the density fluctuations measured between $t_{of} = 261\,\mathrm{s}$ and $t_{of} = 271\,\mathrm{s}$ of the flight is shown in the bottom panel of Figure 4.13. The figure is again only shown from $f_s = 0.8\,\mathrm{Hz}$ due to the detrending process (see section 3.3.2) and the depletions at $f_s \approx 3.3\,\mathrm{Hz}$ and $f_s \approx 6.5\,\mathrm{Hz}$ are due to the spin removal and the second harmonic. From $f_s \approx 350\,\mathrm{Hz}$ the noise level is reached. The power spectrum exhibits two linear regimes that merge at about $f_s \approx 43\,\mathrm{Hz}$, or equivalently $\lambda \approx 28\,\mathrm{m}$. The slope for frequencies going from $f_s = 1\,\mathrm{Hz}$ to $f_s = 35\,\mathrm{Hz}$ ($\lambda \approx 1150\,\mathrm{m}$ to $\lambda \approx 33\,\mathrm{m}$) is $p_1 = -1.64 \pm 0.3$ and the slope between $f_s = 45\,\mathrm{Hz}$ and the noise level ($\lambda \approx 27\,\mathrm{m}$ to $\lambda = 3\,\mathrm{m}$) is $p_2 = -4.62 \pm 0.2$. Despite the fact that the density fluctuation profiles are different between the region investigated in the end of the flight and this one, the slopes of their power spectra (compare Figure 4.10 and Figure 4.13) are very similar: both spectra exhibit a dual slope power spectrum with a knee at about 30 m, a slope in low frequency range $p_1 \approx -1.7$ and a slope $p_2 \approx -4.7$ at high frequencies.

As for the gradient in section 4.3.1, the selected density structure has been divided into two shorter intervals of 2 seconds in order to compare strong and low fluctuating regions. Figure 4.14 presents the power spectra of the density fluctuations after the strong irregularities visible until $t_{of} = 270\,\mathrm{s}$ of flight (panel a)) and in the middle of the perturbations (panel b)). The time intervals are $t_{of} = [271.5, 273.5]\,\mathrm{s}$ and $t_{of} = [265, 267]\,\mathrm{s}$ respectively, which correspond to scale lengths $L \approx 2400\,\mathrm{m}$. Again, the power spectrum corresponding to the lower electron density fluctuation (Figure 4.14 a)) only exhibits one power-law, with index $p = -2.13 \pm 0.3$ while the other power spectrum (Figure 4.14 b)) exhibits two slopes, with indices $p_1 = -1.81 \pm 0.3$ and $p_2 = -4.95 \pm 0.2$. The steepening occurs at a frequency $f_{sb} \approx 45\,\mathrm{Hz}$, corresponding to $\lambda_b \approx 26\,\mathrm{m}$.

The same process as discussed for the structures in **region D** seems to occur, that is, an enhancement of the power at all scales accompanied by a dual-slope power spectrum for strong fluctuations, independent of the shape of the irregularity.

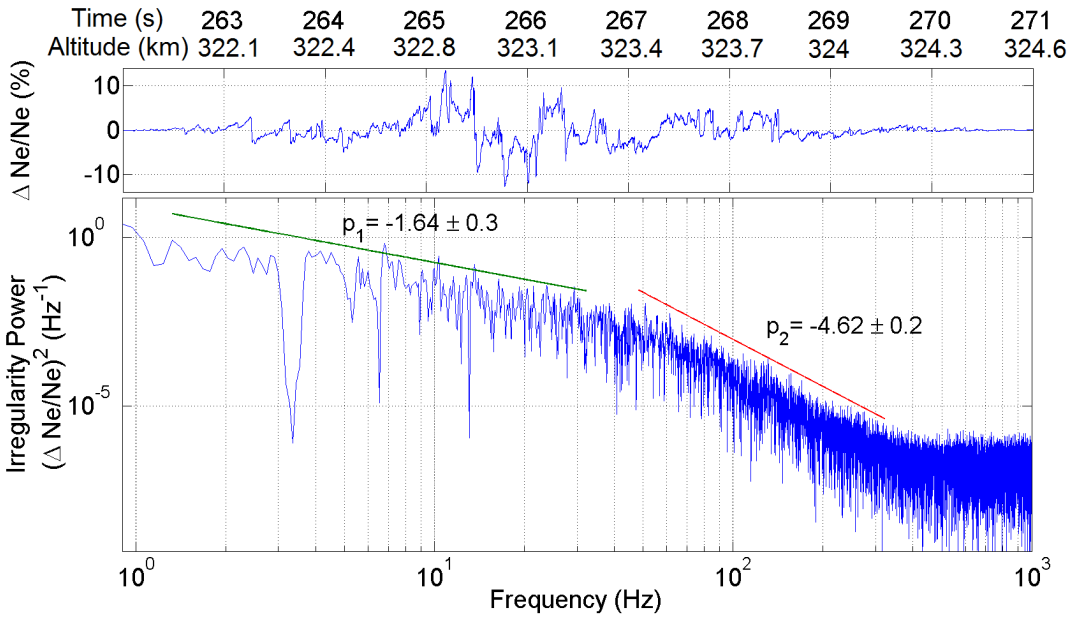

Figure 4.13: (top) Relative electron density fluctuation between $t_{of} = 262\,\mathrm{s}$ and $t_{of} = 271\,\mathrm{s}$ of flight. (bottom) Power spectrum of this interval. The slopes are $p_1 = -1.64 \pm 0.3$ ($R^2 = 0.56$) and $p_2 = -4.62 \pm 0.2$ ($R^2 = 0.77$). The breaking point is ≈ 27 m.

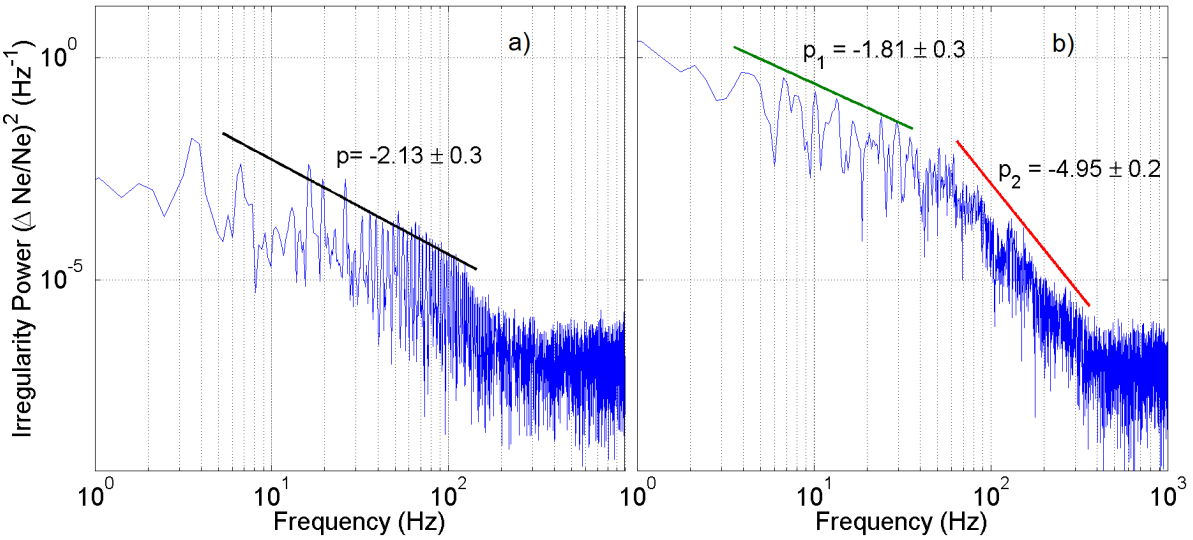

Figure 4.14: a) Power spectrum between $t_{of} = 271.5\,\mathrm{s}$ and $t_{of} = 273.5\,\mathrm{s}$ of flight, i.e., just after the strong fluctuations. b) Power spectrum of highly perturbed electron density between $t_{of} = 265\,\mathrm{s}$ and $t_{of} = 267$ s of flight.

4.3.3 The entire ICI-2 flight

It was demonstrated in sections 4.3.1 and 4.3.2 that despite the fact that the density fluctuations at the end of the flight and before apogee had different shapes, their power spectra exhibited the same features and similar slopes: the strongly fluctuating density gave rise to a dual slope power spectra with enhanced power, while the smoother plasma density was associated with a unique slope and little power.

In order to see whether these spectral characteristics are reproduced throughout the ICI-2 flight, we consider the electron density measured between $t_{of} = 100\,\mathrm{s}$ and $t_{of} = 440\,\mathrm{s}$ of flight. This corresponds to the time just before the rocket crossing with the first enhanced density structure and just after the last one. Figure 4.15 a) presents again the electron density in order to have a visual reference for comparing the plasma structures and the power spectral density (PSD). In Figure 4.15 b), the PSD is shown color coded versus the time of flight and the sample frequency. This type of figure is called a *spectrogram* and it was produced using the sample frequency of the rocket $F_s = 5787\,\mathrm{Hz}$, a Hann window of 6000 data points (corresponding to approximately one second) and an overlap of half a second. Several regions with high irregularity power can be observed. The most intense is between $t_{of} = 120\,\mathrm{s}$ and $t_{of} = 140\,\mathrm{s}$ of flight. The power extends to frequencies of about 90 Hz, which correspond to spatial scales of tens of meters. This result is similar to the one obtained by Oksavik et al. (2012). Two other regions with high PSD can be identified around $t_{of} = 260\,\mathrm{s}$ and from $t_{of} = 400\,\mathrm{s}$. Note that the increase in power occurs at almost all frequencies below approximately 100 Hz and that these regions can be associated with strong electron density perturbations matching with density gradients, as it will be shown later.

Figure 4.15 c) shows the slopes p_1 and p_2 with respect to time of flight/altitude. To produce this figure, the density fluctuation series has been divided into 2 seconds intervals and a power spectrum of each interval has been plotted. The power spectra exhibiting clear features and continuous over a broad enough range have then been fitted by linear polynomials as it has been done earlier in sections 4.3.1 and 4.3.2. Figure 4.15 c) shows the resulting slopes. It is clear that the slopes split into two component several times during the flight. The spectral indices corresponding to the low frequencies are plotted in blue (p_1) and the indices corresponding to higher frequencies are plotted in red (p_2). The slopes p_2 are always steeper than p_1 and the power spectra exhibiting dual slopes are often collocated with the enhanced PSD in Figure 4.15 b) and electron density gradients abovementioned.

A better estimate of the spectral indices of the dual-slope power spectra shown in Figure 4.15 can be obtained by computing the histogram of the slopes p_1 and p_2. Figure 4.16 presents such histograms, with the slope in the x-axis and the number of occurrence in the y-axis. The values for p_1 (left panel in Figure 4.16) are scattered between $p_1 = -2$ and $p_1 = -0.4$ but 60% of the values are contained between $p_1 = -1.5$ and $p_1 = -2$. Spectral indices in the range $p \in [-1, -2]$ have been observed several times in previous high-latitude satellite experiments (e.g Phelps and Sagalyn, 1976; Singh et al., 1985; Cerisier et al., 1985; Basu et al., 1990; Kivanc and Heelis, 1997). The results of this study provides thus another confirmation that the slopes of the power spectra of strong plasma density fluctuations are in the range $p_1 \in [-1, -2]$ for low frequencies.

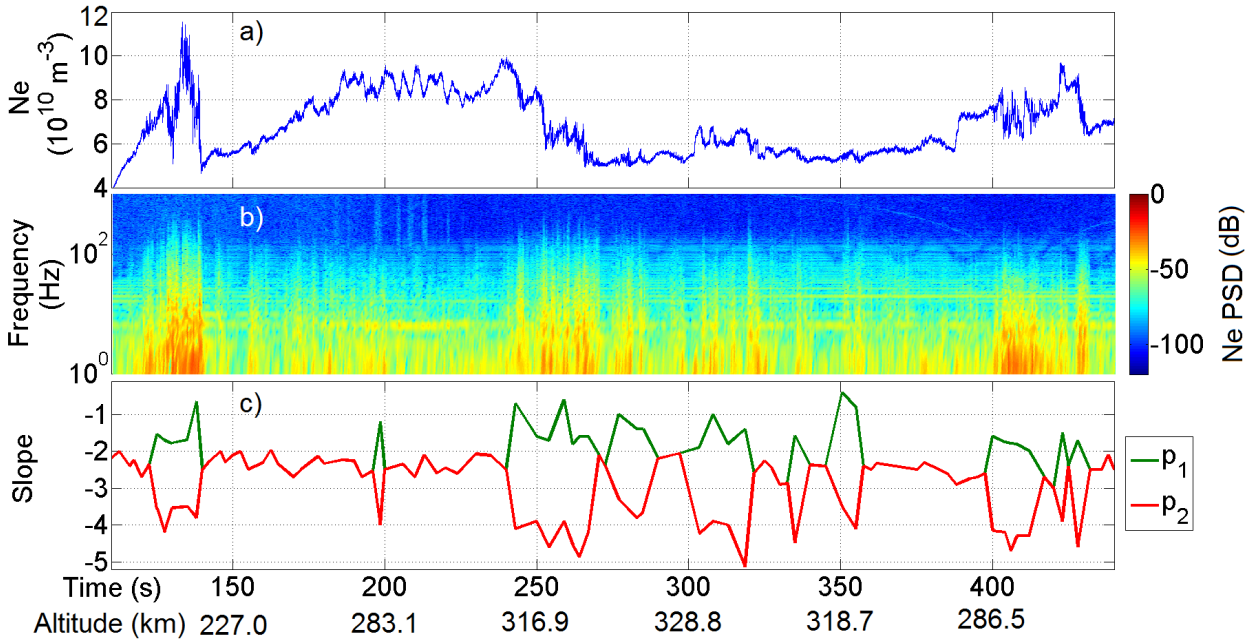

Figure 4.15: a) Electron density measured by the 4-needle Langmuir probes on the ICI-2 rocket. b) Power spectral density of the whole flight. The spectrogram has been performed using one second intervals, a Hann window and half a second overlapping. c) Slopes of power spectra made approximately every 2.5 seconds for time intervals of 2 seconds. The value p_1 corresponds to the slope of the low frequency range, while p_2 corresponds to slopes at high frequencies.

In contrast to the previous studies cited above, the high sampling rate of the ICI-2 rocket allowed to resolve structures of meter scales and to compute power spectra with frequencies as high as $f_s = 1000\,\text{Hz}$. The spectral indices p_2 (right panel in Figure 4.16) corresponding to high frequencies are more negative than p_1 implying a steepening of the power spectra. The values are scattered between $p_2 = -5.2$ and $p_2 = -3.4$ with a mean value of $\bar{p}_2 = -4.1$. The previous satellites studies in the high-latitude F-region did not mention an average slope as steep as $p_2 = -4.1$, as it was found here, even though some indicated a steepening of the power spectra (e.g Phelps and Sagalyn, 1976; Basu et al., 1990; Mounir et al., 1991).

The frequencies at which the power spectra steepen are shown in Figure 4.17 (top) and the corresponding wavelengths in Figure 4.17 (bottom). The frequencies are in the range $f_s \in [20, 55]\,\text{Hz}$, corresponding to scale lengths between 25 m and 60 m. Theses scale lengths are in accordance with the results from Mounir et al. (1991) who indicated a possible steepening at 40 m. Note, however, that other larger values such as 800 m (Villain et al., 1986) or 300 m (Tsunoda, 1988) or 125 m (Basu et al., 1990) have been documented. For a magnetic field $B \approx 5 \cdot 10^{-5}\,\text{T}$, the O_+ gyrofrequency is about $f_{O_+} \approx 47$ Hz, which is in the range of the break frequencies. Assuming $T_i = 1000\,\text{K}$, this corresponds to a Larmor radius of $r_L \approx 4\,\text{m}$.

Nevertheless, it is difficult to draw firm conclusions about the relation between the ion gyrofrequency and the observed frequencies because the data include various contributions from Doppler shift effects due to the motion of the rocket and the plasma drifts.

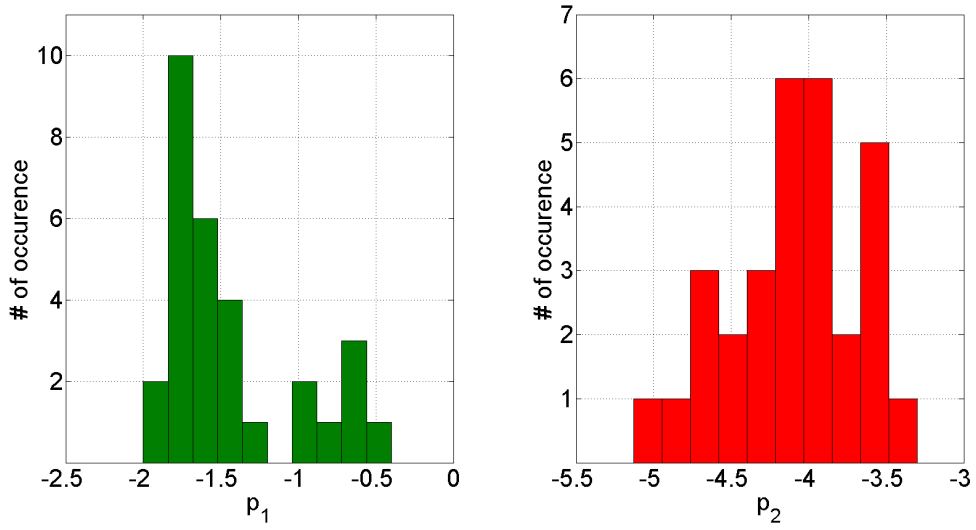

Figure 4.16: Slopes corresponding to the low frequency range (left) and to the high frequency range (right).

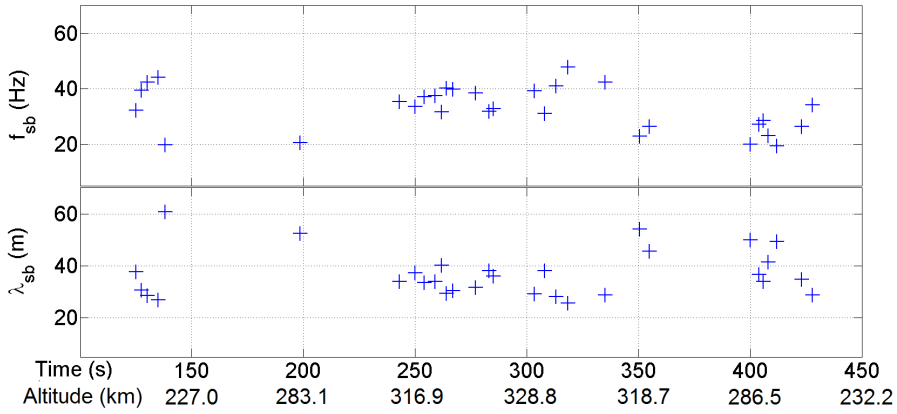

Figure 4.17: Frequencies (top) and wavelengths (bottom) at which the power spectra steepen. The frequencies are in the range $f_{sb} \in [20, 55]$ Hz, corresponding to wavelengths $\lambda_{sb} \in [25, 60]$ m.

In order to minimize the subjectivity in the results, a code providing the slopes of the power spectra with automatic fitting was written. For this purpose the RMS value of the electron density fluctuations have been calculated for two seconds intervals, every half a second. When the irregularity amplitudes were higher than a threshold value of 2 %, windowed FFT were performed on the selected intervals and the power spectra were fitted by polynomials in two frequency ranges. The frequency domains were selected on the basis of the results presented in Figure 4.17, showing that the spectral knees occurred between $f_{sb} = 20$ Hz and $f_{sb} = 55$ Hz. Hence, both ranges for p_1 and p_2 were $[1.7, 26]$ Hz and $[40, 190]$ Hz. The results are shown in Figure 4.18. The top panel in Figure 4.18 presents the RMS values of 2 seconds intervals of the relative electron density fluctuations. Several regions with strong fluctuations can be

identified. They are all located in the plasma enhancements described in section 4.2 and shown in Figure 4.6 b). For visualization purpose, the regions **A**,**B**,**C** and **D** are also shown in Figure 4.18. The strongest relative fluctuations are located between $t_{of} \approx 125\,\mathrm{s}$ and $t_{of} \approx 140\,\mathrm{s}$ and reach 9.8 %. Two other intervals of the flight exhibit higher density fluctuations with values of about 5 %. The first one begins at $t_{of} \approx 250\,\mathrm{s}$ and ends at $t_{of} \approx 270\,\mathrm{s}$. It corresponds to the region analysed in more details in section 4.3.2 and is located on the trailing edge of region **B** (see section 4.3.2). The second starts at $t_{of} = 400\,\mathrm{s}$ and corresponds to region **D**, which was probably due to a plasma spatial structure modulated by particle precipitation (see section 4.3.1). The continuous black line in Figure 4.18 delimits the data taken into account for computing the spectral analysis. The slopes of the power spectra for density fluctuations higher than 2% are displayed in the lowest panel of Figure 4.18. The green and red crosses correspond to the slopes of the low frequency ranges and high frequency ranges, respectively. It is again clear that the spectral indices are smaller at high frequencies, implying a steepening of the power spectra.

The resulting histograms are presented in Figure 4.19. The left panel (green) shows the distribution of p_1, corresponding to the low frequency range (long wavelengths), while the right panel (red) shows the distribution of p_2, matching the high frequency domain (small scales). Since there is less control in the fitting process compared to the manual technique, the values are spread over a larger range than in Figure 4.16. Nevertheless, the results are similar, confirming the spectral indices described in 4.3.3. The values for p_1 are greater than p_2, with averages $\bar{p}_1 = -1.79$ and $\bar{p}_2 = -3.84$, respectively. Note also the peaks of the distributions between $p_1 = -1.5$ and $p_1 = -2$ for low frequencies and at about $p_2 = -4$ for high frequencies.

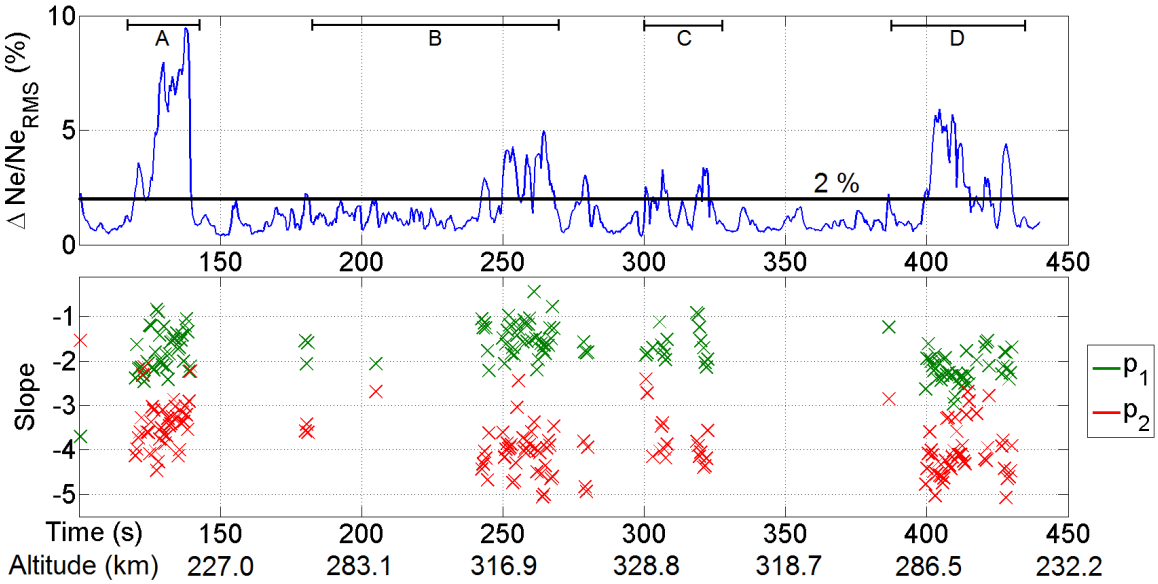

Figure 4.18: (top) RMS values of 2 seconds intervals of the electron density fluctuations. The intervals are computed every 0.5 seconds. The continuous black line represents a 2 % threshold. All four density enhancements (regions **A**-**D**) presented in section 4.2 are shown for visualization purpose. (bottom) Slopes for density fluctuations above 2 %, with p_1 for frequencies $f_{low} \in [1.7, 26]$ Hz (green) and p_2 for $f_{high} \in [40, 190]$ Hz (red).

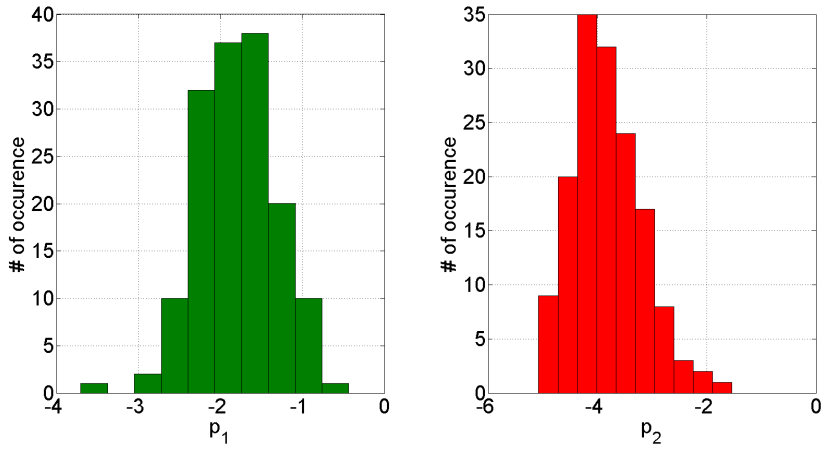

Figure 4.19: Slopes corresponding to the frequency ranges $f_{low} \in [1.7, 26]$ Hz (left) and to $f_{high} \in [40, 190]$ Hz (right).

To summarize, the power spectra associated with enhanced density perturbations exhibit dual-slope power spectra. This feature has been observed throughout the entire ICI-2 flight and no difference in the spectral indices has been observed between the various regions with or without electron precipitations. In this particular case, this might imply that precipitation had not a dominant role in the creating of these double-slope power spectra, but that some other feature (such as gradients) was more important.

4.4 Spectral analysis using Morlet wavelets

In the previous section, the power spectra of the electron density have been computed using FFT on windowed intervals. It is known that Fourier analysis has two limitations: the loss of temporal information about the spectral components and the stationarity hypothesis (see section 3.3.2). However a method called wavelet analysis can overcome these limitations. Hence, in this section, wavelet transforms are applied to the time series in order to acquire complementary results and test the findings of section 4.3.

The first quantity considered here is the electron density during the entire flight. Figure 4.20 (top) shows the plasma fluctuations measured by the ICI-2 sounding rocket. As mentioned in section 4.3.3, four regions containing stronger irregularities can be identified, mainly located in the regions of enhanced plasma density **A**, **B**, **C** and **D** (see section 4.2).

- Between $t_{of} \approx 125$ s and $t_{of} \approx 140$ s of flight. The plasma structure encountered during this time interval is associated with a cold plasma patch (Lorentzen et al., 2010).
- Between $t_{of} \approx 250$ s and $t_{of} \approx 270$ s of flight. This region is collocated with the trailing edge of a plasma enhancement.
- Between $t_{of} \approx 300$ s and $t_{of} \approx 320$ s of flight. The electron density enhancement matches a region with particle precipitation.
- Between $t_{of} \approx 400$ s and $t_{of} \approx 430$ s of flight. The plasma structure encountered during this time interval is probably a density enhancement regulated by particle precipitation.

In addition, a wave-like pattern can be distinguished between $t_{of} = 205\,\mathrm{s}$ and $t_{of} = 230\,\mathrm{s}$. All these structures can be identified in a wavelet spectrogram and studied in detail. This type of figure shows the time evolution of the frequency components of a signal. Figure 4.20 (bottom) presents the wavelet spectrogram of the electron density fluctuations using the Morlet wavelet. The time of flight is displayed in the horizontal axis, the frequency components in the vertical axis and the logarithm of the wavelet power is color-coded. This figure resembles the Fourier spectrogram presented in Figure 4.15 but its resolution is better. The ability of the wavelets to resolve simultaneously high and low frequency components makes it more accurate (see discussion in 3.3.3).

The power at very small frequencies, i.e. $f_s < 0.08\,\mathrm{Hz}$, is low since the quantity considered is the relative electron density fluctuation. The detrending process implies a loss of information in the long wavelength regime, as noted in section 3.3.2. The four irregularity regions listed above are clearly detectable in the wavelet spectrogram due to their enhanced power over a wide range of frequencies covering several order of magnitude. For all four regions the power decreases as the frequency increases, giving rise to vertical structures in the figure. At low frequencies (about $f_s < 0.5\,\mathrm{Hz}$) the strong power is spread over large time intervals but it narrows and forks as the frequency increases, leading to isolated structures.

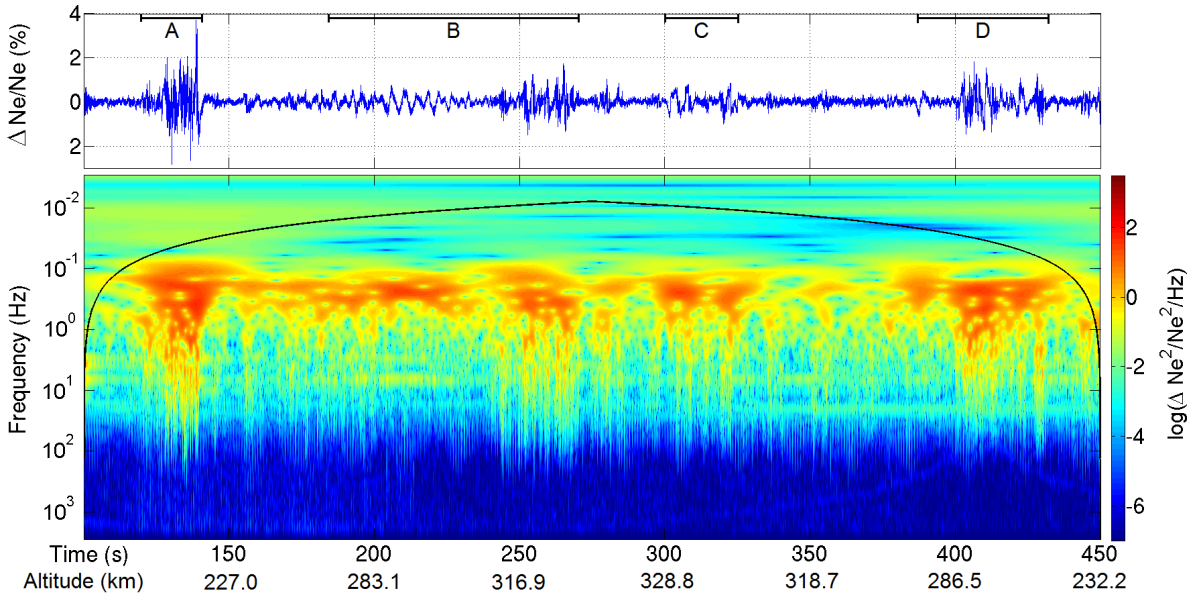

Figure 4.20: (top) Relative electron density fluctuations. The four regions (**A**-**D**) corresponding to enhanced plasma density are shown for visualization purpose. (bottom) Wavelet spectrogram of the electron density. The black line shows the cone of influence (COI).

There are other regions where the power is enhanced in Figure 4.20 (bottom). The strongest one (dark red) is located between $t_{of} = 205\,\mathrm{s}$ and $t_{of} = 230\,\mathrm{s}$ of flight at a frequency of $f_s \approx 0.25\,\mathrm{Hz}$. The time interval and the frequency match well with the wave-like structure seen in the density and electric field fluctuations. Note that this enhanced wavelet power is different to the ones described above, in the sense that very little vertical structures are visible. This means that no small scales irregularity is taking place. In addition, several lines

can be observed during large time intervals of the flight. They also correspond to enhanced power but they can all be related to harmonics of the 3.25 Hz rocket spin frequency. Indeed, all of them are multiple of 3.25 Hz: the first yellow line from the top and visible until about $t_{of} = 220$ s corresponds to the rocket spin frequency; the second yellow line from the top and visible during the whole flight is located at $f_s = 6.5$ Hz which is two times the spin frequency; the turquoise line present during the entire time domain (but best visible from about $t_{of} = 340$ s) corresponds to $f_s = 19.5$ Hz, which is the 6th harmonics of the spin. When processing the data, band-reject filters were used to remove the spin frequency, the second, third and fourth harmonics. The filtering process was seemingly too crude and the range of the filters too small to remove all the spin components at $f_s = 3.25$ Hz and $f_s = 6.5$ Hz. Regarding the power at $f_s = 19.5$ Hz, it is expected to be enhanced since the 6th harmonic was not filtered during the data extraction. These statements have been verified by changing the size of the filters and removing the contributions at $f_s = 19.5$ Hz, which had for consequence the eradication of the three power lines.

The wavelet power at each frequency can be averaged over time in order to obtain figures similar to the power spectra computed by windowed Fourier transforms, i.e., presenting power versus frequency. It is then possible to compare the results provided by both methods. Figure 4.21 presents four FFT and Morlet wavelet power spectra. The time intervals were selected so that the Fourier spectra would have two slopes and thus be paired with regions of strong density fluctuations. The first one, shown in panel a), is $t_{of} = [128, 132]$ s and corresponds to a region of greatly fluctuating plasma located in the middle of the first density enhancement encountered by the rocket. In panel b) the power spectrum of a density gradient associated with high perturbation is presented. The two last panels display the same spectra as the one presented in section 4.3.2 and 4.3.1, corresponding to structures prior to apogee and at the end of the flight. By looking at all four panels, it is clear that both methods give reassembling results: the energies and the slopes are very similar. The Morlet wavelet power spectra exhibit fewer structures but still compare well with the FFT spectra. This is because the wavelet spectra are made of averages of the coefficients at each frequency during the selected time interval. The slopes p_1 and p_2 found in all four panels are given in table 4.1. The values calculated for the Morlet spectra are slightly shallower than for the FFT especially at high frequencies. This was also noticed by Lagoutte et al. (1992) who argued that it was due to somewhat larger power at high frequencies. Note that FFT power spectra contain most of their data in the upper part of the curves despite all the vertical lines visible. These irregularities affect the fitting and tend to make the slopes steeper. By taking an average of the FFT power spectra the slopes are more similar.

Time interval		FFT	Morlet wavelet
a) $t_{of} = [128, 132]$ s	p_1:	-1.6	-1.4
	p_2:	-3.9	-3.7
b) $t_{of} = [243, 247]$ s	p_1:	-1	-0.9
	p_2	-4.59	-4.2
c) $t_{of} = [262, 271]$ s	p_1:	-1.64	-1.4
	p_2:	-4.62	-4.3
d) $t_{of} = [427, 431]$ s	p_1:	-1.8	-1.8
	p_2:	-4.77	-4.3

Table 4.1: Slopes of the windowed FFT and Morlet wavelet power spectra presented in Figure 4.21

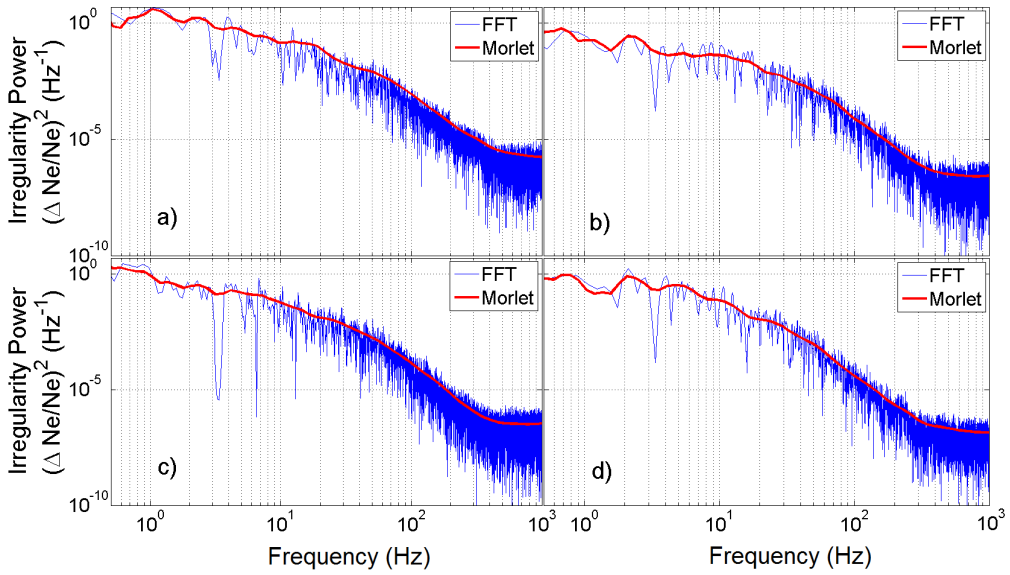

Figure 4.21: Comparison between power spectra obtained with the windowed FFT and the Morlet wavelet for the intervals a) $t_{of} = [128, 132]$ s, b) $t_{of} = [243, 247]$ s, c) $t_{of} = [262, 271]$ s and d) $t_{of} = [427, 431]$ s of flight.

In order to compare more than just four FFT and wavelet spectra, the automated analysis described in section 4.3.3 was also performed using wavelet transforms. That is, calculating the slopes p_1 and p_2 in the frequency ranges $[1.7, 26]$ Hz and $[40, 190]$ Hz for all 2 seconds intervals having fluctuations above 2 %. The histograms of the spectral indices are presented in Figure 4.22, showing both the values for the Morlet and windowed FFT methods (the values for p_1 and p_2 for the windowed FFT are the same as in Figure 4.19). The slopes calculated using the wavelet method in the low frequency domain are within the range $p_{1M} = [-2.30, -0.52]$. They are slightly shallower than for the FFT technique, with a mean value of $\bar{p}_{1M} = -1.45$ (compared to $\bar{p}_{1F} = -1.79$ for Fourier analysis), but still are in rather good agreement. In the higher frequency range, the Morlet spectral indices are also less spread out but the slopes are considerably flatter than for the FFT. The average Morlet slope is $\bar{p}_{1M} = -3.3$, while the FFT average slope is $\bar{p}_{1M} = -3.83$. These values are also in agreement with the particular cases presented in Table 4.1 and are again, likely due to the inherent averaging of the wavelet power spectra.

It was shown that both the FFT and the wavelet techniques provided similar power spectra showing a dual-slope characteristic. Since wavelet analysis does not require any assumption concerning the data, the assumption of stationarity for Fourier transforms can be considered as reasonable. Despite their similarity, the slopes obtained using wavelets were generally shallower than the values given by the Fourier transforms. It is thus legitimate to examine which method is better suited to analyze the data. The wavelets have the ability to produce precise wavelet spectrogram. They are thus ideal to detect frequency components of a signal and are more adequate than the Fourier spectrograms for this purpose. Additionally, wavelet analysis does not require any assumption about the data, provided the cone of influence. However in order to study the slopes of power spectra, the averaging of the wavelet coefficients causes a loss of information. In this sense (and assuming the stationarity of the time series), a more precise knowledge of the spectral indices can be obtained with FFT transforms.

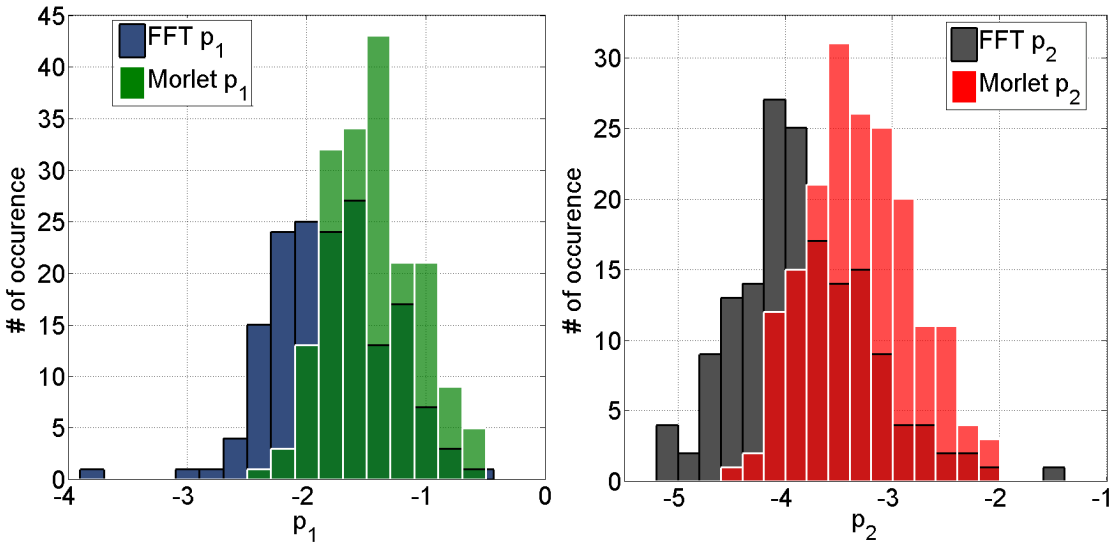

Figure 4.22: Histograms of the slopes corresponding to the frequency ranges $f_{low} \in [1.7, 26]$ Hz (left) and $f_{high} \in [40, 190]$ Hz (right) for the power spectra computed using the FFT and Morlet wavelets.

4.5 Spectral analysis of the electric field measurements

In the previous section, power spectra of electron density fluctuations were presented. However, using the slopes of only this quantity makes it difficult to distinguish between the different instability mechanisms that might be responsible for the observed fluctuations. By looking at table 2.1 in section 2.5.1, for example, one can notice that a power spectrum of $\Delta N_e/Ne$ with slope $p = -5/3$ could either be due to the GDI/CC or the KH instability. However, the analysis of other quantities such as the electric field or the magnetic field could provide additional information. In their review, Kintner and Seyler (1985) also pointed out the necessity to investigate several plasma parameters such as the electron density, the electric, magnetic field and the particle precipitations in order to assess which instability mechanism is occurring. This was for example done by Basu et al. (1990), who compared electric field and density perturbations and found that the values of the electric field fluctuations was at least one order of magnitude larger for velocity shear processes than for the GDI. Mounir et al. (1991) indicated that magnetic fluctuations were also associated with velocity shears. No in-situ magnetic field data are available from the ICI-2 rocket and the DC electric field resolution do not allow to study power spectra in the same way as for the electron density.

Indeed, two difficulties were encountered with the electric field data:

- Originally the sampling rate of the DC electric field measurements was $F_s = 180$ Hz. However, a cut-off of about $f = 40$ Hz was applied to the data in the extraction process. This leads to damped values slightly below $f \approx 40$ Hz and higher in Fourier space, and only some strong frequency components survive the filtering process. Consequently, the frequency range resolvable is more restricted than for the density fluctuations and the comparison between the spectra of both quantities is made difficult.

- There exists an AC electric field data set with frequencies as high as 1.7 kHz. By combining both the DC and the AC components, it would be possible to resolve the signal over a wider frequency range. Regrettably, the final DC electric field data was available about the $10th$ of April 2013, leaving little time for analysis. Now that the DC electric field is correct, the AC data should also be analyzed so a wider frequency range could be studied, providing more information. At the time of writing, only the low resolution data were available and the spectral analysis of the electric field should be reconsidered in future work.

Two different DC electric field time series were used in this work. The major difference between them is the procedure of removing the spin frequency of the rocket, its harmonics and wake effects. The first one was determined assuming that **E** did not change much during one spin of the rocket. Each of the 180 data points per second of the time series is an average over one spin period of the electric field measured by the two probe pairs. The averaging implies that the frequency resolution is much lower than for the density fluctuations and that structures at frequencies higher than about 3.25 Hz (the rocket spin frequency) should not be considered. This electric field series is thus of no help to study structures at small scales. Nevertheless, the spin of the rocket and the wake effects are almost absent in these data and therefore, they give very accurate information concerning the orientation of the electric field. All the figures showing the magnitude or the direction of the plasma flow were computed on the basis of this time series, i.e. Figures 3.12, 4.3 and 4.5.

Since the frequency resolution was too low in the first method, no averaging over the potential values measured by the booms was effectuated in the second electric field time series, here referred as the *combined data*. The sampling frequency was $F_s = 180\,\text{Hz}$ giving a Nyquist frequency of $f_N = 90\,\text{Hz}$ but due to the cut-off, the real frequency range is $f \approx [0, 40]\,\text{Hz}$. For the combined data, the spin frequency and its harmonics were filtered by band-reject filters, as it was done for the electron density. In this section, electric field measurements are briefly described. The averaged data are used to show the different components of the field and their orientations while the combined values are used for spectral analysis.

Figure 4.23 shows the averaged electric field components in an Earth-fixed reference frame with coordinates North-East-Down (NED). These components are obtained by subtracting the induced field $\mathbf{E}_{ind}$ to the in-situ electric field $\mathbf{E}_{rock}$. The northward values increase during the flight from about $E_N = 25\,\text{mV/m}$ to $E_N = 78\,\text{mV/m}$ at $t_{of} = 450\,\text{s}$. The eastward component decreases gradually from $E_E = 20\,\text{mV/m}$ to $E_E = 0\,\text{mV/m}$ at $t_{of} = 369\,\text{s}$, where it starts pointing towards West. The Down component is much smaller. Its values are contained between approximately $E_D = -5\,\text{mV/m}$ and $E_D = -10\,\text{mV/m}$ during the whole flight. This is consistent with plasma convection in the F-region high latitude ionosphere, where most of the motion is perpendicular to the magnetic field (see 2.3.2). The electric field components are quite smooth with some small oscillations except between $t_{of} = 175\,\text{s}$ and $t_{of} = 230\,\text{s}$, where the values exhibit a wave-like structure. The peak to peak drop in the burst reaches 30 mV/m and this oscillating pattern is also noticeable in the density data (see Figure 4.6). Note that when no component is given, the letter E means the norm of **E** perpendicular to **B**. The perturbations are almost nonexistent during the whole flight (approximately 1 %, as shown later) except between $t_{of} = 150\,\text{s}$ and $t_{of} = 230\,\text{s}$, where the low frequency wave pattern was observed.

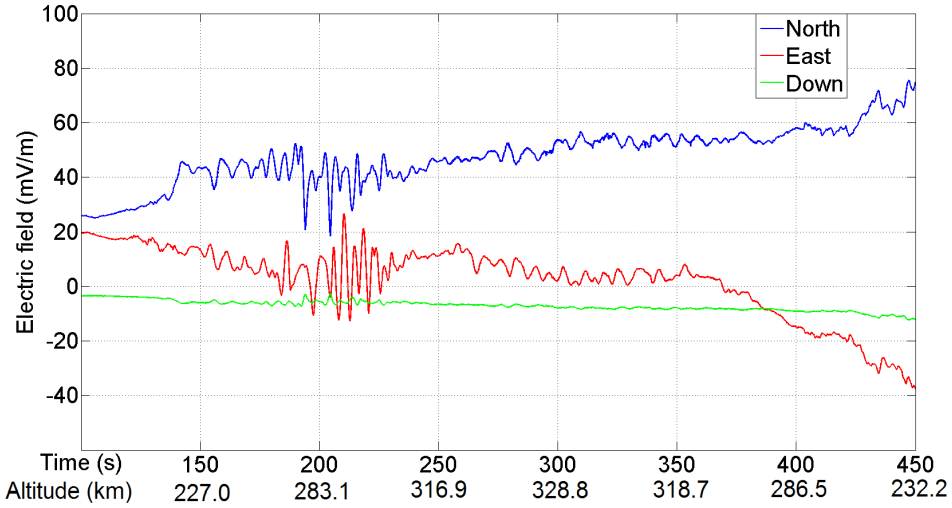

Figure 4.23: Electric field measured on-board the ICI-2 rocket and transposed into an Earth-fixed reference frame North-East-Down (NED). The electric field does not exhibit much structures (compared to the electron density shown in Figure 4.6) except between $t_{of} \approx 175\,\mathrm{s}$ and $t_{of} \approx 230\,\mathrm{s}$ of flight. This region shows a wave-like pattern with frequency $f \approx 0.25\,\mathrm{Hz}$.

Most of the fluctuations are only present at large scales and the small scales are dominated by the spin frequencies or simply not resolvable. This can be seen in Figure 4.24. Figure 4.24 a) shows the combined electric field fluctuations $\Delta E\,\mathrm{mV/m}$ with respect to time. The spin and the six following harmonics have been removed using band-reject filters. The values presented are still noisy and it is clear that some frequencies due to the rotation of the spacecraft or wake effects are still present.

Figure 4.24 b) presents the spectrogram of the combined electric field data. The turquoise lines at 3.25 Hz, 6.5 Hz and 26 Hz correspond to the rocket spin frequency, the 2nd harmonic and the 8th harmonics, respectively, which have not been removed during the filtering process. In addition, one can observe that every structure above about 25 Hz is dominated by the rotation of the rockets.

The largest structure detectable is the wave-like pattern between $t_{of} \approx 175\,\mathrm{s}$ and $t_{of} \approx 230\,\mathrm{s}$ of flight. The frequency of the wave is $f \approx 0.25\,\mathrm{Hz}$ as it was for the electron density fluctuations (see Figure 4.20). The wavelet power extends to about $f = 1\,\mathrm{Hz}$ and drop drastically meaning again that little small scale fluctuations are present in this region.

The most striking feature visible in Figure 4.24 b) is the lack of enhanced wavelet power above 1 Hz, implying little (or no) irregularity are small scales. This is clearly different to the spectrogram of density fluctuations which exhibited strong power at frequencies as high as 100 Hz (see again Figure 4.20). The lack of power above 10 Hz, the small number of data and the influence of the detrending process at low frequencies makes it laborious to compute FFT power spectra with significant slopes and to compare them to the indices found for density fluctuations. Therefore, the spectral characteristics of the electric field perturbations should be further analyzed when the new data will be available. However we give here an insight in a feature observed for the electric field fluctuations that seems to be associated with irregularities in density and that should be further studied with the AC data sets:

There is an enhancement in the electric field fluctuations power associated with density

perturbations. Indeed, in Figure 4.24 b), stronger power can be seen extending to higher frequencies (about 25 Hz) between $t_{of} \approx 120\,\mathrm{s}$ and $t_{of} \approx 140\,\mathrm{s}$, between $t_{of} \approx 290\,\mathrm{s}$ and $t_{of} \approx 350\,\mathrm{s}$ and $t_{of} \approx 400\,\mathrm{s}$ and between $t_{of} \approx 430\,\mathrm{s}$, corresponding to the regions with enhanced density fluctuations presented in section 4.2. This feature can also be seen in the FFT spectra of the electric field showing an increase in power at frequencies between $f \approx 0.5\,\mathrm{Hz}$ and $f \approx 30\,\mathrm{Hz}$. An example is given in Figure 4.25 showing the power spectra of $\Delta E/E$ for $t_{of} = [427, 431]\,\mathrm{s}$ (left) and $t_{of} = [433, 437]\,\mathrm{s}$ (right). The first time-interval, i.e. $t_{of} = [427, 431]\,\mathrm{s}$, matches the density gradient with strong irregularities studied in section 4.3.1 and the second, $t_{of} = [433, 437]\,\mathrm{s}$, corresponds to a smoother region. The enhancement in power is visible in the left panel of Figure 4.24.

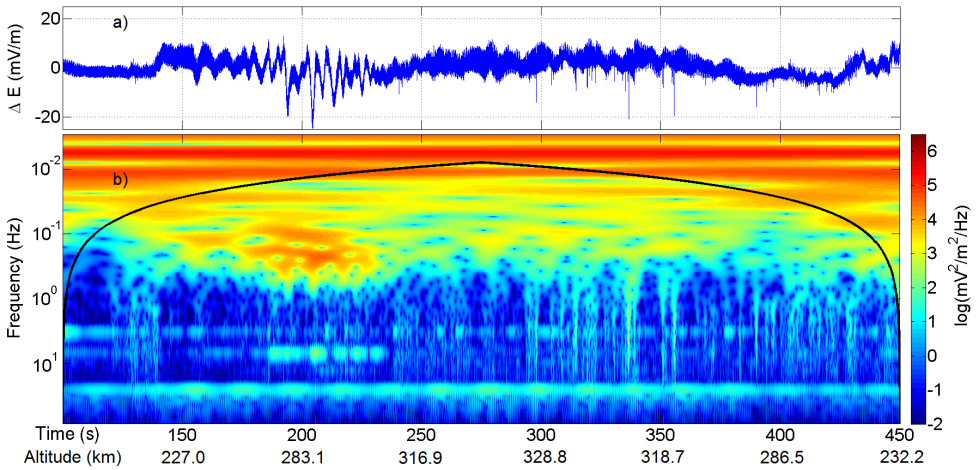

Figure 4.24: a) Relative fluctuations of the combined electric field. b) Wavelet spectrogram of the time series shown in a). The black line shows the cone of influence (COI).

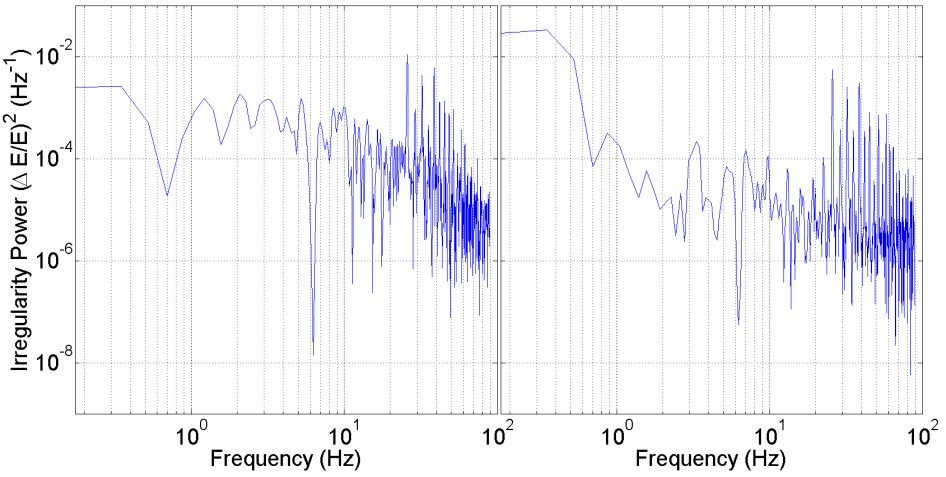

Figure 4.25: Power spectra of $\Delta E/E$ for (left) $t_{of} = [427, 431]\,\mathrm{s}$ and (right) $t_{of} = [433, 437]\,\mathrm{s}$. The irregularity power is slightly enhanced in the left panel, corresponding to a region with strong fluctuations is electron density.

4.6 Discussion of the results

Many mechanisms have been proposed in the literature for the generation of plasma irregularities in the high latitude ionosphere. Among them are the gradient-drift instability, the current-convective instability, the ion cyclotron instability, drift waves, ion acoustic waves, velocity shears, structured particle precipitation, turbulent electric fields (e.g. Tsunoda, 1988; Ossakow and Chaturvedi, 1979; Kelley et al., 1980; Walker et al., 1991; Carlson et al., 2008; Kelley, 2009; Oksavik et al., 2012) and the free energy available for their generation is also multiples: density and temperature gradients, electric fields, FAC, shear flows etc.

Several processes might be occurring at the same time or subsequently. Consequently, in order to assign an instability mechanism to a observed irregularity, one should have an exhaustive knowledge of the plasma structures, temperatures, electric and magnetic fields. Kintner and Seyler (1985), Basu et al. (1990) and Mounir et al. (1991) also argued that several quantities should be analyzed for discerning between different instability mechanisms in the ionosphere. An additional complexity rises from the ambiguity in determining the power spectrum of the plasma structures in their own rest frame, as the rocket only samples a cut in the plasma (see section 3.4.1). Also related to this restriction of one-dimensional sampling is the difficulty to distinguish between quasi-stationary and turbulent/irregularity structures. Indeed, each measurement is made at a precise location in time and space and, as a consequence of the relative motion between the rocket and the plasma, a limited picture of the spatio-temporal evolution of the plasma structures is obtained. However, as noted in section 3.2, the ICI-2 rocket allowed in-situ measurements with an unprecedented sampling rate providing meter-scale resolution of electron density structures, which would be impossible for ground-based radars. In addition to the rocket data, the other instruments cited in section 3.1 provided a good overview of the plasma flow conditions and the space-physics phenomena occurring during the ICI-2 flight.

Hence, even if it is difficult to draw firm conclusions with this set of data, we are able to discuss which candidates are the most likely mechanisms producing the strong fluctuations in the electron density observed by the ICI-2 sounding rocket. In this section, the results obtained from the spectral analysis of the ICI-2 data are first compared with previous in-situ studies in order to put them in a wider context. Then, the results are discussed with respect to several instability and turbulence mechanisms.

4.6.1 Comparison with earlier results

The power spectra of the strongly fluctuating electron density structures presented in this study exhibit dual-slope characteristics, as described in section 4.3. The frequency range of the spectral knees is $f_s = [2, 55]$ Hz, which is in the range of the oxygen ion gyrofrequency (see section 4.3.3). For power spectra of 2 seconds intervals, the mean slope of the low frequency regime (i.e. between $f_s = 1.7$ Hz and $f_s = 26$ Hz) is $\bar{p}_1 = 1.79$. For frequencies between 40 Hz and 190 Hz (close to the noise level), the mean slope is $\bar{p}_2 = -3.84$.

Several other spacecrafts were launched into the ionosphere to study the power spectra of electron density irregularities. Table 4.2 presents an overview of most of the results found in the existing literature concerning spectral index classifications of high latitude F-region density fluctuations. The spectral shape of the form $(\Delta Ne/Ne)^2 \sim k^{-p_1}$ has been observed several times.

In 1974, Dyson et al. (1974) studied power spectra of ion concentrations observed by satellites over a scale-size range of 70 m to 70 km. They obtained values close to $p_1 = -1$ and found that these slopes were insensitive to the irregularity amplitude. They thus suggested that large-scale structures of about 10 km dissipate their energy creating smaller-scale structures, as expected for turbulent flows.

Singh et al. (1985) analyzed data obtained by satellites in the auroral oval, in the polar cap and in the dayside/cusp region. They studied the power spectra of the density fluctuations in these different regions with scale size ranging from hundreds of kilometers to hundreds of meters. At altitudes between $h = 280$ km and $h = 300$ km, Singh et al. (1985) found indices $p_1 = -1.9$ in the three abovementioned regions.

Cerisier et al. (1985) inspected electron density fluctuations measured by a satellite flying in the high latitude topside F-region below $h = 2000$ km altitude. They investigated asymmetric density enhancements exhibiting strong irregularities on one edge and assimilated the instabilities with the gradient-drift type. The power spectrum of the irregular edges shows a slope $p_1 = -1.93$ from wavelengths $\lambda = 10$ km to $\lambda \approx 100$ m.

In two articles, Basu et al. (1988, 1990) investigated DE-2 satellite data in order to compare the gradient-drift instability and the Kelvin-Helmholtz instability in the high latitude F-region ionosphere. Their initial sampling resolution was 120 m, but with the help of comb filters (see Basu et al. (1988)), they managed to resolve scale-lengths as short as 10 meters. Using this technique, they obtained slopes $p_1 = 1.8$ when they associated the irregularities with velocity shear flow, and $p_1 = [1.6, -2]$ for the GDI. They also found a steepening for wavelengths shorter than $\lambda = 125$ m, with $p_2 \approx 3$.

Mounir et al. (1991) also used satellite data and computed power spectra of the electron density fluctuations associated with high latitude irregularities. The majority of their spectral indices were between $p_1 = -1.6$ and $p_1 = -1.8$ for wavelengths in the range 10 km to 40 m. At shorter wavelengths, they indicated an apparent steepening of the power spectra to values of the order of 3. This steepening was however weak and not clearly pronounced, maybe due to a poor resolution.

Also using satellite data, Kivanc and Heelis (1997) studied 18 polar cap patches and performed a statistical analysis. They found spectral slopes of $\Delta Ne/Ne$ in the range $[0.33; -4]$, with a strong dominance of $p_1 \in [-1.33; 1.66]$.

The spectral indexes obtained in the previous studies, i.e., $p_1 \approx -1.9$, are in very good agreement with the results found in this work for the low frequency domain. A steepening at high-frequencies also agrees with the plausible steepening noted by Basu et al. (1990) and supported by Mounir et al. (1991).

Conclusively, there is very little evidence for the spectral knee in the high latitude F-region ionosphere. A reason that might explain this is the lower resolution of the previous experiments. Indeed, the unprecedented high sampling rate of 5.8 kHz of the ICI-2 sounding rocket allowed to resolve plasma structures down to meter scales. This hypothesis can be illustrated in Figure 4.26. Figure 4.26 a) shows the electron density fluctuations and the power spectrum of 1/50 of the measurements made by the Langmuir probes during the time interval $t_{of} = [262, 271]$ s. This implies a sampling frequency $F_s = 115.6$ Hz. The spectral index is $p_1 = -1.64 \pm 0.2$ over the entire frequency range. Figure 4.26 b) shows the fluctuations and the power spectrum over the same time interval as in Figure 4.26 a), but sampled at $F_s = 5.8$ kHz. The slopes in the low frequency ranges are similar in both Figure 4.26 a) and Figure 4.26 b) but the steepening only occurs in the case of high sampling rate.

Author	Spacecraft	Altitude (km)	Resolution (m)	p_1	p_2
Dyson et al. (1974)	satellite	$400-1000$	$[70000, 70]$	-1	-
Phelps and Sagalyn (1976)	satellite	$600-3200$	$[10000, 200]$	$[-1.5, -2.5]$	-
Singh et al. (1985)	satellite	300	>160	-1.9	-
Cerisier et al. (1985)	satellite	$400-2000$	$[10000, 50]$	-1.9	-
Basu et al. (1990)	satellite	300 and 900	>120 and >10	$[-1.6, -2]$	$[-3, -3.5]*$
Mounir et al. (1991)	satellite	$450-2000$	$[640, 40]$	$[-1.6, -1.8]$	order of 3
Kivanc and Heelis (1997)	satellite	-	>240	-1.5	-
ICI-2 results (2013)	rocket	$200-330$	>1	-1.8	-3.8

Table 4.2: Previous high latitude ionosphere experiments as well as the ICI-2 results. Due to poor resolution (tens of meter in the best case), the spectral indices found in the literature have to be compared to *our* p_1, corresponding to the intermediate scale range. $*$ Basu et al. (1990) could only resolve structures of 120 meters, but using a series of filters, they managed to extend their resolution down to 10 m. With this technique, they observed dual-slope power spectra with breaking point at about $\lambda_b \approx 125$m. Note that the values given here are indications of the results obtained by the authors. For precise numbers, see the references.

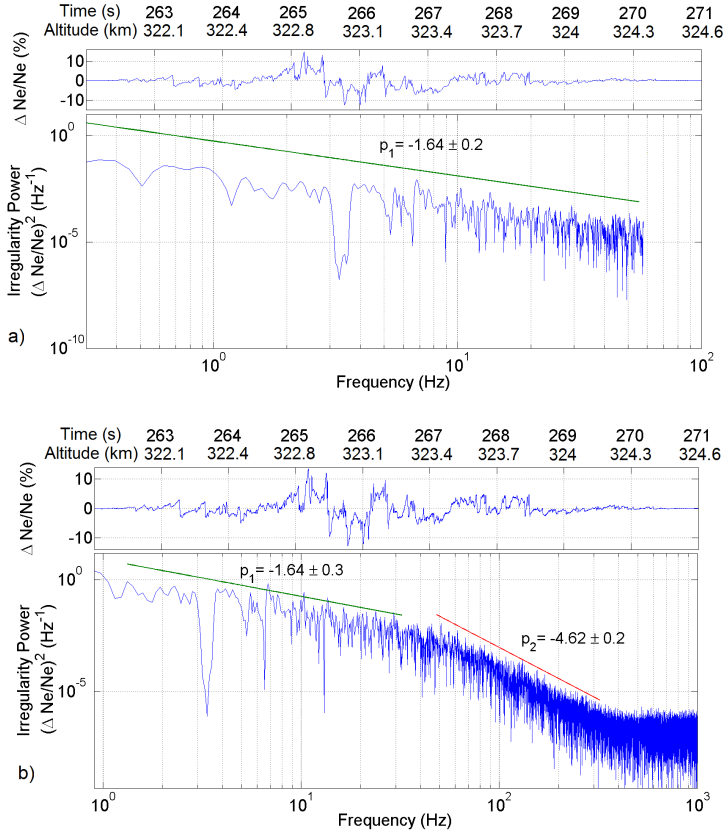

Figure 4.26: a) Power Spectrum of 1/50 of the electron density measurements made by the Langmuir probes between $t_{of} = 262$ s and $t_{of} = 271$ s. This implies a sampling frequency $F_s = 115.7$ Hz. b) Power spectrum for the same time interval, but with the 5.8 kHz sampling rate.

It is worth noticing that spectral knees at large scales have been observed in the high latitude F-region before. For example, Villain et al. (1986), analyzing satellite measurements, found a break at about 800 m in about 25% of their data. Phelps and Sagalyn (1976) also argued that 10% of their measurements would be best fitted by two slopes.

In contrast to the power spectra obtained by high latitude F-region experiments, many evidences exist of dual-slope power spectra in the low latitude ionosphere. Indeed, several rockets and satellites launched to study ionospheric plasma irregularities in the equatorial zone intersected plasma structures exhibiting two slopes (e.g. Kelley et al., 1982; Hysell et al., 1994; Rodrigues et al., 2009). Table 4.3 shows some results obtained in the equatorial region. Different explanations have been proposed. Assuming turbulence theories to be well suited to describe the observed plasma structures, the long wavelengths regime may be due to the RT instability (see section 2.5.1) (Kelley, 2009) and the steepening may be due to drift waves or to diffusion (e.g. LaBelle et al., 1986; Kelley, 2009). There are also arguments against turbulence theories, proposing that the spectral indices are related to the amplitude of the structures and a steepening of the waves Hysell et al. (1994).

Author	**Spacecraft**	**Altitude (km)**	$\mathbf{p_1}$	$\mathbf{p_2}$
Kelley et al. (1982)	rocket	< 600	-2	-5
LaBelle et al. (1986)	rocket	< 700	-2.5	-4.5
Hysell et al. (1994)	rocket	< 500	-2	-5
Jahn and LaBelle (1998a)	rocket	< 822	-1.6	-5
Rodrigues et al. (2009)	satellite	$400 - 853$	-1.6	steepening
ICI-2 results (2013)	rocket	$200 - 330$	-1.8	-3.8

Table 4.3: Previous low latitude ionosphere experiments as well as the ICI-2 results. The wavelengths at which the power spectra steepen is considered to be $\lambda_b \approx 100$ m at low latitudes. Note that the values given here are indications of the results obtained by the authors. For precise numbers, see the references.

4.6.2 Low-frequency range - intermediate-scales

The low-frequency results correspond to wavelengths between several kilometers and about $30-50$ m. They will be discussed here with respect to four macroinstabilities: the Ion-Cyclotron instability (IC), the current-convective instability, the gradient-drift instability and the Kelvin-Helmoltz instability. These particular instabilities have been chosen because they are the most probable candidates for high latitude ionospheric irregularities (see for example, Kintner and Seyler, 1985; Kelley, 2009; Oksavik et al., 2012; Carlson, 2012) and section 2.5.1.

Theoretical work was done in the past in order to calculate the generation of electrostatic ion cyclotron waves by field-aligned current (FAC) (Kelley, 2009), which can be a source of free energy available for the production of irregularities (see section 2.3.2 for more flatter about FAC). When the waves generated by the FAC drive the plasma unstable, this mechanism is termed Ion-Cyclotron instability. The IC instability has had some experimental evidence in the high latitude ionosphere, especially at high altitudes (e.g. Kintner et al., 1978). At lower altitudes, Walker et al. (1991) studied enhanced density fluctuations associated with arc formation and also argued that the IC was the most likely source mechanism for their measured irregularities.

The current densities required for the IC instability are higher than the average FAC observed in the ionosphere (Kelley, 2009). IC instabilities should thus be rare and may be restricted to

the edges of auroral arcs which are often associated with strong FAC and/or regions with intense shear flows (Kelley, 2009). For the ICI-2 flight, no values of the FAC were available. However, the electron precipitations were mostly diffuse, with low energies (about 200 eV) and only present in small parts of the flight. Therefore, we may assume that the rocket did not fly through a region with strong FAC. In this regard, the IC instability is probably not the dominant mechanism responsible for the observed irregularities. Another argument against the IC instability is that the spectra computed from the ICI-2 data did not exhibit any peaks nor enhancements at the ion cyclotron frequency (and/or its harmonics), as it could be expected for the IC instability (Treumann and Baumjohann, 1997).

As noted in section 2.5.1, the CC instability also requires currents flowing along the magnetic field lines. Thus, without the FAC values, one cannot completely rule out this mechanism. However, it is presumably not a dominant process occurring during the ICI-2 flight because the diffuse auroral particle precipitation that may have the ability to trigger the CC instability (Ossakow and Chaturvedi, 1979) was only encountered close to apogee and at the end of the flight. By comparing panels a) and b) in Figure 4.27 (see section 4.3.1 for a complete description of the figure), one can see that electron precipitations and strong fluctuations in the electron density only coincide for the beam F3. Moen et al. (2012) also argued that only F3 was collocated with decameter-scale irregularities. Since most of the inverted V, F1, F2 and F4 had no major influence on the small-scales irregularities, it is less likely that the beam F3 had a preponderant influence on them either. In addition, the CC instability is usually not believed to be a dominant mechanism at altitudes close to the F-peak, as it has a preferential tendency to create unstable conditions for low plasma densities (e.g. Tsunoda, 1988; Kelley, 2009).

The most striking feature of Figure 4.27 a) is the difference in fluctuations between the leading edge (at $t_{of} \approx 388\,\mathrm{s}$) and the trailing edge (at $t_{of} \approx 430\,\mathrm{s}$) of the density enhancement: the trailing gradient exhibits very strong fluctuations. This preferred direction of irregularities was observed in previous experiments and was claimed to be a supporting evidence for the gradient-drift instability (e.g. Cerisier et al., 1985; Basu et al., 1990; Mounir et al., 1991). Referring to section 2.5.1, the GDI is unstable when the $\mathbf{E} \times \mathbf{B}$-polarization drift is along the preexisting density gradient. Thus, when IMF $B_z < 0$, the trailing edge of a plasma patch (or a density enhancement) moved by the ionospheric convection pattern should be unstable. Note, however, that this property can be altered due to zonal flows (Gondarenko and Guzdar, 2004). Recalling the assumption from section 4.2 stating that the negative gradients measured by the ICI-2 rocket correspond to the trailing edges of the plasma structures, the GDI should be unstable on these negative gradients.

The strong irregularities observed at $t_{of} \approx 430\,\mathrm{s}$ in Figure 4.27 are located in both the region with particle precipitation and on the gradient with favorable disposition to the GDI. Tsunoda (1988) argued that in order to have a maximum growth rate of the CC process in a system comprising both the GDI and the CC instability, the magnitude of the slip velocity v_0 (the magnitude of the $\mathbf{E} \times \mathbf{B}$-velocity relative to the neutrals), and the magnitude of the velocity along $\mathbf{B}$ should be comparable, i.e. $v_0 \approx ||\mathbf{v}_{\parallel}||$. He concluded that for typical dayside ionospheric conditions (with FAC values $||\mathbf{j}_{\parallel}|| \sim 1\,\mu\mathrm{A/m}^2$), the electron density in the F region was typically 100 times higher than the value required for a maximum growth rate of the CC instability. In this sense, the GDI is more likely to create the irregularities.

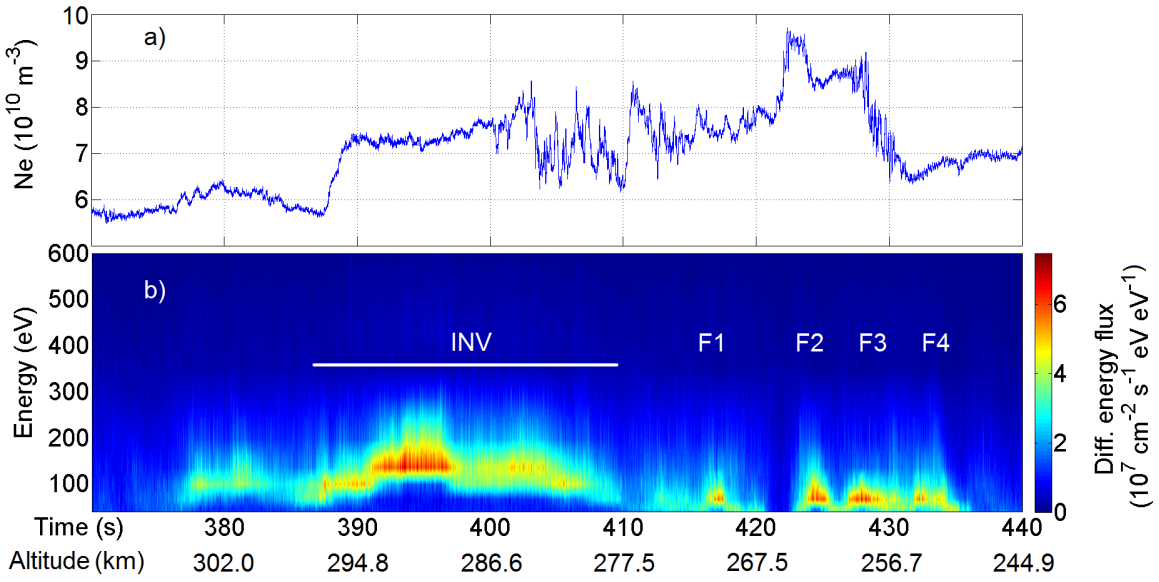

Figure 4.27: a) Electron density enhancement between $t_{of} = 370\,\mathrm{s}$ and $t_{of} = 440\,\mathrm{s}$ of flight. b) $0 - 30°$pitch angle low energetic particle (LEP) precipitating electron flux.

By analyzing the entire flight (see Figure 4.15) one can observe that the strong fluctuations and the double slope power spectra are often collocated with density gradients. This feature is even more prominent when comparing panel a) and panel b) in Figure 4.28, showing the RMS value of 2 seconds intervals of density fluctuations and the density gradients, respectively. The correlation between density fluctuations above the 2 % threshold and density gradients is evident. Especially, there is a clear correspondence between the strong fluctuations and the negative density gradients, as emphasized by the arrows. In fact, most of the strong perturbations match a negative density gradients, which strongly suggests the GDI as a source mechanism.

Another argument in favor of the GDI is in the spectral indices associated with the strong density fluctuations. The average slope of these power spectra being $\bar{p}_1 = -1.79$, it agrees well with both theoretical predictions and previous in-situ experiments: a slope $p_1 = -5/3$ is expected from the fluid description of the GDI (see Table 2.1) and previous high-latitude studies of the GDI obtained $p_1 \in [-1.6, -2]$ (Cerisier et al., 1985; Basu et al., 1990; Mounir et al., 1991). Numerical simulations performed by Gondarenko and Guzdar (2004, 2006) to simulate plasma patches in the high latitude ionosphere also exhibited slopes close to $p = -1.6$. In addition, the theory of Sudan and Keskinen (1984) states that both the RT instability and the GDI should exhibit the same power spectral indices in the low-frequency range, as their dynamics are similar. Most of the F-region equatorial irregularities at intermediate-scales have been attributed to the RT instability Kelley (2009), which exhibits slopes $p_1 \approx -2$, similar to the one obtained in this thesis (see again Table 4.3).

In addition, Oksavik et al. (2012) calculated the time-scale for GDI irregularity growth ($\tau_{GDI} = \gamma_{GDI}^{-1}$) for the entire ICI-2 flight and argued that this instability was likely a dominant mechanism for the decameter-scale irregularities.

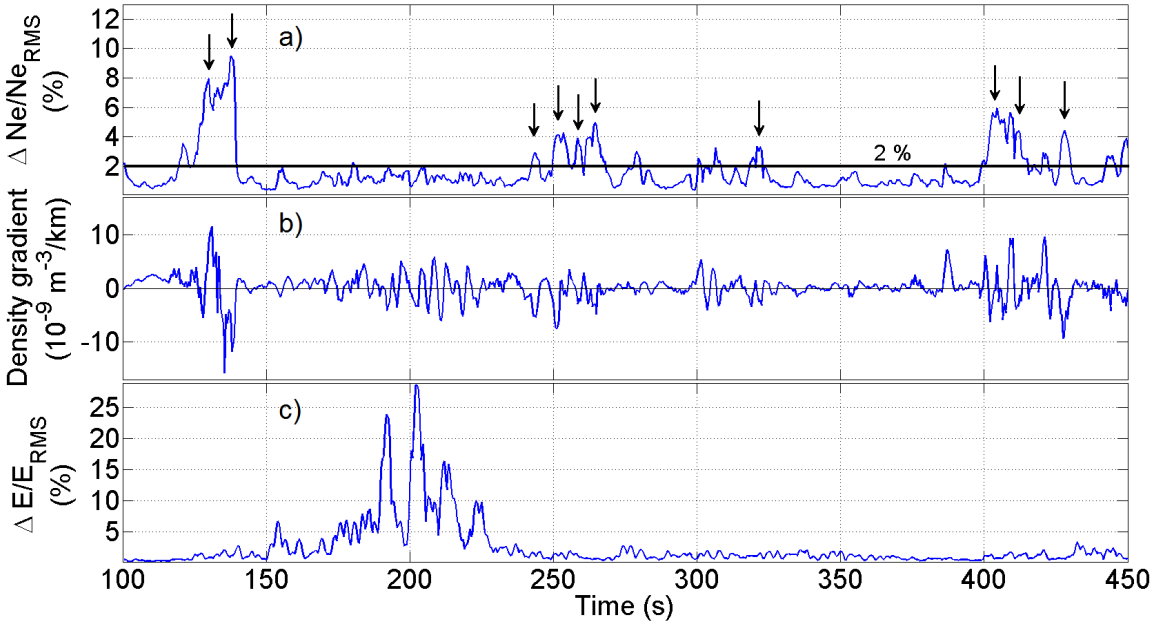

Figure 4.28: a) RMS values of 2 seconds intervals of the electron density fluctuations. The intervals are computed every 0.5 seconds. The vertical arrows emphasize the correlation between density fluctuations above 2 % and negative density gradients. b) Density gradients for the same intervals. c) RMS values of 4 seconds intervals of the electric field fluctuations. The intervals are computed every second.

The last macroinstability considered here is the KH, which requires velocity shears transverse to the magnetic field (see section 2.5.1). In the electrostatic approximation, velocity fluctuations (and shears) are closely related to the electric field fluctuations (Kintner and Seyler, 1985). The RMS electric field fluctuations for 4 seconds intervals are shown in Figure 4.28 c). They are very small ($\sim$ 1 %) during the entire flight, except between $t_{of} \approx 150$ s and $t_{of} \approx 230$ s. This time interval corresponds to the waveform seen in the electron density and in the electric field data described in sections 4.2 and 4.5. It is likely due to a VLF wave and not to turbulences/irregularities. Hence, according to Figure 4.28 c), little velocity shear processes are expected during the ICI-2 flight.

The growth rate of the KH instability given in section 2.5.1 is also proportional to the electric field fluctuations. By looking at Figure 4.28 c), one can argue that the values of the growth rate given by Eq. (2.57) are small throughout the ICI-2 flight, except in the region of the wave pattern. Oksavik et al. (2012) calculated γ_{KH} during the entire ICI-2 flight and concluded that the KH instability was too slow compared to the GDI to explain the decameter-scale irregularities observed.

In the view of above, the results suggest the gradient drift instability as a dominant source mechanism. Using only the absolute electron density measured by a single rocket as viable quantity, we cannot completely rule out other processes (or a superposition of processes) and neither determine the spatio-temporal evolution of the structures. Therefore, a question remains open, that is, whether one of the GDI-spectral theories cited in section 2.5.2, i.e. turbulence or coherent steepening theory, is adequate to explain the irregularities.

Consecutive and/or simultaneous measurements may allow to determine whether the observed structures are quasi-stationary, turbulent or due to coherent coupling. It may also be possible

to distinguish between coherent structures and random/turbulent structures by applying a bispectral analysis to the data, as done in LaBelle and Lund (1992). This is however beyond the scope of this work and is left for future study.

4.6.3 High frequency range - small-scales

As described in section 4.6.1, little research has been performed on the spectral analysis of the electron density fluctuations associated with small-scales high latitude F-region irregularities. In the equatorial regions, mainly two processes have been proposed for the steepening of the power spectra observed: drift-waves (e.g. Kelley et al., 1982; LaBelle et al., 1986) and diffusion perpendicular to the magnetic field (e.g. Kelley, 2009; Hysell et al., 1994). These two mechanisms are discussed here with regard to the data obtained from ICI-2.

Drift waves can be driven on abrupt gradients and can act as a secondary process (Similon and Sudan, 1990) feeding on an initial instability. From theoretical arguments, the slopes of the power spectra associated with DW are either $p_2 = -5$ or $p_2 = -11/3$, for the direct and inverse cascade, respectively (see Table 2.1 in section 2.5.2). Due to these steep slopes, DW have been used to explain the steepening of the power spectra in equatorial regions (e.g. LaBelle et al., 1986). For the power spectra obtained from ICI-2 data, the slopes in the high-frequency range were usually closer to $p_2 = -4$, which is shallower than the value expected for the direct DW cascade and slightly steeper than for the inverse cascade value.

It was shown that for irregularities in the equatorial zone at F-region altitudes, the gradient scale-size L (see section 2.5.1) should be smaller than 100 m for the generation of ~ 3 m irregularities by the DW process (Huba and Ossakow, 1979). In the case of the ICI-2 flight, the observed gradients appeared rather weak, with typical values $L \approx [5000, 10000]$ m. In this regard, the DW seems unlikely to have directly generated the observed small-scale irregularities. However, the theory of Huba and Ossakow (1979) is based on equatorial conditions and should be reconsidered for high latitude plasma regions, where the phenomena depicted in section 2.3.1 comprising for example particle precipitation, FAC, conductivities and large-scale electric fields are present and different from the low latitude regions (an extensive description of the dynamics at low latitudes can be found in Kelley (2009)).

Kelley et al. (2002) argued that the DW mechanisms needed not to be invoked to explain the steepening observed for equatorial irregularities, but that diffusion could be adequate.

The lifetime of horizontal structures in the high-latitude ionosphere depends on the diffusion across the magnetic field (Kelley et al., 1982). Kelley (2009) argued that the stability of a plasma at a given k depends on whether some positive contribution to the growth rate of an instability exceeds diffusive damping due to terms of the form $-k^2 D_\perp$, where $D_\perp$ is the diffusion coefficient $\perp \mathbf{B}$. Vickrey and Kelley (1982) calculated the expected diffusion coefficients for the F-region depending on the conductivity of the E-layer, which can be increased for example by particle precipitation or direct solar radiation. They argued that the typical values increase from roughly $1\,\mathrm{m}^2/\mathrm{s}$ to more than $10\,\mathrm{m}^2/\mathrm{s}$ as the E-region conductivity increases (as the ratio Σ_p^E/Σ_p^F increases. See section 2.3.2 for the altitude variations of the conductivity in the high latitude ionosphere).

Considering the diffusion process, the linear growth rate of the GDI given in section 2.5.1 becomes

$$\gamma_{GDI} = \frac{E_0'}{BL} - k^2 D_\perp, \tag{4.1}$$

where E_0'/B is the component of $\mathbf{E}' \times \mathbf{B}/B^2$ parallel to ∇n. From Eq. 4.1, one can find the critical wavelength λ_{cr} at which diffusion balances the irregularity growth, i.e.

$$\lambda_{cr} = 2\pi \left(\frac{E_0'}{BL} \frac{1}{D_\perp} \right)^{-1/2} . \tag{4.2}$$

Using $L = 12000\,\mathrm{m}$, $E_0'/B = 990\,\mathrm{m/s}$ (values corresponding to the gradient at $t_{of} \approx 430\,\mathrm{s}$, see Figure 4.28) and $D_\perp = 1\,\mathrm{m}^2/\mathrm{s}$, which is on the small side, one gets $\lambda_{cr} \approx 22\,\mathrm{m}$. Note that a larger $D_\perp$ would make the value λ_{cr} larger. In addition, since the velocity of the neutral is not known, the approximation $E_0' \approx E_0$ had to be made. Assuming a velocity of the neutrals which is 60 % of the ion drift speed, the critical wavelength would increase to $\lambda_{cr} \approx 30\,\mathrm{m}$.

Thus, in the example above, a positive instability growth occurs for all wavelengths greater than $\lambda_{cr} \approx 22\,\mathrm{m}$. Unless some additional instability process emerges at small-scales, the only way waves with $\lambda \leq 10\,\mathrm{m}$ can arise is through a cascade of structures from large-scales to small-scales.

An estimation of λ_{cr} with $D_\perp = 1\,\mathrm{m}^2/\mathrm{s}$ during the entire ICI-2 flight can be seen in Figure 4.29. For comparison, Figure 4.29 also shows the length-scales at which the spectral knees occur, λ_{sb}. The errorbars on λ_{sb} are calculated assuming that the actual spectral knees are contained in a frequency range of about $\pm 5\,\mathrm{Hz}$ with respect to the values f_{sb}. It is interesting to notice that λ_{cr} and λ_{sb} match fairly well, except for some values that are completely off scale (e.g. at $t_{of} \approx 405\,\mathrm{s}$). At the end of the flight, the critical wavelengths λ_{cr} are generally smaller than the spectral knees. This might be explained by the fixed $D_\perp = 1\,\mathrm{m}^2/\mathrm{s}$ chosen for the entire flight: particle precipitation occurred from approximatively $t_{of} = 380\,\mathrm{s}$, which might have resulted in an increase of $D_\perp$, as argued by Vickrey and Kelley (1982), and thus an increase in the actual critical wavelengths.

In this regard, diffusion could explain the steepening of the power spectra observed during the ICI-2 flight. However, the critical wavelengths shown in Figure 4.29 are dependent, among others, on the value $D_\perp$. Using the value given by (Kelley et al., 2002), i.e. $D_\perp = 0.125\,\mathrm{m}^2/\mathrm{s}$, the critical wavelengths due to classical diffusion would be much smaller ($\approx 1/3$ of the values shown in Figure 4.29).

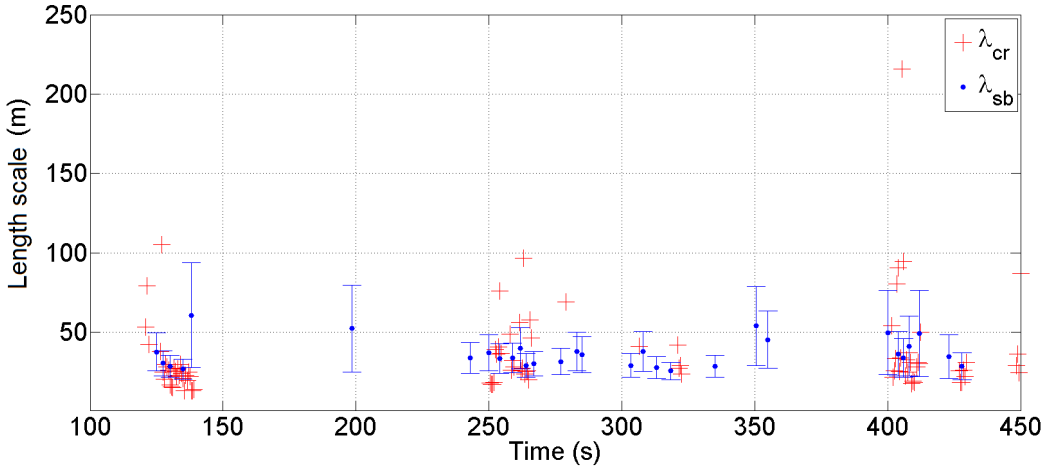

Figure 4.29: Figure displaying the critical wavelength λ_{cr} at which diffusion balances the irregularity growth (red) and the wavelengths λ_{bs} at which the spectra steepen (blue).

A suitable way to investigate the decay of the plasma structures would be using successive measurements of the same structure, for example with two consecutive rockets or satellites. This was done in the equatorial regions, were Hysell and Kelley (1997) computed the fluctuation spectra for several plasma bubbles observed on consecutive satellite orbits. Using this technique, they could estimate the decay of the plasma structures and they argued that a diffusive damping would occur via three-wave interactions in the range $1\,\mathrm{m} < \lambda < 100\,\mathrm{m}$.

For the ICI-2 flight, the spectral knees were measured in the range of f_{O_+}, the O_+ gyrofrequency. For phenomena occurring at frequencies higher than the f_{O_+}, corresponding to small-scales, the motion and the coupling between electrons and ions cannot be described by a fluid description anymore (Baumjohann and Treumann, 1996) and kinetic effects should be taken into account. Nevertheless, it is difficult to draw any firm conclusion about the relation between the ion gyrofrequency and the observed frequencies (and about the transformation from frequencies to scales) because the data include various contributions from Doppler-shift effects due to the motion of the rocket and the plasma drifts. Again, consecutive and/or simultaneous measurements would allow to resolve the temporal evolution of plasma structures and therefore, give further indications on the physical phenomena. In-situ measurements of the ion and electron temperatures would also provide valuable flatter and allow one to calculate precise values for the gyroradii of ions and electrons.

4.6.4 Summary and concluding remarks

Despite their crucial importance for mitigation/circumvention of consequences on communication and navigation systems, small-scales high-latitude irregularities in the F-region ionosphere are still poorly understood. Research in this area has not progressed as fast as in the equatorial regions, as it is geometrically impossible for high-latitude ground based radars to obtain an appropriate backscatter angle at F-regions using VHF and UHF systems (Kelley, 2009), and as the resolution of HF systems is usually too coarse. Therefore, the only possibility to study in depth and characterize these small-scales irregularities is by means of in-situ experiments.

In this regard, the Investigation of Cusp Irregularities 2 (ICI-2) sounding rocket was launched from Ny-Ålesund, Svalbard, Norway (78.9° N, 11.9° E geographic coordinates) at 1035 Universal Time (UT) on the 5th of December 2008. The main objectives were to resolve the irregularity structures at meter-scales and to quantify the gradient drift instability process.

In this study, power spectral analysis was performed on the electron density fluctuation data using the windowed FFT as a main technique and the Morlet wavelet transforms as a secondary approach. This was done in order to compare two different techniques and test the results obtained by the windowed FFT. Power laws at various segments of cusp/polar cap activities associated with different plasma structures such as particle precipitations or density gradients were computed and compared. The power spectra of the strong density fluctuations measured during the ICI-2 flight exhibit a characteristic dual-slope power law behavior with a spectral knee at frequencies in the range $f_{sb} \in [20, 55]\,\mathrm{Hz}$, corresponding to wavelengths $\lambda_{sb} \in [25, 60]\,\mathrm{m}$. The average spectral indices are $\bar{p}_1 = -1.8$ below approximatively 30 Hz and $\bar{p}_2 = -4$ at frequencies above 40 Hz. The dual-slope characteristic was obtained using both the Fourier and the wavelet techniques, providing a good confidence in the results.

Few previous experiments were dedicated to the spectral analysis of plasma density at F-region altitudes in the high latitude ionosphere, and even fewer managed to resolve structures at decameter-scales. Consequently, limited literature is available concerning the spectral indices obtained at high-latitude for these small scales, especially concerning the dual-slope power

spectra. Nevertheless, the slopes obtained from the ICI-2 data in the low-frequency range (below $\sim 30\,\mathrm{Hz}$) match well earlier satellite observations, which mainly obtained $p_1 \in [-1.5, 2]$ (see Table 4.2). A plausible steepening of the power spectra at higher frequencies has also been indicated in previous high-latitude studies (e.g. Villain et al., 1986; Basu et al., 1990; Mounir et al., 1991) with a spectral break occurring between 800 m and 40 m. However, the dual-slope characteristic feature has mostly been described in the equatorial regions, where more research has been directed towards the spectral analysis of rocket data.

Four macroinstability mechanisms were considered with a view towards determining the most likely candidate for the observed low-frequency irregularities: the ion-cyclotron, the current-convective, the Kelvin-Helmoltz and the gradient-drift instabilities. As most of the strong density irregularities observed by the ICI-2 sounding rocket were collocated with gradients in the plasma, the results suggest the gradient drift instability as a dominant source mechanism. As no viable magnetic and electric field data were available in the entire frequency range of interest at the time of writing, we cannot completely rule out other processes. Future work on the AC electric field data may provide additional flatter to confirm the results.

Several hypotheses have also been proposed and discussed for the steepening of the power spectra observed by the ICI-2 rocket: drift-waves, diffusion processes and damping due to kinetic effects. Drift-wave processes seem unlikely to have directly produced the observed irregularities because the density gradients were rather weak. Nevertheless, both diffusion mechanisms and kinetic effects may explain the steepening, and should therefore be further analyzed in future work.

We have pointed out the need for consecutive and/or simultaneous measurements in order to investigate accurately the spatio-temporal evolution of the irregularities and the decay of the plasma structures. Indeed, successive measurement may allow to determine whether these irregular structures are quasi-stationary, turbulent or due to coherent coupling of waves, as well as assess the role of diffusion or damping due to kinetic effects.

4.7 Outlook

As previously mentioned, further work should be performed in order to characterize the power spectra associated with high latitude, small-scales F-region irregularities. We divide them in three categories: future work on ICI-2, other rocket experiments, theoretical background.

- *Future work on ICI-2*: As mentioned in section 4.5, only the DC electric field data were available at the time of writing. The frequency range was too narrow to study the power spectra in the same way as for the electron density. However, it may be possible to obtain more information concerning the high-frequency components of the electric field by combining the DC and the AC data, allowing a suitable spectral analysis.

  We also argued in section 2.5.2, that two theories exist concerning the slopes of the power spectra: one assumes scaling laws and turbulences while the other assumes coherent wave steepening. A technique called bispectral analysis could be performed on the electron density data in order to see whether coherent structures are present in the density fluctuations.

- *Spectral analysis of measurements made by other rockets*: In addition to the ICI-2 sounding rocket, several other rockets were launched or are planned for the future. The ICI-3 sounding rocket was launched from Ny-Ålesund at 0721 UT on the third of December

2011 and intersected a region with flow shears. A thorough power spectral analysis could be done in order to see whether the slopes are different to the ones obtained for ICI-2. Note that preliminary results seem to indicate the presence of dual-slope power spectra throughout the entire ICI-3 flight, with slopes in the same range as for the ICI-2 rocket.

Also, rockets such as the MICA rocket, launched from the Poker Flat research range, Alaska, on February 19. 2012, and the ICI-4, that will be launched by the end of 2013, would provide additional information concerning irregular structures in the high-latitude ionosphere. As mentioned previously, a particular need for consecutive and/or simultaneous measurements is desired in order to study the decay of irregularities. In this regard, the ICI-5 sounding rocket is planned to be launched with daughter payloads, allowing to resolve the spatio-temporal evolution of plasma structures.

- *Theoretical/modeling approach*: In order to understand the complex, multi-scale phenomena occurring in the polar caps/cusps, advanced plasma models are needed. Numerical and theoretical modeling of plasma patches/enhancements including also kinetic instabilities may provide precious information on different irregularity mechanisms and decay processes. However, this was beyond the scope of this thesis and should be considered in the future.

Appendix

Codes

As the number of pages is already considerable, only a brief version of the central part of the code is given here, that is, the one made for computing the power spectra. The other codes written for this thesis are given in a separate CD-rom. The codes can also be found on the web at the address: *http : //tid.uio.no/plasma/ici_powerspectra/*. For the latter a *username* and *password* are required. These can be obtained by sending me an e-mail at *andres.spicher@gmail.com*.

In order to run the code calculating the power spectra, i.e. `ICI2_PowerSpectra.m`, the following codes must be executed in the right order (once the other codes have be run one time, `ICI2_PowerSpectra.m` can be used alone) :

1. `ICI2_Datas_interpol.m`: Extracts the 4-NLP data and removes the NANs.
2. `ICI2_filter.m`: Filters the spin and some of the harmonics.
3. `ICI2_Altitude.m`: Determines the altitude of the rocket.
4. `ICI2_Ne.m`: Calculates the electron density.
5. `ICI2_Efilter.m`: Filters the electric field data.
6. `ICI2_Efield.m`: Computes the electric field directions
7. `ICI2_PowerSpectra.m`: Computes the power spectra.

The last code cited above is the following:

Listing: ICI2_PowerSpectra.m

```
clear; close all;
%%-------------------------------------------------------------------------
%% File made to compute the power spectra from the ICI2_Ne.mat file
%% and using the E-field to calculate the relative ExB-velocity.
%% Andres Spicher, 28.05.2013, Oslo
%%-------------------------------------------------------------------------

%% Load the folders
load('ICI2_Ne.mat'); % Loads the Electron density file
load ICI2_ELast.mat; % Loads the Electric field file

%% Frequency of sampling of the ICI-2 rocket
Fs=2*2893.5;

%% Graph and number settings
format long
set(0,'defaultfigurerenderer','zbuffer','defaultlinemarkersize',.01);

%% Electron density between t1 and t2
t1=ceil(100*Fs);
```

```
t2=ceil(450*Fs);
t1_vec= find(time_noNans==t1);
t2_vec= find(time_noNans==t2);

%% Calculate the relative velocity using the electric field datas
v_rel_in = interp1(tl , normrExBned , nlpTimeSec);

%% ------------------ POWER SPECTRA ------------------
for i=1:1

%% Select the time interval for the spectrum
ta=426+1*i; % Time in sec. at which we want to start the spectrum
ta_noNans= ceil(ta*Fs); % Equivalent of ta in time-steps
ta_vec= find(time_noNans==ta_noNans); % Position in the time_noNans vector
t_add=2; % Select the end-time of the spectrum (ex: 2 sec)
tb_vec= ta_vec+1*ceil(Fs*t_add);
tb=time_noNans(tb_vec)/Fs;
longueur = length(time_noNans(ta_vec:tb_vec)); % Length of the interval

%% Removing the trends
L=2*ceil(longueur*0.1/2); % Lenght added to the window
values = csaps(time_noNans(ta_vec:tb_vec),Ne(ta_vec:tb_vec),1e-14, time_noNans(ta_vec:
    tb_vec) ); % Spline for detrending
window = hanning(longueur+L); % Hanning window
window(1:L/2)=[];
window(end-L/2+1:end)=[];

% Ratio version
Ne_selected=Ne(ta_vec:tb_vec); % Selection of the Ne interval.
Ne_rel = Ne_selected./values'-1; % We use the normalized value -> the ratio between the
    density and its mean
Ne_fluct = (Ne_rel.*window'); % Use the window on the data

%% Calcul of different values
Ne_av_fluct(i)=rms(Ne_rel)*100; % Calcul of the RMS fluctuations
v_rel=mean(v_rel_in(ta_vec:tb_vec)); % Calcul of the mean v_rel

%% ------------------ FFT-algorithm ------------------
nfft = 2^(nextpow2(longueur)); % Use for the FFT algorithm
delta_t=1/Fs; % Time interval between two samples
m=nfft/2; % We just need the half of the samples, because of symmetry
fc=1/(2*delta_t); % Nyquist freq.
freq= Fs*(0:m)/nfft; % Frequency vector
Ne_fft=fft(Ne_fluct,nfft); % Applies the FFT on nfft interval bins
Power_Ne_fft=Ne_fft.*conj(Ne_fft)/nfft; % Computes the power and normalizes it
Power_Ne_fft(m+2:nfft)=[]; % Removes half of the values
Power_Ne_fft(2:m+1)=2*Power_Ne_fft(2:m+1); % Muliplies by two to get the right power

%% Taking the logs of everything
logfreq= log(freq(2:end));
logPower= log(Power_Ne_fft(2:end));

%% Select the intervals for the automatized fitting
[minvalLow1    fLoow1] = min(abs(freq-1.7)); % Lowest freq.
[minvalLow2    fLoow2] = min(abs(freq-(26))); % End of low freq. range
[minvalhigh1    fhigh1] = min(abs(freq-(40))); % Beginning of high freq. range
[minvalhigh2    fhigh2] = min(abs(freq-190)); % Noise level

% Take the log of the values (for fitting)
logfreq_fit= logfreq(fLoow1:fLoow2);
logfreq_fit=logfreq_fit(:);
logPower_fit=logPower(fLoow1:fLoow2);
logPower_fit=logPower_fit(:);
logfreq_fit1= logfreq(fhigh1:fhigh2);
logfreq_fit1=logfreq_fit1(:);
logPower_fit1=logPower(fhigh1:fhigh2);
```

```
logPower_fit1=logPower_fit1(:);

%% Calculation of the gradients
dens_chang=(Ne(tb_vec)-Ne(ta_vec)); % Change in density between t2 and t1
dx=v_rel*t_add/1000; % Distance in km
grad(i)=dens_chang/dx; % Gradient

%% ---------------- FITS ----------------

%% Part made to calculate the double slope authomatically
if Ne_av_fluct(i)>=2  % If fluct equal or above 2 %

% Fit for the low freq. part of the spectrum
p= polyfit(logfreq_fit,logPower_fit,1);
d(i)=p(1); % slope p1
[f gof] = fit(logfreq_fit,logPower_fit,'poly1');
fit_val = feval(f,logfreq_fit);
exp_fit_val=exp(fit_val);

% Fit for the high freq. part of the spectrum
p1= polyfit(logfreq_fit1,logPower_fit1,1);
d1(i)=p1(1); % slope p2
[f1 gof1] = fit(logfreq_fit1,logPower_fit1,'poly1');
fit_val1 = feval(f1,logfreq_fit1);
exp_fit_val1=exp(fit_val1);

else  % put NaNs where Ne_fluc < 2% (for plotting purpose)
d(i)=NaN;
d1(i)=NaN;
end

%% ---------------- FIGURES ----------------
% Figure for the electron density fluctuations
% figure;
% plot(time_noNans(ta_vec:tb_vec)/Fs,Ne_fluct*100,'-b');
% xlabel('Time (s)','FontSize',30);
% ylabel('\Delta Ne/Ne (%)','FontSize',30);
% set(gca,'FontSize',30)
% grid on;
%
%% Figure for the Power Spectrum
% figure;
% loglog(freq, Power_Ne_fft,'-b')
% hold on;
% loglog(exp(logfreq_fit),exp_fit_val,'-g')
% loglog(exp(logfreq_fit1),exp_fit_val1,'-r')
% xlabel('Frequency (Hz)','FontSize',30);
% ylabel('Irregularity Power (\Delta Ne/Ne)^2 (Hz^{-1})','FontSize',30);
% set(gca,'FontSize',30)
% grid on
% axis([0.1 1000  0.0000000001 20])
end
```

In addition, the following codes were also used:

- `ICI2_ManualSlopes.m`: Used to compute the slopes and spectral knees with the manual method.
- `ICI2_EFourierAnalysis.m`: Used for the Fourier analysis of the electric field fluctuations.
- `ICI2_NeWavelet.m`: Used to create the wavelet spectrograms and power spectra
- `morlet.m`: Morlet wavelet function, implemented by Torrence and Compo (1998).

Bibliography

Akasofu, S. I. and S. Chapman (1972). *Solar-Terrestrial Physics*. London: Oxford University Press.

Anderson, D. N., J. Buchau, and R. A. Heelis (1988). Origin of density enhancements in the winter polar cap ionosphere. *Radio Science 23*(4), 513–519.

Axford, W. I. and C. O. Hines (1961). A unifying theory of high-latitude geophysical phenomena and geomagnetic storms. *Canadian Journal of Physics 39*(10), 1433–1464.

Barth, V. L. (2009). *Identification and tracking of extreme electron densities by EISCAT Svalbard radar and SuperDARN, Master's thesis*. Department of Physics, The University of Oslo, Oslo.

Basu, S., S. Basu, E. Mackenzie, W. R. Coley, J. R. Sharber, and W. R. Hoegy (1990). Plasma Structuring by the Gradient Drift Instability at High-Latitudes and Comparison with Velocity Shear Driven Processes. *Journal of Geophysical Research-Space Physics 95*(A6), 7799–7818.

Basu, S., S. Basu, E. Mackenzie, P. F. Fougere, W. R. Coley, N. C. Maynard, J. D. Winningham, M. Sugiura, W. B. Hanson, and W. R. Hoegy (1988). Simultaneous Density and Electric Field Fluctuation Spectra Associated With Velocity Shears in the Auroral Oval. *Journal of Geophysical Research-Space Physics 93*(A1), 115–136.

Batchelor, G. K. (1969). Computation of the energy spectrum in homogeneous two-dimensional turbulence. *Physics of Fluids 12*(12), II–233.

Batchelor, G. K. (2000). *An Introduction to Fluid Dynamics*. Cambridge: Cambridge University Press.

Baumjohann, W. and R. A. Treumann (1996). *Basic Space Plasma Physics*. London: Imperial College Press.

Bekkeng, T. A., K. S. Jacobsen, J. K. Bekkeng, A. Pedersen, T. Lindem, J.-P. Lebreton, and J. I. Moen (2010). Design of a Multi-Needle Langmuir Probe System. *Measurement Science & Technology 21*(8), 085903.

Bloomfield, P. (2000). *Fourier Analysis of Time Series An Introduction Second Edition*. New York: John Wiley and Sons.

Cairns, R. A. (1985). *Plasma Physics*. Glasgow: Blackie Academic and Professional.

Carlson, H. C. (1994). The Dark Polar Ionosphere - Progress and Future Challenges. *Radio Science 29*(1), 157–165.

Carlson, H. C. (2012). Sharpening our thinking about polar cap ionospheric patch morphology, research, and mitigation techniques. *Radio Science 47*, RS0L21.

Carlson, H. C., J. Moen, K. Oksavik, C. P. Nielsen, I. W. McCrea, T. R. Pedersen, and P. Gallop (2006). Direct observations of injection events of subauroral plasma into the polar cap. *Geophysical Research Letters 33*(5), L05103.

Carlson, H. C., K. Oksavik, and J. Moen (2008). On a new process for cusp irregularity production. *Annales Geophysicae 26*(9), 2871–2885.

Carlson, H. C., T. Pedersen, S. Basu, M. Keskinen, and J. Moen (2007). Case for a new process, not mechanism, for cusp irregularity production. *Journal of Geophysical Research-Space Physics* (A11), A11304.

Carlson, J. H. G. and A. Egeland (1995). Aurora and Auroral Ionosphere. In Margaret G. Kivelson and Christopher T. Russel (Ed.), *Introduction to Space Physics*. New York: Cambridge University Press.

Cerisier, J. C., J. J. Berthelier, and C. Beghin (1985). Unstable Density Gradients in the High-Latitude Ionosphere. *Radio Science 20*(4), 755–761.

Champagne, F. H. (1978). The fine-scale structure of the turbulent velocity field. *Journal of Fluid Mechanics 86*, 67–108.

Chaturvedi, P. K. and S. L. Ossakow (1977). Nonlinear theory of the collisional rayleigh-taylor instability in equatorial spread f. *Geophysical Research Letters 4*(12), 558–560.

Chisham, G., M. P. Freeman, I. J. Coleman, M. Pinnock, M. R. Hairston, M. Lester, and G. Sofko (2004). Measuring the Dayside Reconnection Rate During an Interval of Due Northward Interplanetary Magnetic Field. *Annales Geophysicae 22*(12), 4243–4258.

Chisham, G., M. Lester, S. E. Milan, M. P. Freeman, W. A. Bristow, A. Grocott, K. A. McWilliams, J. M. Ruohoniemi, T. K. Yeoman, P. L. Dyson, R. A. Greenwald, T. Kikuchi, M. Pinnock, J. P. S. Rash, N. Sato, G. J. Sofko, J.-P. Villain, and A. D. M. Walker (2007). A decade of the Super Dual Auroral Radar Network (SuperDARN): scientific achievements, new techniques and future directions. *Surveys in Geophysics 28*(1), 33–109.

Cowley, S. W. H. (2000). Magnetosphere-ionosphere interactions: A tutorial review. In Ohtani, S. and Fujii, R. and Hesse, M. and Lysak, R. L. (Ed.), *Magnetospheric Current Systems*, Volume 118 of *Geophysical Monograph Series*, pp. 91–106.

Crooker, N. U. (1992). Reverse Convection. *Journal of Geophysical Research-Space Physics 97*(A12), 19363–19372.

Crowley, G. (1996). *Critical Review of Ionospheric Patches and Blobs*. In Sonte, W. R. (Ed.), Review of Radio Science 1992-1996, Oxford: Oxford University Press.

Daubechies, I. (1992). *Ten Lectures on Wavelets*. Philadelphia: Society for Industrial and Applied Mathematics.

Davidson, P. A. (2006). *Turbulence An Introduction For Scientists and Engineers*. New York: Oxford University Press.

Dungey, J. W. (1961). Interplanetary Magnetic Field and the Auroral Zones. *Phys. Rev. Lett. 6*, 47–48.

Dyson, P. L., J. P. McClure, and W. B. Hanson (1974). In Situ Measurements of the Spectral Characteristics of F Region Ionospheric Irregularities. *Journal of Geophysical Research 79*(10), 1497–1502.

Earle, G. D. and M. C. Kelley (1993). Spectral Evidence for Stirring Scales and 2-Dimensional Turbulence in the Auroral Ionosphere. *Journal of Geophysical Research-Space Physics 98*(A7), 11543–11548.

Emery, W. J. and R. E. Thomson (2004). *Data Analysis Methods in Physical Oceanography Second and Revised Edition*. Amsterdam: Elvesier.

Farge, M. (1992). Wavelet Transforms and their Applications to Turbulences. *Annual Review of Fluid Mechanics 24*, 395–457.

Foster, J. C., A. J. Coster, P. J. Erickson, J. M. Holt, F. D. Lind, W. Rideout, M. McCready, A. van Eyken, R. J. Barnes, R. A. Greenwald, and F. J. Rich (2005). Multiradar observations of the polar tongue of ionization. *Journal of Geophysical Research-Space Physics 110*(A9), A09S31.

Fredricks, R. W. and F. V. Coroniti (1976). Ambiguities in the Deduction of Rest Frame Fluctuation Spectrums From Spectrums Computed in Moving Frames. *Journal of Geophysical Research-Space Physics 81*(31), 5591–5595.

Frisch, U. (1995). *Turbulence The Legacy of A.N. Kolmogorov*. New York: Cambridge University Press.

Glover, D. M., W. J. Jenkins, and S. C. Doney (2011). *Modeling Methods for Marine Science*. New York: Cambridge University Press.

Gondarenko, N. A. and P. N. Guzdar (2004). Plasma patch structuring by the nonlinear evolution of the gradient drift instability in the high-latitude ionosphere. *Journal of Geophysical Research: Space Physics 109*(A9), A09301.

Gondarenko, N. A. and P. N. Guzdar (2006). Nonlinear three-dimensional simulations of mesoscale structuring by multiple drives in high-latitude plasma patches. *Journal of Geophysical Research: Space Physics 111*(A8), A08302.

Greenwald, R. A., K. B. Baker, J. R. Dudeney, M. Pinnock, T. B. Jones, E. Thomas, J.-P. Villain, J.-C. Cerisier, C. Senior, C. Hanuise, R. D. Hunsucker, G. Sofko, J. Koehler, E. Nielsen, R. Pellinen, A. D. M. Walker, N. Sato, and H. Yamagishi (1995). Darn/superdarn a global view of the dynamics of high-latitude convection. *Space Science Reviews 71*(1-4), 761–796.

Haerendel, G. and G. Paschmann (1975). Entry of Solar Wind Plasma into the Magnetosphere. In Hultqvist, B. and Stenflo, L. (Ed.), *Physics of the Hot Plasma in the Magnetosphere*. New York: Springer.

Hapgood, M. A. (1992). Space Physics Coordinate Transformations - A User Guide. *Planetary and Space Science 40*(5), 711–717.

Horbury, T. S., R. T. Wicks, and C. H. K. Chen (2011). Anisotropy in Space Plasma Turbulence: Solar Wind Observations. *Space Science Reviews, Online First*, 325–342.

Huba, J. and S. Ossakow (1979). On the generation of 3-m irregularities during equatorial spread f by low-frequency drift waves. *Journal of Geophysical Research: Space Physics 84*(A11), 6697–6700.

Hudgins, L., C. A. Friehe, and M. E. Mayer (1993). Wavelet transforms and atmopsheric turbulence. *Phys. Rev. Lett. 71*, 3279–3282.

Hughes, W. J. (1995). The Magnetopause, the Magnetotail, and Magnetic Reconnection. In Margaret G. Kivelson and Christopher T. Russel (Ed.), *Introduction to Space Physics*. New York: Cambridge University Press.

Hundausen, A. J. (1995). The Solar Wind. In Margaret G. Kivelson and Christopher T. Russel (Ed.), *Introduction to Space Physics*. New York: Cambridge University Press.

Hysell, D. L. and M. C. Kelley (1997). Decaying equatorial f-region plasma depletions. *Journal of Geophysical Research: Space Physics 102*(A9), 20007–20017.

Hysell, D. L., M. C. Kelley, W. E. Swartz, R. F. Pfaff, and C. M. Swenson (1994). Steepened Structures in Equatorial Spread-F: 1. New Observations. *Journal of Geophysical Research-Space Physics 99*(A5), 8827–8840.

Hysell, D. L., C. E. Seyler, and M. C. Kelley (1994). Steepened structures in equatorial spread-f: 2. theory. *Journal of Geophysical Research: Space Physics 99*(A5), 8841–8850.

Jacobsen, K. S., A. Pedersen, J. I. Moen, and T. A. Bekkeng (2010). A New Langmuir Probe Concept for Rapid Sampling of Space Plasma Electron density. *Measurement Science & Technology 21*(8), 085902.

Jahn, J. M. and J. LaBelle (1998a). Rocket Measurements of High-Altitude Spread F Irregularities at the Magnetic Dip Equator. *Journal of Geophysical Research-Space Physics 103*(A10), 23427–23441.

Jahn, J. M. and J. LaBelle (1998b). Rocket Measurements of High-Altitude Spread F Irregularities at the Magnetic Dip Equator. *Journal of Geophysical Research-Space Physics 103*(A10), 23427–23441.

Jenkins, G. M. and D. G. Watts (1968). *Spectral Analysis and its Applications*. San Fransisco: Holden-Day.

Kelley, M. C. (2009). *The Earth's Ionosphere Plasma Physics and Electrodynamics Second Edition*. Amsterdam: Elsevier.

Kelley, M. C., K. D. Baker, J. C. Ulwick, C. L. Rino, and M. J. Baron (1980). Simultaneous Rocket Probe, Scintillation, and Incoherent Scatter Radar Observations of Irregularities in the Auroral zone Ionosphere. *Radio Science 15*(3), 491–505.

Kelley, M. C., T. L. Franz, and G. Prasad (2002). On the turbulent spectrum of equatorial spread f: A comparison between laboratory and space results. *Journal of Geophysical Research: Space Physics 107*(A12), 1432.

Kelley, M. C. and P. M. Kintner (1978). Evidence for two-dimensional inertial turbulence in a cosmic-scale low-beta plasma. *Astrophysical Journal 220*, 339–343.

Kelley, M. C., R. Pfaff, K. D. Baker, J. C. Ulwick, R. Livingston, C. Rino, and R. Tsunoda (1982). Simultaneous Rocket Probe and Radar Measurements of Equatorial Spread-F - Transitional and Short Wavelength Results. *Journal of Geophysical Research-Space Physics*, 1575–1588.

Kelley, M. C., J. F. Vickrey, C. W. Carlson, and R. Torbert (1982). On the Origin and Spatial Extent of High-Latitude F-Region Irregularities. *Journal of Geophysical Research-Space Physics 87*(NA6), 4469–4475.

Keskinen, M. J., H. G. Mitchell, J. A. Fedder, P. Satyanarayana, S. T. Zalesak, and J. D. Huba (1988). Nonlinear evolution of the kelvin-helmholtz instability in the high-latitude ionosphere. *Journal of Geophysical Research: Space Physics 93*(A1), 137–152.

Keskinen, M. J. and S. L. Ossakow (1983). Theories of High-Latitude Ionospheric Irregularities - A Review. *Radio Science 18*(6), 1077–1091.

Kintner, P. and N. D Angelo (1977). A transverse kelvin-helmholtz instability in a magnetized plasma. *Journal of Geophysical Research 82*(10), 1628–1630.

Kintner, P. M., M. C. Kelley, and F. S. Mozer (1978). Electrostatic hydrogen cyclotron waves near one earth radius altitude in the polar magnetosphere. *Geophysical Research Letters 5*(2), 139–142.

Kintner, P. M. and C. E. Seyler (1985). The Status of Observations and Theory of High-Latitude Ionospheric and Magnetospheric Plasma Turbulence. *Space Science Reviews 41*(1-2), 91–129.

Kivanc, O. and R. A. Heelis (1997). Structures in ionospheric number density and velocity associated with polar cap ionization patches. *Journal of Geophysical Research-Space Physics 102*(A1), 307–318.

Kivelson, M. G. (1995). Physics of Space Plasmas. In Margaret G. Kivelson and Christopher T. Russel (Ed.), *Introduction to Space Physics*. New York: Cambridge University Press.

Knudsen, W. C. (1974). Magnetospheric Convection and High Latitude F2 Ionosphere. *Journal of Geophysical Research 79*(7), 1046–1055.

Kraichnan, R. H. (1967). Inertial ranges in two-dimensional turbulence. *Physics of Fluids 10*(7), 1417–1423.

Kraichnan, R. H. and D. Montgomery (1980). Two-dimensional turbulence. *Reports on Progress in Physics 43*(5), 547.

Kumar, P. and E. Foufoula-Georgiou (1997). Wavelet analysis for geophysical applications. *Reviews of Geophysics 35*(4), 385–412.

LaBelle, J. and M. C. Kelley (1986). The Generation of Kilometer Scale Irregularities in Equatorial Spread-F. *Journal of Geophysical Research-Space Physics 91*(A5), 5504–5512.

LaBelle, J., M. C. Kelley, and C. E. Seyler (1986). An Analysis of the Role of Drift Waves in Equatorial Spread-F. *Journal of Geophysical Research-Space Physics 91*(A5), 5513–5525.

LaBelle, J. and E. J. Lund (1992). Bispectral analysis of equatorial spread f density irregularities. *Journal of Geophysical Research: Space Physics 97*(A6), 8643–8651.

Lagoutte, D., J. L. Cerisier, J. C.and Plagnaud, J. P. Villain, and B. Forget (1992). High-Latitude Ionospheric Electrostatic Turbulence Studied by Means of The Wavelet Transform. *Journal of Atmospherical and Terrestrial Physics 54*(10), 1283–1293.

Lau, K. M. and H. Weng (1995). Climate Signal Detection Using Wavelet Transform: How to Make a Time Series Sing. *Bulletin of the American Meteorological Society 76*(12), 2391–2402.

Leith, C. E. (1971). Atmospheric Predictability and 2-Dimensional Turbulence. *Journal of the Atmospheric Sciences 28*(2), 145–161.

Lepping, R. P., D. B. Berdichevsky, and C. C. Wu (2003). Sun-Earth Electrodynamics: The Solar Wind Connection. *Recent Res. Devel. Astrophys., Research Signpost, 1*, 139–171.

Lockwood, M. and H. C. Carlson (1992). Production of polar cap electron density patches by transient magnetopause reconnection. *Geophysical Research Letters 19*(17), 1731–1734.

Lockwood, M., W. F. Denig, A. D. Farmer, V. N. Davida, S. W. H. Cowley, and H. Luhr (1993). Ionospheric Signatures of Pulsed Reconnection at the Earth's Magnetopause. *Nature 361*(6411), 424–428.

Lorentzen, D. A., J. Moen, K. Oksavik, F. Sigernes, Y. Saito, and M. G. Johnsen (2010). In Situ Measurement of a Newly Created Polar Cap Patch. *Journal Of Geophysical Research-Space Physics 115*, A12323.

Low, B. C. (2001). Coronal Mass Ejections, Magnetic Flux Ropes, and Solar Magnetism. *Journal of Geophysical Research-Space Physics 106*(A11), 25141–25163.

Lyons, R. G. (2004). *Understanding Digital Signal Processing, Second Edition*. Upper Saddle River: Prentice Hall PTR.

Merrill, L. T. (2010). *Our Magnetic Earth: The Science of Geomagnetism*. Chicago: The University of Chicago Press.

Moen, J., H. C. Carlson, S. E. Milan, N. Shumilov, B. Lybekk, P. E. Sandholt, and M. Lester (2000). On the collocation between dayside auroral activity and coherent hf radar backscatter. *Annales Geophysicae 18*(12), 1531–1549.

Moen, J., H. C. Carlson, K. Oksavik, C. P. Nielsen, S. E. Pryse, H. R. Middleton, I. W. McCrea, and P. Gallop (2006). Eiscat observations of plasma patches at sub-auroral cusp latitudes. *Annales Geophysicae 24*(9), 2363–2374.

Moen, J., H. C. Carlson, Y. Rinne, and A. Skjaeveland (2012). Multi-Scale Features of Solar Terrestrial Coupling in the Cusp Ionosphere. *Journal of Atmospheric and Solar-Terrestrial Physics 87-88*(SI), 11–19.

Moen, J., K. Oksavik, T. Abe, M. Lester, Y. Saito, T. A. Bekkeng, and K. S. Jacobsen (2012). First in-situ measurements of HF radar echoing targets. *Geophysical Research Letters 39*, L07104.

Moen, J., K. Oksavik, L. Alfonsi, Y. Daabakk, V. Romano, and L. Spogli (2013). Space Weather Challenges of the Polar Cap Ionosphere. *Journal of Space Weather and Space Climate 3*(26), A02.

Moen, J., I. K. Walker, L. Kersley, and S. E. Milan (2002). On the Generation of Cusp HF Backscatter Irregularities. *Journal of Geophysical Research-Space Physics 107*(A4), SIA 3–1–SIA 3–5.

Mounir, H., J. C. Cerisier, A. Berthelier, D. Lagoutte, and C. Beghin (1991). The Small-Scale Turbulent Structure of the High-Latitude Ionosphere: ARCAD-AUREOL-3 observations. *Annales Geophysicae-Atmospheres Hydrospheres and Space Sciences 9*(11), 725–737.

Newell, P. T. and C.-I. Meng (1992). Mapping the dayside ionosphere to the magnetosphere according to particle precipitation characteristics. *Geophysical Research Letters 19*(6), 609–612.

Newell, P. T., J. M. Ruohoniemi, and C.-I. Meng (2004). Maps of precipitation by source region, binned by imf, with inertial convection streamlines. *Journal of Geophysical Research: Space Physics 109*(A10), A10206.

Oksavik, K., J. Moen, M. Lester, T. A. Bekkeng, and J. K. Bekkeng (2012). In Situ Measurements of Plasma Irregularity Growth in the Cusp ionosphere. *Journal of Geophysical Research-Space Physics 117*, A11301.

Oksavik, K., J. M. Ruohoniemi, R. A. Greenwald, J. B. H. Baker, J. Moen, H. C. Carlson, T. K. Yeoman, and M. Lester (2006). Observations of isolated polar cap patches by the european incoherent scatter (eiscat) svalbard and super dual auroral radar network (superdarn) finland radars. *Journal of Geophysical Research: Space Physics 111*(A5), A05310.

Ossakow, S. L. and P. K. Chaturvedi (1979). Current Convective Instability in the Diffuse Aurora. *Geophysical Research Letters 6*(4), 332–334.

Ossakow, S. L., P. K. Chaturvedi, and J. B. Workman (1978). High-Altitude Limit of Gradient Drift Instability. *Journal of Geophysical Research-Space Physics 83*(NA6), 2691–2693.

Paschmann, G. (1991). Geomagnetism. In Jacobs, J. A. (Ed.), *The Magnetopause*. New York: Academic Press.

Paschmann, G., G. Haerendel, N. Sckopke, H. Rosenbauer, and P. C. Hedgecock (1976). Plasma and Magnetic Field Characteristics of the Distant Polar Cusp near Local Noon: The Entry Layer. *Journal of Geophysical Research 361*(6411), 2883–2899.

Pécseli, H. L. (2012). *Waves and Oscillations in Plasmas*. Boca Raton: Taylor and Francis.

Pfaff Jr., R. F. (2012). The Near-Earth Plasma Environment. *Space Science Reviews 168*(1-4), 23–112.

Phelps, A. D. R. and R. C. Sagalyn (1976). Plasma-Density Irregularities in High Latitude Top Side Ionosphere. *Journal of Geophysical Research-Space Physics 81*(4), 515–523.

Priest, E. R. (1995). The Sun and its Magnetohydrodynamics. In Margaret G. Kivelson and Christopher T. Russel (Ed.), *Introduction to Space Physics*. New York: Cambridge University Press.

Priestley, M. B. (1981). *Spectral Analysis and Time Series volume 1 Univariate Series*. Orlando: Academic Press.

Proelss, G. (2004). *Physics of the Earth's Space Environment: an Introduction*. Berlin Heidelberg: Springer.

Rinne, Y. (2006). *EISCAT Observations of Reversed Flow Events in the Cusp Ionosphere*. Department of Physics, The University of Oslo, Oslo.

Rodger, A. S., M. Pinnock, J. R. Dudeney, K. B. Baker, and R. A. Greenwald (1994). A New Mechanism for Polar Patch Formation. *Journal of Geophysical Research-Space Physics 99*(A4), 6425–6436.

Rodrigues, F. S., M. C. Kelley, P. A. Roddy, D. E. Hunton, R. F. Pfaff, O. de La Beaujardiere, and G. S. Bust (2009). C/NOFS Observations of Intermediate and Transitional Scale-Size Equatorial Spread F Irregularities. *Geophysical Research Letters 36*, L00C05.

Russell, C. T. (2000). *The polar cusp*, Volume 25 of *Advances in Space Physics*, pp. 1413–1424.

Sandholt, P. E., H. C. Carlson, and A. Egeland (2002). *Dayside and Polar Cap Aurora*. Dordrecht: Kluwer Academic Publishers.

Sandholt, P. E. and C. J. Farrugia (2007). Poleward Moving Auroral Forms (PMAFs) Revisited: Responses of Aurorae, Plasma Convection and Birkeland Currents in the Pre- and Postnoon Sectors under Positive and Negative IMF B(y) Conditions. *Annales Geophysicae 25*(7), 1629–1652.

Sandholt, P. E., C. J. Farrugia, and W. F. Denig (2004). Dayside Aurora and the Role of IMF Vertical $|B_y|/|B_z|$: Detailed Morphology and Response to Magnetopause Reconnection. *Annales Geophysicae 22*(2), 613–628.

Sandholt, P. E., C. J. Farrugia, J. Moen, O. Noraberg, B. Lybekk, T. Sten, and T. Hansen (1998). A classification of dayside auroral forms and activities as a function of interplanetary magnetic field orientation. *Journal of Geophysical Research-Space Physics 103*(A10), 23325–23345.

Schultz-Dubois, E. O. and I. Rehberg (1981). Structure-Function in Lieu of Correlation-Function. *Applied Physics 24*(4), 323–329.

Schunk, R. W. and A. F. Nagy (2009). Ionospheres Physics, Plasma Physics, and Chemistry Second Edition. Cambridge: Cambridge University Press .

Shkarofsky, I. P. (1969). Turbulence of Fluids and Plasmas. In Jerome Fox (Ed.), *Analytic Forms for Decaying Space/Time Turbulence Functions*. New York: Polytechnic Press of the Polytechnic Institute of Brooklyn.

Similon, P. L. and R. N. Sudan (1990). Plasma Turbulence. *Annual Review of Fluid Mechanics 22*, 317–347.

Singh, M., P. Rodriguez, and E. P. Szuszczewicz (1985). Spectral Classification of Medium-Scale High-Latitude F-Region Plasma-Density Irregularities. *Journal of Geophysical Research-Space Physics 90*(NA7), 6525–6532.

Siscoe, G. L., W. Lotko, and B. U. O. Sonnerup (1991). A High-Latitude, Low-Latitude Boundary-Layer Model of The Convection Current System. *Journal of Geophysics Research-Space Physics 96*(A3), 3487–3495.

Smith, M. F. (1994). Transient Dayside Reconnection and its Effects on the Ionosphere. In Holtet, J. A. and Egeland, A. (Ed.), *Physical Signatures of Magnetospheric Boundary Layer Processes*, Volume 425, pp. 275–289. Nato Advanced Science Institues Series, Series C, Mathematical and Physical Sciences.

Sojka, J. J., M. V. Subramanium, L. Zhu, and R. W. Schunk (1998). Gradient Drift Instability Growth Rates from Global-Scale Modeling of the Polar Ionosphere. *Radio Science 33*(6), 1915–1928.

Sonar, T. (2011). Turbulences sur Les Equations des Fluides. *Pour la Science 115*, A12323.

Sonnerup, B. U. O. (1985). Solar Wind Interaction with Planetary Magnetic Fields. *ESA Future Missions in Solar, Heliospheric and Plasma*, 53–64.

Stix, M. (2004). *The Sun: An Introduction Second Edition*. Heidelberg: Springer.

Sudan, R. N. and M. J. Keskinen (1984). Unified theory of the power spectrum of intermediate wavelength ionospheric electron density fluctuations. *Journal of Geophysical Research-Space Physics 89*(A11), 9840–9844.

Taylor, G. I. (1938). The Spectrum of Turbulence. *Proceedings of The Royal Society of London Series a Mathematical and Physical Sciences 164*(A919), 0476–0490.

Torrence, C. and G. P. Compo (1998). A practical guide to wavelet analysis. *Bulletin of the American Meteorological Society 79*(1), 61–78.

Treumann, R. A. and W. Baumjohann (1997). *Advanced Space Plasma Physics*. London: Imperial College Press.

Tsinober, A. (2009). *An Informal Conceptual Introduction to Turbulence*. Berlin: Springer.

Tsunoda, R. T. (1988). High-Latitude F-Region Irregularities - A Review and Synthesis. *Reviews of Geophysics 26*(4), 719–760.

Vickrey, J. F. and M. C. Kelley (1982). The Effects of a Conducting E-Layer on Classical F-Region Cross-Field Plasma-Diffusion. *Journal of Geophysical Research-Space Physics 87*(NA6), 4461–4468.

Villain, J. P., C. Beghin, and C. Hanuise (1986). ARCAD3-SAFARI Coordinated Study of Auroral and Polar F-Region Ionospherric Irregularities. *Annales Geophysicae Series A-Upper Atmosphere and Scpace Sciences 4*(1), 61–68.

Walker, D. N., P. K. Chaturvedi, M. Singh, P. Rodriguez, C. Siefring, and N. M. Baumback (1991). Low-Frequency Oscillations Associated with a Polar-Cap Auroral Arc : Local Spectral Density Estimation . *Journal of Geophysical Research-Space Physics 96*(A3), 3589–3600.

Weber, E. J., J. Buchau, J. G. Moore, J. R. Sharber, R. C. Livingston, J. D. Winningham, and B. W. Reinisch (1984). F layer ionization patches in the polar cap. *Journal of Geophysical Research: Space Physics 89*(A3), 1683–1694.

Wei, W. W. S. (2006). *Time series analysis: univariate and multivariate methods*. Boston: Pearson Addison Wesley.

Weimer, D. R. (1995). Models of high-latitude electric potentials derived with a least error fit of spherical harmonic coefficients. *Journal of Geophysical Research: Space Physics 100*(A10), 19595–19607.

Xing, Z. Y., H. G. Yang, D. S. Han, Z. S. Wu, J. M. Liu, Z. J. Hu, Q. H. Zhang, H. Q. Hu, and Y. H. Liu (2013). Dayside poleward moving auroral forms and ionospheric convection under stable interplanetary magnetic field (IMF) conditions. *Science China-Technological Sciences 56*(4), 910–916.

Yordanova, E. (2005). *Scaling behaviour of Turbulence in the Polar cusp, thesis submitted for the degree of Doctor of Physics.* Space Research Centre, Polish Academy of Science, Warsaw.